THE UNIVERSITY *of* EDINBURGH

Evaluating Spectral Radiances Simulated by the HadGEM2 Global Climate Model using Longwave Satellite Measurements

Emma Catherine Turner

A thesis presented for the degree of
Doctor of Philosophy

The University of Edinburgh

2015

Declaration

This thesis and the work presented herein is my own original composition. Where it draws on the work of others this is acknowledged at the appropriate points in the text. Chapter 2 comprises work that has been accepted for publication in a peer-reviewed scientific journal where I am the lead author. Chapter 3 comprises work that has been accepted as a discussion paper for a peer reviewed scientific journal where I am also the lead author. I confirm that appropriate credit has been given within the thesis where reference has been made to the work of others. No part of this work has been submitted for any other degree or professional qualification.

Chapter 2 is based on the following paper published in *Climate Dynamics*:
'Emma C Turner and Simon FB Tett. Using longwave HIRS radiances to test climate models. Pages 1-25, 2013'

Chapter 3 is based on the following paper which is under revised review in *Atmospheric Chemistry and Physics Discussions*:
'Emma C Turner, Hai-Tien Lee and Simon FB Tett. Using IASI to simulate the total spectrum of Outgoing Longwave Radiances 14(12):18421-18459, 2014'

Emma Turner
January 13, 2015

Abstract

A 'model-to-radiance' comparison of simulated brightness temperatures and radiances from the Hadley Centre Global Environmental Model 2 (HadGEM2-A) with longwave measurements from the High Resolution Infrared Radiation Sounder/4 (HIRS/4) and the Infrared Atmospheric Sounding Interfermeter (IASI) onboard the MetOp-A satellite is presented for all-sky and clear-sky global means. The fast Radiative Transfer model for TOVS 10 (RTTOV-10) is applied to HadGEM2 output to simulate observational-equivalent data. The results are compared with corresponding broadband analyses. A method is developed to extend hyperspectral IASI radiances to cover the whole outgoing terrestrial spectrum, in order to identify any compensating biases, and explore wavebands in the unobserved Far Infrared (FIR) region.

For the all-sky HIRS analysis, the model overestimates brightness temperatures in the atmospheric window region with the greatest biases over areas associated with deep convective cloud. In contrast to many global climate models, much smaller clear-sky biases are found indicating that model clouds are the dominating source of error. Simulated values in upper atmospheric CO_2 channels approximate observations better as a result of compensating cold biases at the poles and warm biases at lower latitudes, due to a poor representation of the Brewer Dobson circulation in the 38 level 'low-top' configuration of the model. Simulated all and clear-sky outgoing longwave radiation evaluated against the Clouds and the Earth's Radiant Energy System (CERES) and HIRS OLR products reveal good agreement, in part due to cancellation of positive and negative biases. Through physical arguments relating to the spectral energy balance within a cloud, it is suggested that broadband agreement could be the result of a balance between positive window biases and unseen

negative biases originating from the water vapour rotational band in the FIR (not sampled by HIRS). Simple sensitivity tests show that dramatically altering existing cloud properties has little effect on the prominent window biases, however raising clouds a maximum of 5 atmospheric levels minimises the error in cloud contaminated channels, due to the introduction of spatially compensating errors. Sensitivities to the way ice clouds are parameterised in RTTOV-10 display a range of up to 2.5 K in window channels but absolute biases still exceed 3 K for all choices.

Because of the lack of satellite based FIR observations due to a technological gap in the spectral region, an algorithm is created to 'fill in' the available data. Correlations between selected IASI channels and simulated unobserved wavelengths in the far infrared are used to estimate radiances between 25.25 - 644.75 cm^{-1} at 0.5 cm^{-1} intervals. The same method is used in the 2760 - 3000 cm^{-1} region. The spectrum is validated by comparing the Integrated Nadir Longwave Radiance (INLR) product (spanning the whole 25.25 - 3000 cm^{-1} range) with the corresponding broadband measurements from the Clouds and the Earth's Radiant Energy System (CERES) instrument on the Terra and Aqua satellites at simultaneous nadir overpasses, revealing mean differences of 0.3 $Wm^{-2}sr^{-1}$ (0.5% relative difference) lower for IASI relative to CERES and significantly lower biases in nighttime only scenes. Averaged global data over a single month produces mean differences of about 1 $Wm^{-2}sr^{-1}$ in both the all and the clear-sky (1.2% relative difference). The new high resolution spectrum is presented for global mean clear and total skies where the far infrared is shown to contribute 44% and 47% to the total OLR respectively, which is consistent with previous estimates. In terms of spectral cloud radiative forcing, the FIR contributes 19% and in some subtropical instances appears to be negative, results that would go un-observed with a traditional broadband analysis.

The equivalent complete IASI OLR model product is simulated from GCM data using RTTOV-10. The same process of applying predictors to the satellite measurements is applied to the model simulated radiances, with appropriate modifications, to produce a directly comparable model product. Annual mean all-sky radiances are still greatly overestimated at all wavenumbers with a total radiance bias of 4.52 Wm^{-2} across the whole range. Compensating negative biases outside of the HIRS coverage that were hypothesised are absent, with the far infrared contributing to the overall bias rather

than cancelling it. Equivalent clear-sky biases are much lower overall at 0.39 Wm^{-2}, in part due to spectral and spatial cancellation of errors. A flux-to-flux comparison is enabled by estimating the spatial distribution of anisotropic factors, using collated HIRS OLR fluxes and IASI OLR radiances, which yields global mean model fluxes in excess of 12 Wm^{-2} higher than observations in the all-sky. The difference between this and the fluxes calculated using the climate model's broadband radiation code (Edward-Slingo) are around 10 Wm^{-2} which is outside the range of uncertainty in the method used to estimate the flux. However, it is discussed that tuning of the climate model's broadband code to known flux values is a required practice to ensure global energy budgets balance but can produce inaccurate parameterised variables. An equivalent analysis adjusting the ice cloud parametrisation to reflect the radiances that have the biggest differences to the original configuration selected showed a bias reduction of 4.5 Wm^{-2}, which is still not enough to completely explain its size, suggesting the existence of residual cloud problems. Finally, it is suggested that the way forward in separating and constraining cloud errors, in both radiative transfer codes, is a rigorous process of testing them with observation cloud properties and reanalysis data as inputs.

Acknowledgements

I would like to thank all the people who helped and supported me with writing this thesis. First and foremost to my supervisor, Professor Simon Tett, for his unwavering persistence, who always made time for me and gave me a great deal of freedom with the direction of the project, which ended far from where it started. I would particularly like to acknowledge Simon's big cheery personality which was invaluable in making every situation seem brighter. I also owe a debt of gratitude to Dr Hai-Tien Lee for coming up with the idea of using the IASI satellite instrument to construct the missing parts of the longwave spectrum, which formed the basis of the latter half of this thesis, and thank him for his collaboration and invariably quick and helpful responses to any queries I had.

Thankyou also to Professor Chris Merchant for his useful advice and for offering a different perspective in the early stages of the project, and to my advisor Dr Hugh Pumphrey who oversaw the progress of my PhD and gave detailed explanations of difficult concepts. Many thanks to my external examiner Professor Richard Allen for taking the time to read my thesis and make helpful suggestions, and to my internal examiner Dr Richard Essery for his highly efficient overseeing of the examination.

Being a strongly computational project none of this work could have been done without the technical facilities and support provided at the University of Edinburgh, and I would like to particularly thank the kindness of Dr Mike Mineter, for the many hours he spent sitting with me staring at a screen full of terminals - we always got there in the end! I was also very appreciative in the early stages for help from two postdocs, Dr Ian MacKenzie, and Dr Anders Lindfors for sharing their codes and giving understandable explanations of complex theories. I would also like to thank

some Met Office employees, Dr James Hocking and Dr Roger Saunders, who were always onhand to answer my many questions about the RTTOV radiative transfer code, Dr Viju John, who provided processed HIRS satellite data files, and Dr Cyril Morcrette, for his considerable efforts in explaining how clouds work in the HadGEM2 climate model.

My time as a postgraduate student was greatly enriched by the discussions and time spent with my climate research group, Carley Iles, Darren Slevin, Andrew Schurer, Tom Russon, Debbie Poulson, Oli Browne and Andrew Harding, and my flat mates through the years, Robin Driscoll, Richard Nair and Dean Thorpe. Additionally I am lucky enough to have too many friends and colleagues to mention, but I want to especially thank Gillian McKay for always providing a warm shoulder, and Robin Driscoll for wine and gin related support. Thankyou to everyone in the Grant Institute and beyond, particularly Rachel Kilgallon, Robyn Tuerena, Lizzie Entwistle, Emma Knowland, Matt Walker, Paddy O'Connor and Rory McKavney for making my final few months of thesis writing more enjoyable than they probably should have been.

Finally thankyou to my father, Randle Turner, who gave me more unconditional support than I could ever have asked for, and to my mother, Janet Light, the first mathematics graduate in our family, who no doubt influenced me in my choice of a numerical career and without whose encouragement I would not be the person who wrote this thesis.

List of Figures

List of Tables

Contents

Chapter 1

Introduction

Systematic testing of climate models via observational comparisons is a prerequisite to applying them confidently. By it's very nature, a model is a simplification of the real world, but if the output is to be used as the basis for decision-making, it is a vital requirement that its performance is shown to be adequate enough for this purpose. The 5th Intergovernmental Panel on Climate Change Report: The Physical Science Basis (Stocker et al., 2013), dedicates an entire chapter to the evaluation of climate models, in which it states that a major development since the previous report is the increased range of climate variables and processes being evaluated. Differences between models and observations are increasingly being quantified using so-called 'performance metrics' (Gleckler et al., 2008). Two such standard metrics are shortwave and longwave radiative fluxes measured at the top of atmosphere (TOA), which are evaluated by broadband satellite observations. There is no specification in the report for a similar analysis to be performed at a spectral level, the details of which contain a potentially rich source of information. This is in part due to previous technological limitations, both on the instrumental and model side. However, recent developments in both fields have offered the chance to gain unprecedented insights into the decomposed spectrum.

This chapter covers the motivation for testing climate models with narrowband and hyperspectral satellite measurements, with a particular emphasis placed on the all-sky (cloud inclusive) analysis, greatly increasing the complexity of the problem due to the challenges involved. The theory behind the treatment of radiation by climate

models and fast radiative transfer schemes is outlined, and the literature surrounding the evaluation of such with satellite measurements is reviewed. This project is restricted to a particular climate model (the Hadley Centre Global Environmental Model version 2 (HadGEM2) developed at the UK Met Office), a particular measure of performance (mean difference or 'bias'), and a particular electromagnetic domain (the terrestrial longwave region), to demonstrate the potential of such an approach.

1.1 Terrestrial long wave radiation

1.1.1 Definition and units

The infrared spectrum is taken to include wavelengths from 0.7 to 1000 μm, and lies between the shorter wavelengths of visible light and the longer wavelengths of microwaves. Longwave is a term that is used primarily to refer to the longer wavelengths of the infrared spectrum that are emitted from the Earth. The definition of the longwave boundaries are variable in the literature, depending on whether the academic base of the author is astronomy, telecommunications or geosciences, but commonly the shortest wavelength considered is either 3 or 5 μm, and the longest is between 200 and 1000 μm. For this thesis the range is defined on the limits from 3.3 to 400 μm, which is set by the range specified by the method used to construct the full spectrum in Chapter 3. The intensity of the radiation emitted at these boundaries typically reduces to less than 0.001% of the total emitted over the whole spectrum.

It is conventional within the field of satellite technology to use the colloquial definition of 'wavenumber' to describe the energy of the radiation, which is a measure of frequency and has units of cm^{-1}. The relationship between wavenumber (ν) and wavelength (λ), measured in μm (10^{-6} m) is:

$$\nu = \frac{10000}{\lambda} \tag{1.1}$$

Hence the coverage of 3.3 to 400 μm is from 25 to 3000 cm^{-1} in wavenumbers. Both wavelength and wavenumber are used in this thesis as appropriate.

1.1.2 Black-body Radiation

The terrestrial longwave radiation spectrum measured from the vantage point of a satellite orbiting the Earth differs from that emitted at the surface, and this is due to atmospheric effects. If the radiation were travelling in a vacuum the spectrum measured would be described by the laws of 'black-body' radiation, the properties of which depend only on the temperature of the emitting surface and the wavelength. A black-body itself is defined as a perfect absorber, so-called because something that absorbs all visible light appears black to the human eye. However, it does also apply to other wavelengths that are not in the visible range, such as those in the infrared. A black-body does not reflect any portion of incident radiation, but re-emits all radiation that it absorbs.

Planck's Law describes the radiance $B_\nu(T)$ emitted by a black-body at wavenumber ν and temperature T of the emitting surface, assuming thermodynamic equilibrium. It is given by:

$$B_\nu(T) = \frac{c_1 \nu^3}{e^{c_2 \nu / T} - 1} \tag{1.2}$$

where the constants c_1 and c_2 are defined in wavenumber form as:

$$c_1 = 2hc^2 \times 10^8 \tag{1.3}$$

$$c_2 = \frac{100hc}{k_b} \tag{1.4}$$

where h is the Planck constant, c is the speed of light and k_b is the Boltzmann constant. The notion of a black-body is a useful standard to have, against which real bodies can be compared. The crux of the notion is the assumption that the emissivity (ϵ_ν) - the proportion of the absorbed radiation that is re-emitted - is equal to 1. In reality all bodies are 'grey bodies', where instead of absorbing 100% of the radiation incident upon them, a portion is reflected. Hence, equation 1.2 has to be scaled by a factor which is less than 1 and the real intensity ($I_\nu(T)$) observed is:

$$I_\nu(T) = \epsilon_\nu B_\nu(T) \tag{1.5}$$

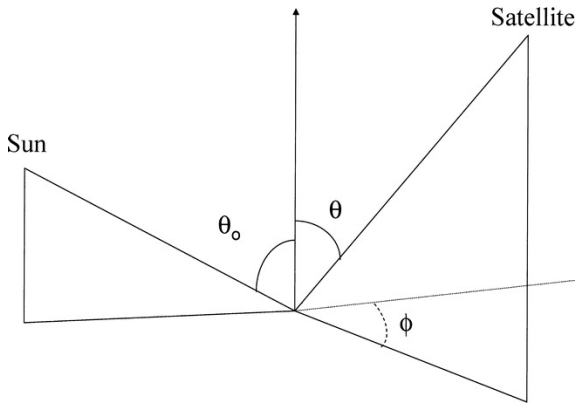

Figure 1.1: Schematic of the Sun-Earth satellite viewing geometry from a point viewed on the Earth. θ_0 is the solar zenith angle, θ is the viewing zenith angle and ϕ is the viewing azimuth angle. From Loeb et al. (2003).

1.1.2.1 Flux

Radiance is a directional quantity measured in $\mathrm{Wm^{-2}sr^{-1}}$ where the steradian (sr) denotes the dependency on solid angle. Most atmospheric radiation studies deal with fluxes measured in $\mathrm{Wm^{-2}}$, which is obtained by integrating the radiance over all solid angles which is necessary for calculations of the Earth's total energy budget. For a single or group of wavenumbers (ν), flux (F_ν) is related to radiance (I_ν) by:

$$F_\nu(\theta_0) = \int_0^{2\pi} \int_0^{\pi/2} I_\nu(\theta_0, \theta, \phi) cos\theta sin\theta d\theta d\phi \tag{1.6}$$

where θ_0 is the solar zenith angle, θ is the viewing zenith angle and ϕ is the viewing azimuth angle of the observer, illustrated in Figure 1.1. For an isotropic field, which is where the radiation is uniformly propagating in all directions, equation 1.6 reduces to:

$$F_\nu = \pi I_\nu \tag{1.7}$$

The degree of deviation from an isotropic field is its 'anisotropy', and is discussed in greater detail in Chapter 4, Section 4.2.5.

1.1.3 Interaction of Longwave Radiation with Matter

Longwave radiation interacts with matter by way of absorption, scattering or emission. The first two of these are extinction mechanisms. For longwave radiation extinction is dominated by absorption processes across the spectrum, however, scattering effects are non-negligible with certain constituents such as clouds. These mechanisms are outlined below.

If the energy of the photons that make up the radiation considered correspond to the difference between two quantum mechanical states of a molecule in its path, all of the energy will be transferred to the molecule. This can induce molecular excitation in the form of electronic transitions, vibrations (stretching or bending), rotation, or a combination of these, depending on its energy which is directly proportional to its wavelength. Longwave radiation does not have enough energy to induce the promotion of electrons to higher energy levels within molecules so there are no electronic transitions in this frequency domain. Vibrations occur when the molecular bond between atoms resonates with a particular 'mode' due to this increase in energy. The 3 modes of vibration for a water vapour molecule are illustrated in Figure 1.2. These are: symmetric stretching (ν_1), bending ν_2, and asymmetric stretching (ν_3). More complicated molecules can vibrate in further rocking and twisting modes. The molecular excitation which requires the least energy is pure rotation, where the molecule must have a permanent or magnetic dipole moments. Additionally combinations of mechanisms can operate at the same time, for example transitions involving changes in both vibrational and rotational states which create rovibrational spectra.

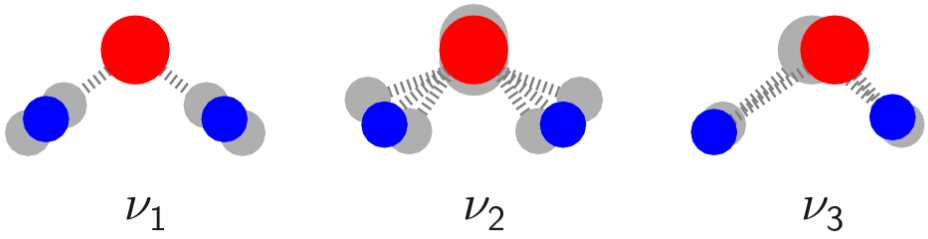

Figure 1.2: The 3 fundamental vibrational modes of molecular absorption for water vapour. ν_1 = symmetric stretching ν_2 = bending ν_3 = asymmetric stretching.

Another important mechanism in the longwave spectrum is known as 'continuum absorption' which is a water vapour effect. This is characterised by a slowly varying absorption with respect to wavelength, as opposed to the relatively narrow spectral lines produced by the rotation and vibrational bands. Around wavelengths with strong sensitivity to certain molecules the continuum is often obscured completely, however where there are atmospheric 'windows' - regions with little or no attenuation by atmospheric gases - it is the dominant absorption mechanism. The causes of continuum absorption are still not well understood, see Shine et al. (2012) for details.

Once the molecule has been exited to a higher vibrational or rotational state, it can release this energy kinetically, via collision with another molecule permanently removing it from the radiation field (pure absorption), or by scattering. Scattering occurs when the excited molecule almost immediately releases a photon identical to the one absorbed, but in a different direction to the original beam of radiation. It is not an important mechanism for gaseous atmospheric constituents such as water vapour because the particles are much smaller than longwave wavelengths. However, for larger particles such as cloud droplets, scattering is far more significant. Scattering by liquid water clouds can be described well by Mie theory (Stephens, 1979), because they can be approximated by spheres. Spheres absorb efficiently and have low anisotropy. Ice particles have irregular shapes that are strongly heterogeneous. Their scattering effects are significantly more complex and difficult to describe by a single theory (Costa and Shine, 2006). Aerosols whose particle radii are of the order of submicron sizes, such as sulfate aerosols, do not interact strongly with radiation in the longwave domain because they are too small. However, mineral dust aerosols have larger radii that have been shown to reduce the outgoing longwave radiation significantly in clear-sky regions where advected dust is prevalent, such as over the dry Saharan desert (Haywood et al., 2005), with both scattering and absorption being equally important by virtue of the non-spherical shape of dust particles (Dufresne et al., 2002).

Emission occurs when molecules are activated by collisions with one other and convert this thermal energy into photons. The energy of these photons corresponds to the result of the Planck equation (1.2), where the wavenumber depends on the emitting molecule and the temperature on the local atmospheric conditions. Absorption,

scattering and emission will occur repeatedly as the photons travel up through the atmosphere until all components become significantly less dense. The remaining one can then continue without exchange of energy to the TOA. The radiance measured here will therefore reflect the temperature at the level of the uppermost medium interacted with, which is highly wavelength specific. This is the basis of temperature sounding by satellite instruments.

1.1.4 The Longwave Spectrum

Figure 1.3 shows blackbody curves at various temperatures overlying an observed atmospheric spectrum measured by a satellite instrument at the TOA. The black-body curve with maximum intensity corresponds to the global annual mean Sea Surface Temperature (SST) of 287.6 K[1]. Where the observed radiance curve differs significantly from the shape of a black-body, extinction is occurring due to one or more atmospheric constituents.

From Figure 1.3 it can be observed that the atmosphere affects all longwave wavenumbers as the intensity of the real spectrum is consistently reduced with respect to the surface intensity. The overlying Planck functions give an indication of the temperature of the level of radiant emission where they intersect with the observed curve. The following describes the general features of the longwave spectrum. Radiation at wavenumbers around 600 - 700 cm^{-1} are subject to CO_2 absorption from the vibrational ν_2 band, placing the average level of emission in the upper troposphere / lower stratosphere at temperatures which are as low as 213 K. Absorption is strongest at the centre of the band producing the 248 K spike at 669 cm^{-1} which arises because the level of emission is highest in the stratosphere, where the temperatures increase with height. The peak of ozone absorption at 1030 cm^{-1} also emits around this level, above the ozone distribution.

All wavenumbers below the approximate cutoff of 645 cm^{-1} belong to a region termed the 'Far Infrared' (FIR) which is sensitive to the rotational transitions of water vapour and places the level of emission in the upper troposphere, because water

[1]Taken from the GISS Surface Temperature Analysis (GISTEMP) available publically at http://www.data.giss.nasa.gov/gistemp/

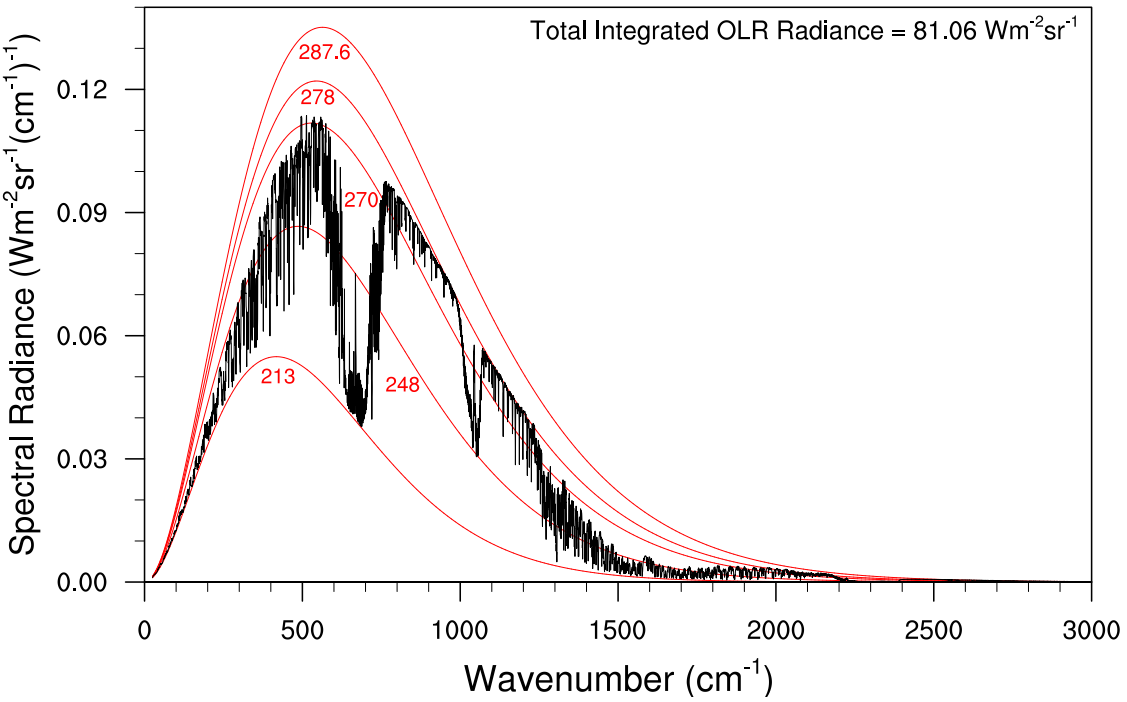

Figure 1.3: Top of atmosphere global mean Outgoing Longwave Radiance (OLR) spectrum which is the global mean of all 2009 data measured by the IASI hyperspectral instrument on the MetOp-A satellite (black curve). The range of wavenumbers measured have been spectrally extended to cover the full extent of the OLR, following the method detailed in Chapter 3. Red lines show the equivalent black-body spectra (Equation 1.2) for the labelled temperatures, measured in Kelvin.

vapour has a higher concentration near the surface. There is increasingly strong absorption towards lower wavenumbers. The wavenumber that emits the highest intensity of longwave photons is around 559 cm^{-1}, which falls into the 'window' region of the FIR where water vapour absorption is lower. This region is discussed in more detail in Chapter 3, Section 3.1. Wavenumbers beyond 1250 cm^{-1} are sensitive to the vibrational mode of water vapour where the bending ν_2 absorption peaks at 1595 cm^{-1}. The mid-infrared window region between 800 and 1250 cm^{-1} emits from the lowest levels in the atmosphere, because it is not sensitive to the excitation energies of any atmospheric gas, apart from the constant noise from the water vapour continuum. It approximately lies on a black-body curve at 278 K which is somewhat below the intensity at the average surface temperature of 287.6 K because of the presence of clouds, which are opaque to the whole longwave spectrum. When a

cloud is present radiation is emitted from the cold cloud top bringing the average radiance down. Airborne mineral dust, when present over clear-sky arid desert areas, can affect wavenumbers in the window region with a peak at 1000 cm^{-1}.

1.1.5 Weighting Functions

The weighting function is a useful concept used in remote sensing to give an indication of the altitude that the majority of the radiation measured at the TOA for a given spectral band ν comes from. It is a dimensionless quantity that effectively gives a 'weight' to the Planck radiation at each layer in the atmosphere, and depends primarily on the emissivity (ϵ_ν) and the transmittance (τ_ν) of the layer, where τ_ν is the fraction of the incident radiation that passes through a medium. The radiance received at the TOA (I_ν) from all atmospheric layers (l) can be written as:

$$I_\nu = B_{v,s}(T_s)\tau_{\nu,s}\epsilon_s + \sum^{l} B_{v,l}(T_l)\tau_{\nu,l}\epsilon_l \tag{1.8}$$

where the first term is the contribution from the surface (s) and the second term is the contribution from all layers. The emissivity with respect to a particular absorbent can be expressed as:

$$\epsilon = k_\nu \rho r dz \tag{1.9}$$

where k_ν is the mass absorption cross section, ρ is the density of the absorbent, r is its mass mixing ratio and dz is a small increment in distance travelled. Substituting equation 1.9 into equation 1.8 and generalising using the integral form gives:

$$I_\nu = B_{v,s}(T_s)\tau_{\nu,s}\epsilon_s + \int_0^\infty B_{v,z}(T_z)w_\nu dz \tag{1.10}$$

where the weighting function (w_ν) is:

$$w_\nu = \tau_{\nu,z} k_\nu \rho r \tag{1.11}$$

As w_ν is the contribution from an atmospheric layer of unit thickness at level z to the radiance received at the TOA it can also be expressed as the derivative of the

transmittance of the overlying layer:

$$w_\nu = \frac{d\tau_{\nu,z}}{dz} \tag{1.12}$$

Weighting functions are commonly used in remote sensing to approximate the altitude or pressure level that emits the peak amount of radiation in a certain channel. They are derived for clear-skies, as the presence of an opaque cloud above the peak would shift the level of emission to the cloud top.

1.1.6 Brightness Temperature

Brightness Temperature is a concept that is regularly used in the observational fields of remote sensing and astronomy as an alternate measure of spectral radiance intensity for a single, or narrow band of wavenumbers. It is defined as the temperature that a black-body in thermal equilibrium with its surroundings, would need in order to duplicate the observed spectral intensity of radiance at a particular wavenumber. It is given by inverting equation 1.2 to produce:

$$T_b = \frac{c_2}{\frac{1}{\nu}\ln\left(\frac{c_1}{B_\nu \nu^{-3}} + 1\right)} \tag{1.13}$$

This does not correspond to the true temperature of the emitting body because the black-body concept assumes an emissivity of 1. Substituting B_ν for I_ν/ϵ_ν (equation 1.5) in this equation and inserting a real emissivity value that is less than 1, for the same measured intensity produces a higher temperature for the emitting surface. Hence brightness temperatures should be taken as the lower bound of the true temperature. Emissivity values in the longwave region are spectrally and surface type dependent but tend to exceed 0.9 for most surfaces (e.g. see Capelle et al. (2012)), and hence the difference is only a few kelvin, which gives a good approximation of the true temperature for most purposes. The exception to this is the far infrared region below 645 cm^{-1}, where recently values as low as 0.8 have been estimated from radiative transfer models (Feldman et al., 2014), which highlights the need to include accurate emissivity values in radiative transfer calculations, particularly in this spectral domain.

1.2 Global climate models

Climate is the weather conditions that prevail in an area over a long period of time. It could be considered the primary influence on humanity in terms of health, agriculture, ecology, economics, politics and environment, to name but a few, e.g. see Patz et al. (2005) and Hulme et al. (1999). This is made evident when weather conditions deviate from the normal mode that a region has come to expect, i.e. with extreme events such as floods, heatwaves and hurricanes, which can have catastrophic effects (Deschenes and Moretti, 2009; Weitzman, 2009). It is vitally important that the extent of the climate's variability can be quantified numerically in order to adapt to the most appropriate way of living alongside it, and climate models are designed to do this by predicting these numbers for the future, on timescales of decades or centuries. In order to do this a fully coupled climate model is needed. This is a model that describes the evolution of the atmosphere but is also linked to a model that describes the evolution of the ocean, and additionally can have components that describe the variability of sea-ice, land changes and systems of further complexity. The crucial feature that defines a coupled model is that, theoretically, they can run freely without any additional input, to give impartial predictions of future variables. Other types of models exist such as those that isolate a region of the globe, or a component of the climate system from all other parts (such as the atmosphere which is described Section 1.2.3), and are used for testing specific processes. This is achieved by applying known boundary conditions to the interfaces between components, which also makes them less computationally intensive.

1.2.1 Historical Development of Climate Models

At its core a climate model is a collection of atmospheric equations that describe the physical laws governing climate, consisting primarily of the hydrodynamic equations of motion and the laws of thermodynamics (Washington and Parkinson, 2005). The fundamental factor limiting climate model development historically is the need to use high performance computers to solve these equations for a large number of locations. Despite this, it was in the pre-computer era of the early 1900's that Norwegian physicist Vilhelm Bjerknes first set down the primitive equations that govern atmospheric flow and defined two broad conditions required for accurate climate

forecasting. These are firstly, that there is a sufficiently good knowledge of the state of the atmosphere at an initial time, and secondly, that there is an understanding of the physical laws from which one atmospheric state develops from another (Bjerknes, 1904). Bjerknes developed a qualitative method for solving the differential equations but without the technical tools at his disposal could not put his ideas to practical use. In 1913 Met Office scientist Lewis Fry Richardson developed Bjerknes's ideas by simplifying and approximating his equations to make them workable (Richardson, 2007), however his initial numerical forecasting attempts failed due to an omission of smoothing techniques, and few advances were made until the first computers were constructed in the late 1940's.

The first computer based climate model can be traced back to the 1950's, and was the work of Princeton scientists John von Neumann and Jule Charney on the first ever computer, ENIAC (Goldstine and Goldstine, 1946). It contained modifications of the primitive equations to fit the capabilities of the computer, whilst at the same time managing to produce results that did not deviate wildly with observations at the time (Charney et al., 1950). The first real global climate model that was considered successful, because it could realistically depict monthly and seasonal patterns in the troposphere, was developed by Norman Phillips at Princeton (Phillips, 1956). Since then advances in model abilities have often followed advances in computer technology, which has increased substantially over time (Chervin, 1988). However, it has been noted recently that improvements in spatial resolution have not kept pace with recent computational improvement (Slingo et al., 2009). The smallest building block of a climate model, the gridbox, is still typically not smaller than a hundred kilometres in the horizontal plane. Additional computing power has instead been diverted into incorporating more Earth system components, increasing the length of simulations and the emerging need for ensembles of simulations (multiple runs with the same initial conditions) to give more probabilistic estimates of future changes.

1.2.2 GCM Parameterisations

Even though climate models have progressed to the point where they can successfully reproduce the past and make predictions that have been subsequently confirmed by

observations (Huber and Knutti, 2014), fundamental challenges still remain. The limited spatial resolution presents challenges for the detailed representation of any processes that are on a smaller scale. These processes have to be approximated or 'parametrised' because, by definition, the gridbox is the limit of the models spatial resolution. Climate modals are still not at a level where weather systems such as tropical cyclones, or small-scale microphysical processes such as the growth of ice crystals or conversion of liquid cloud particles to rain droplets (Rotstayn, 2000) can be explicitly represented. Hence, these 'unresolved' physical processes are often expressed in terms of 'resolved' processes, such as state variables like temperature and gas concentrations. This is often done using statistical relationships which are based on empirical techniques. As such, parametrised processes are rarely based on theoretical principles and as a result have limited accuracy when different scales are considered, or conditions arise that are significantly different to those used when initially creating the relationship. Additionally, some subgrid processes, such as clouds, involve a level of complexity that means they cannot easily be expressed in this way. The uncertainty involved in making these parameter choices has led to the creation of a particular class of experiments called 'perturbed-physics' experiments and involve varying uncertain parameters in order to assess the models sensitivity (Collins et al., 2011; Yang and Arritt, 2002).

1.2.3 Atmospheric GCMs

Atmospheric-only GCMs (AGCMs) are GCMs that impose observed sea surface temperatures (SSTs) to the lower bound of the atmosphere, and hence provide a framework to test atmospheric processes. This removes the need for a separate ocean model. They can also be used to test if an atmospheric phenomenon, such as the Madden-Julian Oscillation, is naturally coupled to the ocean, as a comparison of AGCM results with an equivalent fully coupled run will deviate if this is the case (Inness and Slingo, 2003). Additionally, complicating factors such as errors in climate feedbacks are not able to develop internally when SSTs are continually being brought back to real values. This makes them appropriate for studying the models representation of clouds and radiation transfer on an instantaneous basis (Potter and Cess, 2004). The requirement for known SSTs means they need be run over the recent instrumental time period (Brohan et al., 2006).

1.2.3.1 HadGEM2-A

The GCM being tested in this project is the atmosphere-only configuration of HadGEM2. HadGEM2 is a family of climate models that forms part of the Met Office's unified weather forecasting and climate modelling system, MetUM (Martin et al., 2011) and was the UK's contribution to the IPCC fifth assessment report (AR5) published in 2013 (Collins et al., 2008). The time period under consideration in this thesis does not extend back any earlier than 2007, which is a limit set by the observations available, and most of the work focuses on the entirety of 2009, as it was the most recent completed year at the projects inception. This experimental set-up is designed to allow robust testing of the parametrisations of the atmosphere and radiation schemes, whilst avoiding the computational burden of coupling with Earth-system components and removing the need for ensembles.

1.3 All-sky Radiation and GCM Clouds

All-sky, or alternatively 'total-sky', is a term used in climate science to mean a world containing clouds, as opposed to the clear-sky, where various steps have been taken to identify and remove them. The reason such a definition exists is because of the difficulty in simulating clouds adequately in climate models and the common practice of using clear-sky data to isolate other climate variables, to the extent that it is necessary to indicate their inclusion. In addition to affecting the planetary energy balance directly with strong variability on global, diurnal and seasonal scales, clouds also act as a feedback mechanism on external radiative forcings, quantification of the latter being the largest source of uncertainty in general circulation models to this day (Chung et al., 2012; Randall et al., 2007; Soden and Held, 2006; Stephens, 2005). Clouds are difficult to parametrise due to their highly variable and small-scale effects, some of which are not yet adequately described by theory, requiring a higher level of detail that global climate models can currently provide. As the radiative effects of clouds may alter under climate change (Gregory and Webb, 2008), it is important that climate models are able to reproduce the current behaviour of both clouds and all-sky radiance, so an adequate description of their current effects is of the utmost importance.

In the observational world clouds can obscure other variables of interest, for example water vapour, from both the vantage points of the ground and top of atmosphere. Alternatively, when the variable of interest is the cloud, obtaining an adequate description of its properties is difficult as they are almost totally opaque to visible and infrared sensors and transparent to microwave sensors. Such is the need for detailed observations of the vertical structure of clouds together with longterm statistics that a constellation of satellites that fly one after the other in the same orbital plane, called the 'A-Train', was designed which has a collective approach to cloud resolving in response to these challenges (Stephens et al., 2002). It should be noted that the additional term 'cloudy-sky' is often used to mean the subset of data where all fields of view under consideration contain some fraction of cloud, whereas the all-sky incorporates both cloudy and clear-sky scenes.

1.3.1 Clear-sky Construction

In order to analyse the interaction of clouds with radiation it is useful to be able to compare the all-sky radiation (F_{all}) with the corresponding clear-sky situation (F_{clr}), and the difference should theoretically isolate their effects. This difference is defined as the cloud radiative forcing (CRF), or the cloud radiative effect (CRE), which is defined as:

$$CRF = F_{clr} - F_{all} \tag{1.14}$$

Globally in the longwave, this consists of a strong greenhouse trapping effect because most clouds absorb longwave radiation. Hence, there will be more outgoing clear-sky radiation escaping than all-sky and equation 1.14 will be a positive quantity. A disadvantage of the CRF is that it convolves any biases present in the all-sky and the clear-sky data within a single quantity, and additionally the latter is prone to biases due to the method of its construction. In the model world it is a technically easier task to remove clouds than in the observational world, however this has a knock-on effect on other model variables. Those profiles which are totally clear can be identified easily and retained while all other points are discarded (Method 1). Alternatively GCMs typically have the option of additionally obtaining radiation at every grid point without incorporating any of the clouds in the profile at little additional computational cost (Method 2) (Cess and Potter, 1987). Biases in the resulting radi-

ation are introduced using both these methods due to the correlation between water vapour and clouds. Method 1 will retain gridboxes that are un-representatively dry and Method 2 will incorporate the extra water vapour associated with a normal distribution of clouds. A recent study has estimated the difference between these two methods can be more than 5 Wm^{-2} or 10% of the total CRF (Sohn et al., 2010), however neither one can claim to be more realistic than the other. Intermediate solutions that involve threshold inclusion of gridboxes based on cloud fractions have been proposed in recent literature (Allan et al., 2003; Allan, 2009). This is discussed in more detail in Chapter 2, Section 2.2.7.3.

1.3.2 Cloud Parametrisation Schemes and Tuning

The macrophysical cloud quantities that are estimated via parametrisation techniques in GCMs are the mean values of cloud fraction and hydrometeor (ice or water particles) concentration (Randall et al., 2003). These are not calculated using explicit cloud physics, i.e. the Kohler theory of droplet growth, but are determined from the other state variables within the gridbox. Microphysics, such as the nature of cloud condensation nuclei has a bearing on the interaction of clouds with the radiation scheme, however, apart from some modifications associated with ice clouds, macrophysical cloud properties do not depend on these.

Parametrisation schemes tend to fall into one of two categories: 'diagnostic' or 'prognostic', though both often contain elements of the other (Bony and Emanuel, 2001). Diagnostic variables contain no memory of the previous timestep, being calculated through statistical relationships with other grid box quantities, e.g. humidity at that instant, whereas prognostic variables are explicitly predicted from various sources and sinks, e.g. advection, and are thus affected by the values on previous timesteps. Diagnostic schemes have recognised deficiencies such as being largely divorced from the rest of the model, and the tight coupling between cloud fraction and condensate can lead to errors in both quantities, however until recently the computational expense required for prognostic schemes was not available. Most modelling centres use diagnostic schemes, for liquid water clouds at least.

Adjustable parameters (usually scalars) that are part of these cloud schemes are commonly tuned to give the right radiation balance at the TOA, which can often be achieved by multiple combinations of these numbers. An obvious consequence of this is that the correct radiation balance could be achieved with a combination of parameter choices that produce inaccurate cloud properties, which could have a undesirable knock-on effect on other variables that derive from them. Hence, it is important that the selected combination remain plausible, and is rigorously tested. A popular choice is the autoconversion threshold radius, whereby a threshold mean cloud droplet radius is specified which converts cloud water to rain once exceeded (Rotstayn, 2000). It is not unusual for a value to be selected that is far lower than observations support (Larson et al., 2001). A recent study tested 3 combinations of selected cloud parameters, tuned to the same TOA radiation targets and found that the time evolution of temperature rise from pre-industrial times to present day were significantly different between configurations, with the most unrealistic value of autoconversion threshold radius giving the most realistic temperature rise (Golaz et al., 2013). This inconsistency is attributed to compensating biases within the climate model tested, and it is suggested that this is a common feature amongst climate models (Suzuki et al., 2013).

1.3.3 Climate Model Clouds: Analyses

An international effort has arisen in response to the need for a consistent standardised framework to evaluate climate variables calculated by the range of GCMs that exist worldwide. This is called the Coupled Model Intercomparison Project (CMIP), the latest phase of which is CMIP5, and involves 20 modelling groups (Taylor et al., 2012). Specific experiments with defined outputs are defined for every participating centre to run and submit to a common database[2]. This has allowed common trends and problems amongst all models to be identified, and to assess progress since the previous phase, CMIP3 (Meehl et al., 2007).

It has consistently been identified that there is a general tendency for climate models to underestimate low cloud cover with respect to observations (Webb et al., 2001). Another widespread problem in these regimes is the over prediction of optical thick-

[2]Data can be accessed at http://cmip-pcmdi.llnl.gov/cmip5/

ness, leading to an over reflection of incoming shortwave radiation. This is sometimes termed the 'too few, too bright' cloud problem, and the compensating behaviour between these two biases cancel to produce reasonable values of simulated TOA flux with respect to observations (Nam et al., 2012). Klein et al. (2013) point out that overall this bias has been reduced in the recent CMIP5 experiments, with the best models eliminating it completely. However, the authors also state that little improvement has occurred in terms of the vertical or climate regime distribution of cloud amount, a result also found by Lauer and Hamilton (2013) with respect to overall cloud climatology. The latter perform an equivalent analysis with atmosphere-only GCMs and find similar biases, isolating the treatment of subgrid scale cloud processes as the reason behind such errors. Jiang et al. (2012) show that in most GCMs the vertical structure of cloud water content and water vapour exhibits the largest uncertainty at upper tropospheric levels, and upper tropospheric ice clouds are worse simulated than lower or middle tropospheric liquid clouds, yet in general, results have improved since the earlier CMIP3.

It has been pointed out that evaluation of standard cloud diagnostics can be misleading. Examining mean cloud profiles convolves individual errors in the frequency of occurrence, amount when present and timing of appearance, which can all compensate to give good agreement in the mean (Morcrette et al., 2012). Additional compensation also frequently exists between the longwave and shortwave cloud radiative effects, for example high clouds exert a strong effect on longwave radiation but have little effect on the shortwave domain, whereas the opposite is true for low clouds (Kay et al., 2012). It is crucial that future studies attempt to decompose these hidden cancellations.

1.3.3.1 HadGEM2 Cloud Evaluation

A recent evaluation of simulated cloud cover in 21 GCMs with International Satellite Cloud Climatology Project (ISCCP) observational data (Rossow and Schiffer, 1991), found that HadGEM1 (whose cloud scheme is unchanged to that in HadGEM2) consistently produces a total column cloud fraction that is around 15% too low between 60 °S and 60 °N (Probst et al., 2012). An alternative cloud fraction dataset based on the High Resolution Infrared Radiation Sounder (HIRS) instruments detects more

thin clouds than ISCCP (Wylie et al., 2005) and therefore 15% could be considered a conservative estimate, with actual differences being much larger. Martin et al. (2011) examined various tropospheric metrics in HadGEM2-A and found that total cloud, along with precipitation, were significantly worse in terms of correlation and RMS bias than all other variables, including OLR. However, Nam et al. (2012) states that HadGEM2 reasonably reproduces observations of low clouds layers under 4 km, one of a handful of models that does in the CMIP5 group, because it is sensitive to environmental conditions and produces a better transition between low-cloud types.

1.3.4 HadGEM2 Cloud Parametrisations

Like most GCMs, HadGEM2 parametrises stratiform or 'large-scale' cloud separately to convective cloud. It is assumed there is no overlap between them. The parametrisation of large-scale and convective cloud in HadGEM2 is described in the following sections.

1.3.4.1 Smith Diagnostic Scheme

Although a prognostic scheme known as 'PC2' (Gregory et al., 2002; Wilson et al., 2008) has been designed for the Met Office models with the intention of replacing the diagnostic scheme in the forthcoming HadGEM3 model (Hewitt et al., 2011), the Smith scheme is the standard configuration used in HadGEM2. It is a diagnostic statistical scheme that parametrises large-scale liquid cloud (Smith, 1990), see Morcrette et al. (2012) for a description of both schemes.

If the model contained no cloud fraction parametrisation at all, each gridbox would have a value of saturation specific humidity (q_{sat}), which depends on the temperature (T), and a value of specific humidity (q) depending on the water vapour concentration (Figure 1.4). If $q > q_s$ there would be 100% cloud cover and if $q < q_s$ there would be 0% cloud cover. Relative humidity (RH) is equal to:

$$RH = \frac{q}{q_{sat}} \times 100 \tag{1.15}$$

hence if $RH > 100\%$ the box is cloud covered because grid scale supersaturation has

been reached, and if $RH < 100\%$ the box is clear-sky.

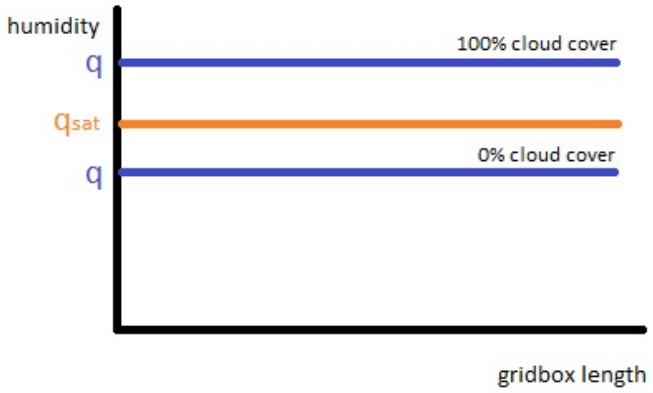

Figure 1.4: Schematic of the humidity in a model gridbox with no cloud fraction parametrisation. There is one value of saturation specific humidity q_{sat} and one value of q at each timestep, resulting in either 100% cloud ($q > q_s$) or 0% ($q < q_s$) with no other possible values. Specific humidity q is taken to be the mass of water vapour in a unit mass of moist air.

In order to obtain a value for fractional cloud cover, variability about the mean humidity values must be applied, hence even if the mean value of the specific humidity is below the saturation specific value a proportion of the distribution could exceed it (the blue curved and orange curved lines in Figure 1.5). This means that even when $RH < 100\%$ there can be some cloud cover. This variability is parametrised by a probability density function (pdf) of q_{total} (total water content, water + vapour) around the mean, the shape of which must be decided upon. The Smith scheme has a symmetric triangular PDF.

Clearly there should be no clouds when RH approaches 0% so a critical relative humidity (RH_c), is defined below which no clouds can form and makes it a relative humidity scheme (Sundqvist et al., 1989). RH_c is set at 85% for all but the lowest two model layers which have values of 92.5%. HadGEM2 includes modifications by Cusack et al. (1999) to relate the RH_c in a gridbox to the conditions in the 3x3 network of gridboxes around it, which replaces the original value. There are also modifications applied to better represent thin clouds vertically, by interpolating

cloud properties into 3 sublayers, rather than assuming the cloud completely fills the gridbox in the vertical.

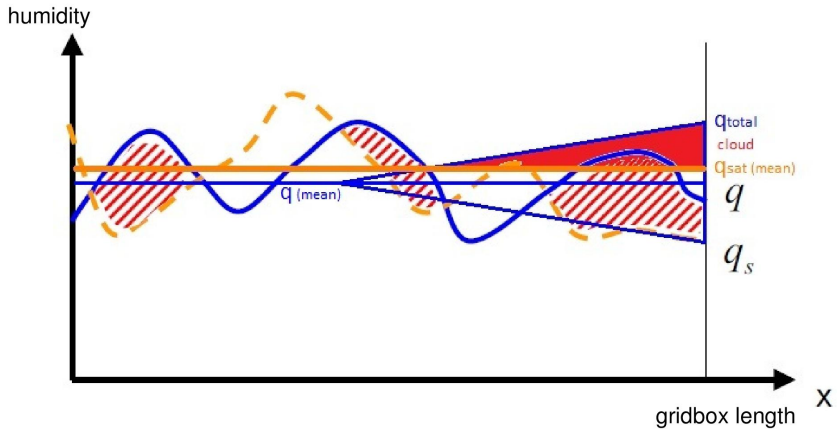

Figure 1.5: The basis of the Smith diagnostic cloud scheme. Schematic of humidity (ordinate) in a model gridbox with variability about the mean values of q and q_{sat}. The variability of q about $q_{(mean)}$ is represented with the blue curved line. The orange dotted line is the variability of q_{sat} about $q_{sat(mean)}$. When q exceeds q_{sat} there is local cloud creation (red diagonal shaded regions). A triangular pdf is the form of the parameterisation that described this behaviour statistically. The area shaded red represents the cloud fraction as it is the portion of q_{total} that exceeds q_{sat} in the pdf.

The scheme uses an assumption of instantaneous condensation once RH_c has been exceeded and liquid cloud fraction is determined diagnostically from q_{total}, RH_{crit} and temperature. The phase of the cloud (liquid or ice) is determined using a linear temperature function. If the temperature is above 0 °C then the cloud is considered to be liquid, if it is below 9 °C it is ice, and for anything in-between a linear fit is assumed for the fractional division of condensate into liquid and ice.

Ice content is calculated separately using a prognostic ice microsphysics scheme which advects ice around the model, developed by Wilson and Ballard (1999). One reason for this is because the instantaneous condensation assumption is not justified for ice,

which can take tens of minutes to adjust to equilibrium. The ice cloud fraction is diagnosed from the ice concentration using a similar relationship that exists between liquid clouds fraction and liquid concentration. Liquid and ice cloud are assumed to be minimally overlapped, so only when their total combined fraction exceeds 100% will there be any. HadGEM2 does not consider rain to be included in its liquid cloud, which is modelled to fall out as soon as the autoconversion occurs, but is one of only two models in CMIP5 that considers falling snow as part of the ice cloud in the layer it falls through.

1.3.5 Gregory-Rowntree Convection Scheme

The parametrisation of convective cloud is based on the mass-flux scheme of Gregory and Rowntree (1990). At its core, the scheme assumes a single plume and calculates the mass change of an updraught due to various entrainment and detrainment mechanisms. HadGEM2 contains a new 'adaptive detrainment' scheme, which links mass flux more closely to the parcel buoyancy profile, significantly improving it's shape (Derbyshire et al., 2011). The convective cloud fraction is based on a logarithmic relationship with the convective rain rate, which gives it a maximum fraction of about 40%. However, the scheme contains major modifications to include anvil effects (Gregory, 1999). An anvil is the upper ice part of a deep convective cloud that has spread out under the tropopause. When the convective cloud exceeds a depth threshold of 500 hPa between top and bottom, has its base in the boundary layer, and the cloud top temperature is less than 0 °C, then the anvil scheme is applied as follows. The anvil base is defined as the freezing level and the cloud is split into two parts, the tower and the anvil. A 'tower factor' of 0.25 is applied to the convective fraction below the freezing level and an 'anvil factor' is applied above, which has the effect of multiplying the upper fraction by up to 3 times its initial value. As this last step could produce cloud fractions of over 100% this has to be capped. Convective cloud water (CCW) is diagnosed from the convective cloud fraction. HadGEM2 specifies a maximum allowed CCW, after which the scheme will precipitate. This threshold is 10 g/kg which corresponds to approximately 0.08 g/m^3, and is about 5-30 times smaller than typical observed values of CCW (0.5 g/m^3 - 3 g/m^3).

The convective scheme has previously been highlighted as suffering from structural

deficiencies, such as the poor representation of the diurnal cycle of convection over tropical land associated with the general difficulty in simulating convective detrainment (Yang and Slingo, 2001). A recent study by Morcrette et al. (2012) showed that clouds are often underestimated in the latter half of the day, due to convective activity peaking too early at noon, whereas in reality this peak is between 18:00 and 21:00. Despite significant error reductions over HadGEM1 due to the inclusion of the new adaptive detrainment parametrization (Martin et al., 2011), and further related implementations such as the depth criterion for shallow convective clouds being removed, the level of sophistication in the representation of the convective cloud in HadGEM2 is still not as good as the large-scale scheme and improvement is an ongoing process (Stratton and Stirling, 2012).

1.3.6 Radiation schemes

The treatment of radiative transfer in GCMs involves a balance between accuracy and computational efficiency, particularly in the case of terrestrial radiation as the absorbing properties vary considerably with wavelength. Due to the computational expense required it is not practical to resolve upwards of 100,000 lines in the spectrum explicitly by using a line-by-line (LBL) code, hence 'band models', which group together spectral lines with common characteristics and make certain approximations, have been developed to make calculations faster (Davies et al., 1987). This is sometimes done by grouping lines which are adjacent to one another into small enough bands that the variation of the Planck function (Equation 1.2) across it is considered negligible. Other techniques involve reordering the wavenumbers in a band, based on their absorption characteristics, such as the 'correlated-k' method (Mlawer et al., 1997). For an overview of the different radiation parametrisations that can be used in climate models see Stephens (1984). Generally a database which contains molecular absorption coefficients for atmospheric constituents such as CO_2 and O_3 is used to generate transmissions over each gas on a LBL basis offline. An example of which is the HITRAN database (Rothman et al., 2005). Parametric relationships for each band are created using these values, which are used to generate radiances during a climate model run.

The first successful implementation of a banded radiative transfer code in a climate

model was in 1975, and comprised 19 bands in the infrared (Fels and Kaplan, 1975). All climate models now contain parametrised treatments of radiative transfer and LBL output provides a useful benchmark with which to test these modified schemes, as they typically contain bands which are wider than 100 cm^{-1}. An international program for the Intercomparison of Radiative Codes in Climate Models (ICRCCM) was set up for this purpose (Ellingson et al., 1991). It has been shown that LBL codes tend to agree with one another well, while climate model codes can deviate from each other by up to 10-20%. Systematic errors can arise in situations when economies are made in the vertical or spectral resolution, or when the water vapour continuum is not represented sufficiently (Morcrette and Fouquart, 1985). When radiation schemes were first implemented in climate models it was common to neglect scattering in the longwave region by atmospheric particles such as clouds and treat them as purely absorbing, because scattering is less important and can be complex to represent (see Section 1.1.3). However, this omission has been shown to introduce biases of up to 20 Wm^{-2} for individual clouds (Ritter and Geleyn, 1992), and hence scattering has recently become parametrised in most climate model radiation schemes.

1.3.6.1 Edwards-Slingo Radiation Scheme

The radiation code used by HadGEM2 is the Edwards-Slingo radiation scheme (Edwards and Slingo, 1996), which parametrises radiative fluxes using a 'two-stream' approximation (Meador and Weaver, 1980). It is a very flexible scheme with options for several user defined choices. For HadGEM2 it solves for 6 wavebands in the shortwave and 9 in the longwave. Within a band, all quantities except for the gaseous mass absorption coefficient are treated as independent of frequency. A further number of 'quasi-monochromatic' divisions are specified in this band, within which the gaseous absorption coefficients for all active gases have fixed values. As the scheme only resolves in the vertical direction, it estimates fluxes directly instead of calculating radiances (see Section 1.1.2.1 for the distinction). For the infrared, the angular variation is parametrised through diffuse vertical beams, and azimuthal symmetry is assumed.

The scheme deals with matter interaction by defining 3 single scattering properties on a layer: optical depth, single scattering albedo (the ratio of scattering efficiency to

total extinction) and asymmetry. Together these determine the overall transmission and reflection coefficients. The form of the parametrisation between these two sets of quantities can be specified by the user, and options include the Eddington approximation (Joseph et al., 1976) or the Practical Improved Flux Method (PIFM) by Zdunkowski et al. (1980). The parametrisation of angular processes is further modified by applying a 'δ-rescaling' to the single scattering properties to increase the forward scattering, which approximates observations more closely. Optical depth and single scattering albedo are calculated from the mass extinction (k^e) and mass scattering (k^s) coefficients which are summed from individual processes due to interaction with various gases, aerosols and clouds. Line transmission data is taken from the GENLN2 LBL model (Edwards, 1992) which uses the HITRAN2004 molecular database (Rothman et al., 2005).

A particular parametrisation, e.g. Slingo and Schrecker (1982) or Ackerman and Stephens (1987), defines the relationship between the mass mixing ratio and effective diameter/radius of cloud water droplets D_e, and k^e and k^s, which can then be included in the flux calculation. The physical basis of effective diameter can be understood in terms of effective photon path, and depends on ice water content and size distribution ($N(D)$) (Mitchell et al., 2011; Mitchell, 2002). Originally D_e was set at a constant value of 7 μm but was developed later to vary in relation to the number of cloud condensation nuclei in the gridbox. For ice clouds, the treatment is not quite as simple due to the irregular shape of ice crystals. An earlier atmospheric version of the Met Office's Unified Model, HadAM3, used a similar scheme to water clouds with a D_e of 30 μm, however in the intervening time more elaborate schemes that define a parameter based on ice crystal size and surrounding temperature have been introduced such as those described by Mitchell et al. (1996), Fu (1996) and Fu et al. (1998). The criterion of whether any convective cloud in a gridbox is to be treated as ice or water particles by the scheme is described by Bower et al. (1996) and is based on the surrounding temperature, with boundary conditions that specify it is not water cloud below -40 °C and not ice cloud above 0 °C.

There are two treatments of the macrophysical properties of clouds in the Edwards-Slingo code; the single column approach and the Monte Carlo Independent Column Approximation (McICA). In the single column approach clouds are plane parallel and

do not vary over the vertical extent of a gridbox. Clouds are split by fraction into either a clear and a total cloud fraction; or a clear, stratiform and convective cloud fraction. Overlapping only happens in the vertical between layers and is treated by coefficients used to couple fluxes at the boundaries between them. The variability of water content is parametrised by multiplying it by a scaling factor which is different for each cloud type. In the McICA scheme the variability of the radiative effect of subgrid cloud water content is explicitly represented. A vertical column is split into subcolumns that are either totally clear or totally cloudy depending on the vertical cloud profile. The Monte Carlo approximation for the columns chooses a random subcolumn to perform the radiative calculations, and is described in Hill et al. (2011). The McICA scheme is currently only available when convective cloud is switched off in the model.

1.4 Evaluating Models with Satellites

Figure 1.6 illustrates the basic concept of this thesis by showing satellite measurements overlying a model grid. Satellite instruments record ungridded radiances over a wide swath, whereas climate model data is produced at set grid points at defined time intervals. In order for the two to be compared, both datasets must be processed so they are spatially, spectrally and temporally consistent. Note that the grid shown is 4 times courser than the resolution of HadGEM2 for clarity.

1.4.1 Satellite Instruments

Satellites carrying instruments for meteorological and climate purposes have been launched into Earth's orbit since the 1960's (Allison and Warnecke, 1965). Over time a large and diverse network has developed that provides a rich scientific resource for present day evaluations. Space borne instruments record radiances from either geostationary, or polar orbits - so-called because they pass near to both poles in every revolution. The type of orbit determines what the data is suitable for.

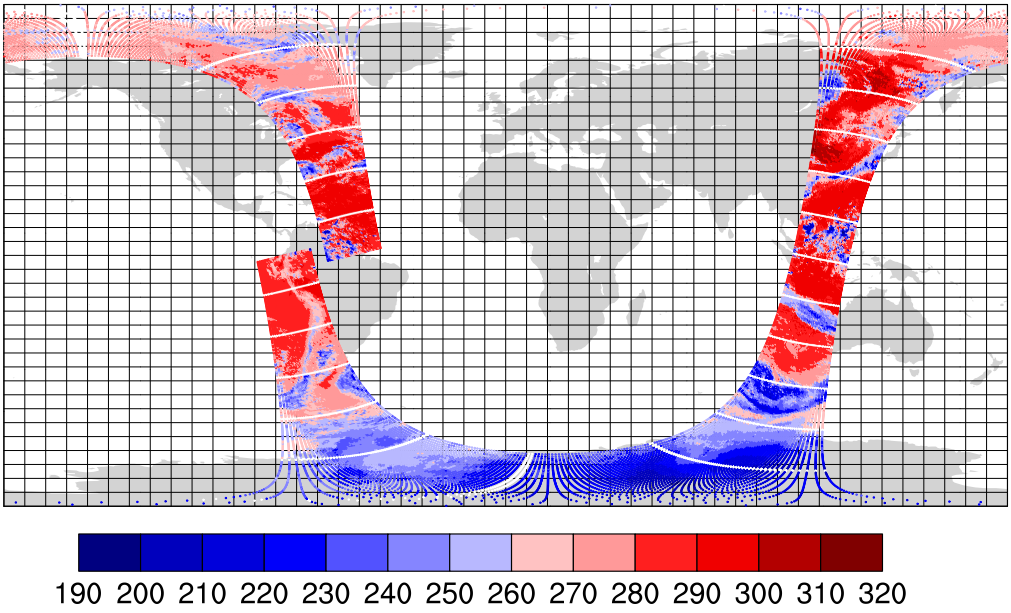

Figure 1.6: Geolocated brightness temperature measurements for wavenumber of 900 cm^{-1} (window region) for a complete polar orbit. Observations are taken from the HIRS instrument on the MetOp-A satellite (described in Chapter 2, Section 2.2.3) from 1st July 2009. The global grid has a resolution of 5 ° latitude by 7.5 ° longitude. The white gaps in the measured data are from when the instrument looks at its calibration target. Units are Kelvin.

1.4.1.1 Sun-Synchronous Polar Orbits

A polar orbit is a low earth orbit, typically occupying a position in the exosphere, where the atmospheric density is so low that any molecules do not collide with one another, thus it is effective for observing the TOA. Remote sensing for this purpose typically exploits a particular type of polar orbit that is known as sun-synchronous. These orbits take advantage of the particular altitude and inclination of the satellite that means it will pass over the same ground-based latitude at the same local time every time. This results in an orbital plane which is at constant angle with respect to the Sun, while the Earth revolves beneath it (Figure 1.7).

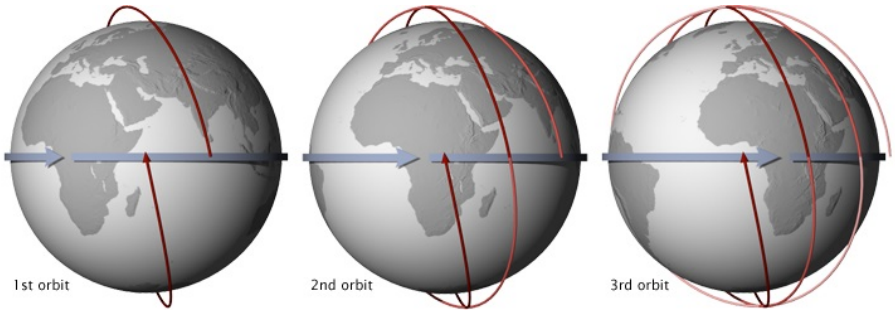

Figure 1.7: 3 sun-synchronous orbits (red arrows). As the Earth revolves in the direction of the blue arrows the orbit maintains the same local time profile for every circumnavigation.

Typical sun-synchronous orbits are at an altitude of between 800 - 900 km above sea level, and have inclinations around 98°, which gives a time period of 96 - 100 minutes, resulting in just over 14 orbits a day. This orbit has the advantage of near global coverage which is useful for studying climatological variables on a global and yearly timescales. However, the analysis is restricted to just 2 local times for either the descending or ascending mode, with a 2 hour time window around them for the majority of the ±65° band. This is the opposite behaviour to geostationary satellites which sense the entire diurnal cycle, but are restricted to one equatorial location.

1.4.1.2 Infrared Sensors

Satellite instruments can only measure quantities relating to the photons that strike their detectors, such as energy or wavelength. They cannot directly describe in-atmosphere geophysical properties such as temperature or gas concentrations as they are remote. Depending on the mechanism by which they achieve this they can be classified as either active or passive. Active sensors send out pulses of radiation such as light waves (lidar) or radio waves (radar) and measure the signal that bounces back to the instrument, whereas passive sensors record the naturally occurring radiation striking the detector.

In the infrared region passive sensors are used. The first, and most basic, passive sensor to be designed was the radiometer (Combs et al., 1965). It quantitatively

measures the intensity of photons striking a detector in single or multiple wavelength bands called channels. Incoming energy is filtered typically by a combination of beam-splitters and optical filters, which when mounted on a rotating wheel can be timed accordingly to record the intensity in a particular channel. They are cooled to temperatures well below freezing to minimise self-emission and produce a change in voltage when struck by a photon which is proportional to the difference in radiance of the target and a black-body reference source. For more detail on radiometer technology with application to the HIRS instrument see Chang and Cao (2014). When observing across a much larger quantity of channels an alternate method is required because it is not practical to separate each one with an individual filter. Interferometers can be used to split and superimpose waves from the original beam to produce an interferogram. A Fourier Transform Spectrometer (FTS) then inverts the interferogram to extract the intensity of each wavelength that comprises the infrared source. For more detail on interferometer technology with application to the Infrared Atmospheric Sounding Interfermeter (IASI) Instrument see Simeoni et al. (2004).

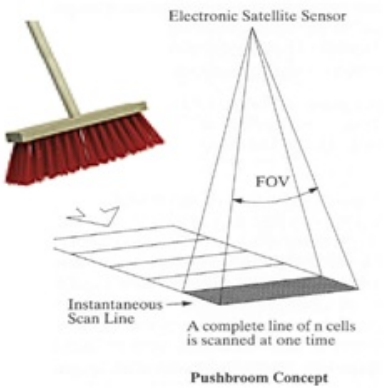

Figure 1.8: Pushbroom Scanner

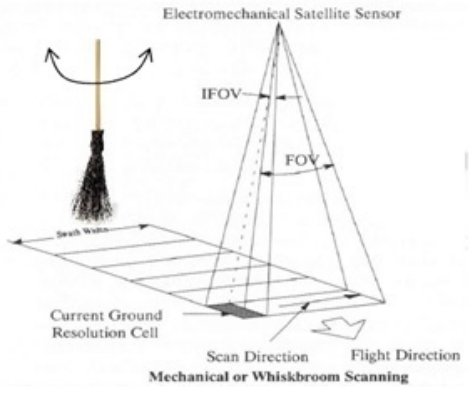

Figure 1.9: Whiskbroom Scanner

In order to observe as much of the atmosphere as possible in the horizontal plane, instruments are often designed with a system that also senses in the direction perpendicular (across-track) to the forward movement of the sensor. One way of achieving this extra coverage is to use a fixed linear array of sensors that are fanned out in a 'push broom' arrangement (Figure 1.8). This has the advantage of constantly recording at a particular angle, but is subject to varying sensitivities between its

sensors. Another option that circumvents this issue is to use a moving mirror that sweeps back and forth in the across-track direction to direct radiation into a single detector, recording at equally spaced angles over a single swath. This arrangement is called a 'whisk broom' scanner (Figure 1.9). A disadvantage of this type is it is potentially subject to problems associated with the moving parts.

Instruments either disseminate their information to ground stations at regular intervals in their orbits, or provide direct readouts at near real-time. Obtaining radiance values from the raw digital counts measured by the instrument is a complex process involving the processes of: geolocation, correcting for spacecraft pointing errors, calibration with respect to internal or external targets with known temperatures, accounting for degradation of antenna and other parts, correcting for self-emission of the instrument and correcting for the spectral response functions of the channels. Depending on the number of these processes that have been completed the radiance product will be assigned a 'level' and distributed by satellite centres such as NOAA[3] or EUMETSAT[4]. The satellite products used in this thesis to evaluate HadGEM2 are detailed in full in the chapters they relate to.

1.4.2 Satellite-Model Comparison

Satellite instruments in sun-synchronous orbits are powerful tools for climate model evaluation due to their near global coverage and longevity, typically spanning a time period of at least 5 years. For trend analysis however, a decadal climate record is needed. In the absence of continuous measurements with the required length, radiances can be inter-calibrated between instruments on different satellite platforms, which with earlier satellites involves correcting for problems associated with orbital drift (Shi and Bates, 2011). Spatially, the regularly precessing orbit only samples the same point on Earth at certain intervals, about once every 5 days at the equator with frequency increasing towards the poles. Combined with the limited local time sampling introduced in Section 1.4.1.1 these 'orbital sampling' issues must be accounted for in the model world, to avoid systematic biases (Guan et al., 2013). Additionally, the differences in footprint size between a satellite pixel and a climate

[3]http://www.ncdc.noaa.gov/
[4]http://www.eumetsat.int/website/home/Data/index.html

model gridbox should be considered when comparing the two (Huang et al., 2007b). Compositing days and months of data are common methods of enabling comparisons with models to be made and requires consideration of consistent averaging methods. Fortunately, the level of sophistication of instruments in the last 50 years has consistently improved, resolving increasingly finer details, and the wealth of instruments that now exist with overlapping spectral regions provides the opportunity for comparisons/verifications between instruments, either on the same platform or at points of orbital cross-over. Once launch has occurred successfully satellites experience relatively little in-situ problems compared with ground based instruments due to the lack of atmosphere in orbit. However when a problem does occur it can be problematic to fix or sometimes even to diagnose due to its remote nature (e.g. see Hewison and Muller (2013)).

Satellite observations can be used to evaluate climate models via one of two methods. The first, and most conventional, method is to create 'model-equivalent' variables from observations, which are known as retrievals. The second is to create 'observational-equivalent' variables by simulating radiances from climate model data in a model-to-radiance approach (Morcrette, 1989). Both methods contain uncertainties. For retrievals quantities relating to clouds and precipitation can be particularly difficult to quantify because of the difficulty in identifying these variables in a satellite's field of view (Stephens and Kummerow, 2007). Complex inversion algorithms are also needed to retrieve the corresponding geophysical variables from the atmosphere. Alternatively with the forward model method, the quality of simulated satellite-like radiances is dependent on the radiative transfer code, for which certain limitations exist (Pincus et al., 2012). Recently there has been an increase in satellite-simulators developed for this type of evaluation in order to represent new satellite instruments in orbit. As this method deals with the forward problem it can be thought of as the more direct approach to model evaluation as it doesn't have to deal with inversion equations (Bodas-Salcedo et al., 2011). For this reason, the model-to-radiance approach is adopted for this thesis.

1.4.3 Model-to-radiance approach

Longwave satellite observations can be either, broadband: a single channel spanning the entire longwave region, narrowband: comprising a small number of channels that are not necessarily spectrally adjacent, or hyperspectral: upwards of 1000 channels with fine spectral resolution. The first of these can be compared with conventional climate model output if the broadband satellite radiances are converted to flux. The two remaining types require a dedicated satellite simulator to produce the equivalent radiances from climate model data. Satellite simulators are comprised of Fast Radiative Transfer Models (FRTM) which are specifically designed for the satellite instrument in question. An FRTM is a computationally efficient modification of a LBL code and the feature that makes the radiative transfer code 'fast' is the use of regression techniques to approximate parts of the radiative transfer equation. Regression coefficients are calculated from LBL output for quantities such as transmittances which are stored inside the FRTM to drastically reduce the number of internal calculations performed.

1.4.3.1 Broadband Evaluations

The Earth Radiation Budget (ERB) instrument that flew onboard the 7 Nimbus satellites from 1964 was the first satellite instrument employed in a model-to-radiance evaluation. OLR data complied by Ellis and Vander Haar (1976) was used by Cess (1976) in a pioneering study that tested the climate sensitivity of the Budyko (1969) and Manabe and Wetherald (1967) pre-satellite era climate models. This data broke new ground by providing empirical constraints for radiative fluxes simulated by global climate models, e.g. see studies by Stephens et al. (1981) and Slingo (1982), and reviews by Hartmann et al. (1986) and Ramanathan (1987). Motivated by a need to more fully sample the diurnal cycle of radiation on smaller spatial scales, the ERB project was succeeded by the Earth Radiation Budget Experiment (ERBE) in 1984 (Barkstrom, 1984), and the improved set of global spaceborne flux observations yielded is still used by modelling communities in GCM studies to this day. For example, Kiehl and Ramanathan (1990) and Kiehl et al. (1994) evaluated the National Center for Atmospheric Research (NCAR) Community Climate Model 2 (CCM2), Barker et al. (1994) combined ERBE with ISCCP data to assess the Canadian Climate Centre (CCC) GCM and Ringer and Allan (2004) compared similar

observations with mean OLR over tropical oceans simulated by HadAM3.

The most recently developed broadband satellite instrument in operation is the CERES instrument which was first launched in 1997 (Wielicki et al., 1996), and was designed as an improvement over the ERBE scanner instruments, but is often used alongside them. The observed OLR has been widely used to validate GCMs, e.g. testing HadAM3 decadal variability (Allan and Slingo, 2002), the diurnal cycle (Smith et al., 2008) and averaged radiative quantities in HadGEM2 (Martin et al., 2011). A recent comparison of broadband radiative fluxes from 12 GCM simulations from the Atmospheric Model Intercomparison Project (Taylor et al., 2012), with CERES EBAF data revealed little similarity between models in terms of sign and magnitude for both clear and all-sky biases, with global means ranging between -9 and 4 Wm^{-2} (Wang and Su, 2013). Similarly, the OLR produced by 16 GCM's in a historical 20th century CMIP5 simulation compared against CERES-EBAF data yielded a similar range of global biases, and additionally showed regional errors ranging from -25 to 30 Wm^{-2} (Li et al., 2013). Most of the models tend to overestimate OLR in the strongly convective regions of the tropics.

1.4.3.2 Spectral Evaluations

Splitting the OLR into isolated wavelength bands is a less common, but potentially more insightful, method of testing climate models (Slingo and Webb, 1997). Numerical Weather Prediction (NWP) models have been subjected to such narrowband tests in the past, where often the spectral region considered is the so-called window band, e.g (Morcrette, 1989, 1991). Rizzi (1994) compared brightness temperatures from HIRS/2 window channel 8 with the equivalent simulated data from the ECMWF model and found global biases exceeding 4 K, whereas comparisons of channels in the CO_2 and water vapour ν_2 bands did not exceed 2 K. NWP results tend to indicate that model simulations in the presence of clouds overestimate longwave emission in window regions (Chevallier et al., 2001; Chevallier and Kelly, 2002; Amorati and Rizzi, 2002).

A recent GCM study made use of spectrally resolved radiances from the hyperspectral Atmospheric Infrared Sounder (AIRS) to test the Geophysical Fluid Dynamics

Laboratory GCM (GFDL version AM2p13), concluding that broadband tests may show agreement that conceals compensating errors in different wavelength bands (Huang et al., 2007a). It is proposed that 'tuning' cloud related parameters in order to force model-simulated all-sky broadband OLR to match observations may leave significant biases of opposite signs in different spectral regions that cancel to give a better overall result. Similarly Huang et al. (2006) performed a spectrally resolved comparison for the clear-sky using the Infrared Interferometer Spectrometer (IRIS) data from 1970 whilst also making the point that tuning using cloud related parameters can mask errors in geophysical quantities in the all-sky, that will be exposed in a clear-sky only comparison. There is a need to see if other climate models stand up to the test of matching radiance observations when the longwave spectrum is broken down. Such results provide the initial tools needed for analysis of cloud feedbacks using a rigorous 'band-by-band' approach. Work in this area is emerging as a much needed test of climate models' abilities to reproduce the details of the radiation budget (Leroy et al., 2008; Huang et al., 2010; Kassianov et al., 2011; Huang et al., 2013).

1.4.4 The RTTOV Satellite Simulator

The Radiative Transfer model for TOVS (RTTOV) is a fast radiative transfer model originally designed to simulate the suite of atmospheric sounding instruments that make up the space borne TIROS Operational Vertical Sounder (TOVS) system. TOVS was part of the payload of NOAA's Television Infrared Observation Satellite - Next-generation (TIROS-N) series of polar orbiting satellites, the first of which was launched on 13 October 1978, and the last on 6 February 2009, with 15 successful missions over this time period. Over time the satellite platforms and sensors supported by RTTOV have expanded beyond the TOVS suite to include 27 satellite platforms and 47 instruments to date.

The first version of the model, RTTOV-3, was originally developed at the European Centre for Medium Range Forecasts (ECMWF) in the early 1990's (Eyre, 1991). It has since passed through several incarnations with each successive version allowing increasing numbers of input variables, the most recent of which is RTTOV-11 released in June 2014. The code is currently maintained through the EUMETSAT

Numerical Weather Prediction Satellite Application Facility (NWP SAF) led by the Met Office, and is available publically[5]. The model comprises a Fortran-90 code that can be run in forward, tangent linear, adjoint or K mode. The forward model takes a vertical distribution of atmospheric variables (the state vector) and calculates top-of-atmosphere radiances/brightness temperatures for each of the channels selected in order to simulate what the real satellite instrument would 'see'. The tangent linear, adjoint and K are routines concerned with calculating changes in TOA radiances give a perturbation in one or more elements of the state vector. The spectral range in the infrared is 3 - 20 μm (500 - 3000 cm^{-1}) and in the microwave is 10 - 200 GHz.

1.4.4.1 The RTTOV Radiative Transfer Equation

The top level form of the all-sky radiative transfer equation for infrared sensors at nadir views (removing viewing angle dependencies) using wavenumber notation is:

$$I^{all}(\nu) = (1 - N)I^{clr}(\nu) + NI^{cld}(\nu) \tag{1.16}$$

where $I^{all}(\nu)$ is the all-sky TOA upwelling radiance at wavenumber ν, $I^{clr}(\nu)$ is the clear-sky TOA upwelling radiance, $I^{cld}(\nu)$ is the cloud affected TOA upwelling radiance and N is the fractional cloud cover. The clear radiance $I^{clr}(\nu)$ is given by:

$$I^{clr}(\nu) = \tau_s(\nu)\epsilon_s(\nu)B(\nu, T_s) + \int_{\tau_s}^{1} B(\nu, T)d\tau \tag{1.17}$$

where the first term is the radiance from the surface s, and the second term is the layer to space radiance at the mean layer temperature T. τ_s is the surface to space transmittance, ϵ_s is the surface emissivity, τ is the layer to space transmittance and $B(\nu, T)$ is the Planck radiance for a scene temperature T (Equation 1.2). It is assumed that there is no reflected term over the infrared wavenumbers considered. The cloudy radiance I^{cld} is given by:

$$I^{cld}(\nu) = \tau_{cld}(\nu)\epsilon_{cld}(\nu)B(\nu, T_{cld}) + \int_{\tau_{cld}}^{1} B(\nu, T)d\tau \tag{1.18}$$

[5] `http://nwpsaf.eu/deliverables/rtm/`

where τ_{cld} is the cloud top to space transmittance and ϵ_{cld} is the cloud top to space emissivity. The second term accounts for all layer to space radiances above the cloud.

Two assumptions are made to simplify equations 1.17 and 1.18. The first is splitting the atmosphere into J layers where the mean layer radiance is given by averaging the radiation variables at the top and the bottom of the layer, where the total layer to space radiance is the sum of all the layers. This requires a sufficient number of layers so that each one can be considered approximately homogeneous. The second assumption is that for a single channel i these equations still apply when the channel is represented by the central wavenumber (McMillin et al., 1979). Within a channels spectral interval a satellite radiometer responds to radiation in a non-uniform way as a function of wavenumber, hence it is necessary to know the profile of responses for each channel. This is known as the spectral response function (SRF). This function can be normalised so that it represents a weight which can be applied to the channels central wavenumber to approximate the total integrated response over the whole channel. These weights are called band correction coefficients. These 2 assumptions modify equations 1.17 and 1.18 for each channel as:

$$I_i^{clr} = \tau_{i,s}\epsilon_{i,s}B(T_s) + \sum_{j=1}^{J_s} I_{i,j} + I_i^{'} \tag{1.19}$$

and

$$I_i^{cld} = \tau_{i,cld}\epsilon_{i,cld}B(T_s) + \sum_{j=1}^{J_{cld}} I_{i,j} + I_i^{''} \tag{1.20}$$

where $j = 1$ is the top atmospheric level descending to the layer above the surface J_s, or cloud top J_{cld}. $I_i^{'}$ is a small atmospheric contribution from the surface to J_s, $I_i^{''}$ is an interpolation of the radiance from the level below the cloud top and the level above it, and $I_{i,j}$ is:

$$I_{i,j} = \frac{1}{2}[B_i(T_j) + B_i(T_{j-1})](\tau_{i,j-1} - \tau_{i,j}) \tag{1.21}$$

where $B_i(T)$ is the modified Planck function that accounts for channel i's spectral

response function. Equation 1.2 is therefore rewritten as:

$$B_i(T) = \frac{c_1 \nu_i^3}{e^{\left(\frac{c_2 \nu_i}{a_i + b_i T}\right)} - 1} \tag{1.22}$$

where ν_i is the central wavenumber of channel i, and a_i and b_i are the band correction coefficients.

The generation of transmittances in RTTOV is a very fast stage. Optical depth d is calculated in the first instance which is related to transmittance τ by:

$$d = -\log \tau \tag{1.23}$$

Accurate LBL layer to space optical depths are found for a number of atmospheric profiles that sample a wide range of atmospheric conditions. This set of profiles is know as a 'training set' and the relationship between optical depth and the variables within the profile is used to produce a set of coefficients. These can be applied to any other profile to estimate its optical depths (Eyre and Woolf, 1988). In RTTOV-10 the Line-By-Line Radiative Transfer Model version 11.1 (LBLRTM) (Clough et al., 2005) is used together with continuum absorption from the Mlawer-Tobin-Clough-Kneizys-Davies version 1.4 (MTCKD) (Mlawer et al., 2012). The molecular database was created and refined based on results obtained by Matricardi (2007) and blends information from HITRAN2004, HITRAN2000 (Rothman et al., 2005) and GEISA2003 (Jacquinet-Husson et al., 2005).

Regression coefficients are computed separately for all gases and the combined transmittance is obtained as the product of the separate transmittances. This assumes that the spectra of the gases involved are not significantly correlated with each other, which is judged a tolerable assumption. Optical depth predictor coefficient files are provided within the RTTOV package with all combinations of gases that can be included as variable, to be specified by the user. The coefficient file selected decides how many predictors should be used.

1.4.4.2 Clouds in RTTOV

A new multiple scattering scheme was introduced in RTTOV-9 to take account of the extinction of radiation not only due to absorption, but also due to the scattering by aerosol and cloud particles. It is based on the parametrisation approach followed by Chou et al. (1999). The approach essentially works by scaling the optical depths on each level by a factor that accounts for backwards scattering and transmission between levels, and is known as the scaling approximation. It assumes that the diffuse radiance field is isotropic, which can be expected to introduce a degree of error particularly due to the natural heterogeneity of ice crystal shapes. The absorption optical depth in equation 1.5, rewritten as d_a is replaced by an extinction optical depth d_e given by:

$$d_e = d_a + bd_s \tag{1.24}$$

where d_s is the scattering optical depth and b is the integrated fraction of energy scattered backwards. RTTOV-10 uses The Optical Properties of Aerosols and Clouds (OPAC) (Hess et al., 1998) database for standard microphysical properties such as the size distributions and droplet radii for different water cloud types and aerosols, both of which are taken to be composed of spherical particles. Of the 11 aerosols components that can be included in RTTOV-10 (listed in Table 1.1), 10 have properties taken from the OPAC database and additionally volcanic ash has been supplemented. Different modes for the same species reflect different particle sizes with different mode radii. The user introduces a number density (cm^{-3}) for the appropriate component at the appropriate vertical layer/s. RTTOV-10 also contains 10 predefined climatological profiles for certain regimes, such as the desert or the Antarctic, which contain typical vertical mixtures of all 11 components for that region.

Water clouds can be defined as 5 different types, 2 stratus and 3 cumulus (listed in Table 1.2). From the range of sizes defined in the OPAC package a standard liquid water content LWC (gm^{-3}) and number concentration N (cm^{-3}) is calculated, and then a constant scaling factor S for each cloud type is defined from the relationship between them by:

$$S = \frac{LWC}{N} \tag{1.25}$$

Table 1.1: RTTOV aerosol components

Aerosol Component
Insoluble
Water-soluble
Soot
Sea salt (acc. mode)
Sea salt (coa. mode)
Mineral (nuc. mode)
Mineral (acc. mode)
Mineral (coa. mode)
Mineral-transported
Sulphate droplets
Volcanic ash

When a cloud liquid water content is introduced into a layer RTTOV calculates N by using the rearranged version of equation 1.25 along with the predetermined value of S, and from this value derives absorption, scattering and extinction optical depths via comparison with normalised versions stored inside the code.

Table 1.2: RTTOV liquid cloud types and scaling factors

Cloud Type	**S factor**
Stratus Maritime	266.67
Stratus Continental Clean	892.86
Cumulus Maritime	147.72
Cumulus Continental Clean	1538.46
Cumulus Continental Polluted	4333.33

A sixth cloud type is defined in the form of cirrus to deal with ice clouds. The large variability in ice crystal size, shape and location renders their treatment more complex so a composite database has been created inside RTTOV for 30 different ice cloud types with their associated size distributions that depend on the temperature and location of the cloud. The option currently exists in RTTOV-10 to specify the clouds as either hexagonal or aggregates (Figure 1.9). Hexagonal columns tend to form at the top of clouds and aggregates at the bottom where turbulent dynamics

tends to induce coalescence between ice crystals. The database of aggregates is taken from Baran and Francis (2004) and consists of 8 hexagonal columns attached to one another. For ice crystals, the interaction between radiation and the particles is highly dependent on crystal size, and no one solution covers all. A large combination of methods was used to generate the database of optical properties of ice crystals in RTTOV, for more detail see Saunders et al. (2010).

For each ice crystal size distribution a generalized effective diameter (D_{ge}) is defined, based on the ice water content (IWC) and/or temperature, from which extinction, scattering and absorption coefficients, and backscatter parameters are found. The parametrisation for calculating D_{ge} from IWC and/or the cloud temperature can be specified by the user by selecting 1 of 4 possible option based on the methods given in the publications listed in Table 1.3.

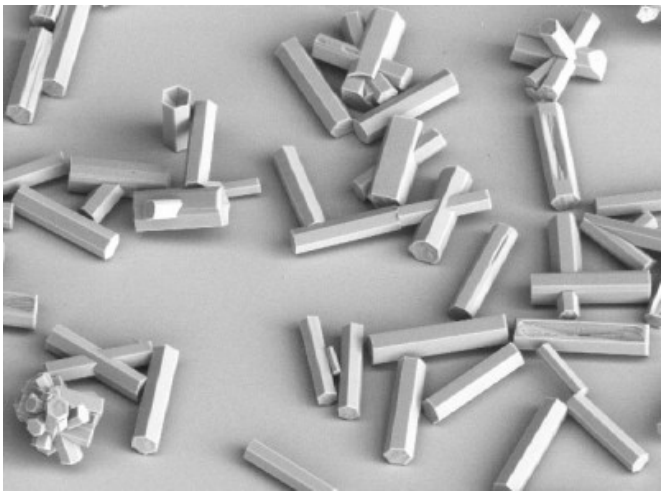

Figure 1.10: Impression of aggregate shaped ice crystals (bottom left corner) and column shaped hexagonal ice crystals.

Table 1.3: RTTOV parameterisation options for generating D_{ge}, and their associated dependencies

Parametrisation	**Dependency**
McFarquhar et al. (2003)	IWC
Boudala et al. (2002)	IWC and Temperature
Wyser and Yang (1998)	IWC and Temperature
Ou and Liou (1995)	Temperature

Additionally a new scheme was introduced in RTTOV-9 to better represent partial horizontal cloud cover. In it, a 'multi-stream method' is applied the radiative transfer equation (Amorati and Rizzi, 2002; Matricardi, 2005). This method divides a single profile into a number of horizontally homogeneous columns dependent on the number of cloudy atmospheric layers, the cloud fractions and the overlap assumption. The TOA radiance is the sum of each column's radiance weighted by its area. Like HadGEM2, RTTOV also uses a maximum-random overlap hypothesis for cloud cover (Räisänen, 1998). RTTOV-10 differs from RTTOV-9 in its ability to accept cloud water concentrations for multiple cloud types in a single layer, based on the assumption that the different types do not interact with each other. It does not, however, have the ability to reflect the relative fractions of different cloud types on each layer. In this case the total sum of all cloud fractions in the model gridbox is the only input allowed.

1.5 Aims of the thesis

This thesis aims to develop methods which allow the representation of the atmosphere in global climate models to be evaluated. The model selected as a prototype is the HadGEM2 model, but it is envisioned that the methods developed could apply to other climate models. A multi-spectral approach is used to focus on compensating errors obscured by traditional broadband analyses, and to isolate atmospheric components by virtue of their sensitivity to different wavelengths. The usefulness of such spectral radiance tests will be demonstrated by comparisons with equivalent broadband evaluations. This thesis deals with the forward model method of GCM evaluation to avoid the substantial errors associated with the inverse problem. The necessity for a fast radiative transfer code to facilitate the comparison with satellite radiances is not error free however, as its fast nature introduces various parametrisations along with their associated uncertainties. This thesis therefore is as much a test of the RTTOV satellite simulator as it is the climate model, and isolating individual biases and primary modes of sensitivity in both is important.

Given the well-known problems associated with the representation of GCM clouds it is expected that these will emerge as the most prominent bias between model and observations. As such, a broad approach is taken by comparing all-sky and clear-sky results at various wavelengths in the first instance, to highlight spectral differences. This project was incepted with the intention of exploiting the HIRS narrowband instrument in its all-sky format, as a development of work stemming from clear-sky analyses (Lindfors et al., 2011; MacKenzie et al., 2012), with the aim of seeing if this data is useful. As a result of this initial analysis it was decided that an examination of the full longwave spectrum was required with the aim of revealing biases in spectral regions uncovered by current satellite instruments, namely, the far infrared below 645 cm^{-1}. Hence, the final aim of this thesis is to assess the use of hyperspectral data, in firstly creating a spectrally extended radiance product, and secondly in evaluating the equivalent simulated in climate models. This is a more technical challenge due to the much higher resolution involved, but provides an incredibly strict test for both the climate and radiative transfer models.

1.6 Outline of the thesis

The remainder of this thesis is set out as follows. Chapter 2 compares observations from the 12 longwave channels of the High Resolution Infrared Radiation Sounder (HIRS) instrument on the MetOp-A satellite, with the equivalent GCM data simulated by RTTOV-10. Both all-sky and clear-sky comparisons are made and sensitivity tests relating to orbital sampling, clear-sky construction and parameter choices are performed. An equivalent broadband analysis using CERES and HIRS OLR data is carried out to compare with the narrowband results. Chapter 3 presents a new observational product using the hyperspectral IASI instrument and increasing the range of spectral resolution to cover the entire longwave region using a theoretical correlation method. The integrated product is verified against co-incident and composite CERES measurements. Chapter 4 combines the method used in Chapter 2 with the product created in Chapter 3 to perform a complete comparison of the simulated longwave spectrum at very high resolution. A separate broadband comparison using the IASI OLR product is facilitated by estimating the radiance-to-flux conversion factors. Chapter 5 presents the conclusions made from the whole study, along with its limitations and possible directions for future work.

Chapter 2

HIRS Model Evaluation

2.1 Introduction

The performance of HadGEM2 with respect to its cloud distribution is summarised in Chapter 1, Section 1.3.3.1. The focus of the present chapter is investigating these known cloud biases further, through decomposition of the longwave spectrum into discrete narrowbands. The High Resolution Infrared Radiation Sounder (HIRS) instrument provides the possibility of carrying out such a test with 12 narrow wavelength bands across the longwave infrared spectrum. Having flown onboard 16 satellites to date, the HIRS instruments form a continuous radiance record of near global coverage extending back to 1978, when the first incarnation flew aboard the Television Infrared Observation Satellite (TIROS-N). Originally intended for weather forecasting purposes, it has provided valuable insights into the fields of upper tropospheric water vapour (Allan et al., 2003; Soden et al., 2005), cirrus cloud retrievals (Wylie et al., 1994, 2005), and GCM evaluation (Chevallier et al., 2001; Chung et al., 2011; MacKenzie et al., 2012).

Due to the different overpass times of NOAA satellites, their drifting away from their designated orbits (see Figure 2 of Lee et al. (2007)), and the changes in spectral response functions that have occurred between instruments, efforts have also been concentrated on correcting and homogenising the record (Chen and Cao, 2012; Shi and Bates, 2011; Cao et al., 2009, 2005b; Bates et al., 1996). Such 'heritage'

instruments provided by NOAA, including HIRS, have been included on the first European Organization for the Exploitation of Meteorological Satellites (EUMETSAT) polar-orbiting satellite, MetOp-A launched in October 2006. This provides a unique opportunity to use HIRS data without the problem of orbital drift as the satellite is in a highly stable orbit (Righetti et al., 2007), and use of a single satellite eliminates the need for inter-satellite homogenisation. A comparison of operational HIRS radiances with the equivalent convoluted IASI measurements on the same satellite reveals average differences of no more than 0.3 K, which is within the accuracy requirement of HIRS operational calibration. This difference is attributed to the HIRS blackbody bias, spectral response function shifts and nonlinearity terms (Chen and Cao, 2012).

A weakness in any radiation study using passive satellite instruments is that the data in a wavelength band only provides information about the uppermost emitting atmospheric layer that it is sensitive to. Limited knowledge can be gleaned about the vertical profile of geophysical quantities below, hence the new generation of active sounding instruments such as CloudSat which were designed to fill this gap (Stephens et al., 2002). Although the design of the 12 longwave channels HIRS instrument is such that it samples radiation sensitive to three atmospheric constituents (H_2O, O_3 and CO_2) across a range of pressure levels, additional results obtained by comparing GCM temperature, humidity and cloud fields to the latest reanalysis data from the ERA Interim project, can aid interpretation (Dee et al., 2011). Reanalysis data is not equivalent to, but assimilates, observations in its forecast model and as such is more representative of reality that GCMs alone, thus can help in isolating prominent geophysical biases in the climate model. Being a model itself though, it has its own errors which must be taken into consideration.

The following GCM evaluation takes the form of a temporal and spatial comparison of all-sky brightness temperatures measured by MetOp-A/HIRS longwave channels and the equivalent simulated by HadGEM2, sampled to match the local time coverage of the satellite. The clear-sky equivalent is then constructed to isolate cloud effects. Exploring model choices that have to be made when setting up the comparison, we look at monthly mean output direct from the GCM and monthly composites constructed from instantaneous output. The threshold assumptions made in defining

model clear-sky data are also investigated. Next, the performance of HadGEM2 in the broadband OLR is tested. Finally we perform a simple sensitivity analysis of the cloud variables in the model, to reveal areas of weakness.

2.2 Data and Methodology

2.2.1 HadGEM2-A Climate Model Data

The atmosphere-only configuration of HadGEM2 version 6.6.3 is run for the time period covering 2009 (experiment xgtbda), forced by observed sea surface temperatures and sea ice extents taken from the Hadley Centre Sea Ice and Sea Surface Temperature dataset (HadISST) (Rayner et al., 2003). The horizontal resolution is 1.875 ° longitude by 1.25 ° latitude corresponding to a meridional size of about 140 km, and it has 38 vertical levels extending up to approximately 40 km above the surface.

The Smith cloud scheme in HadGEM2 is described in Section 1.3.4.1. The following 3-dimensional output for large-scale cloud fields are obtained: liquid condensate, ice condensate, liquid fraction, and ice fraction, as instantaneous fields at 15 hourly intervals and also as monthly means. The 2-dimensional cloud fraction produced by the model for each profile is also used in the determination of the clear-sky, which uses a maximum random overlap assumption (Räisänen, 1998). Additionally convective cloud condensate and fraction with the same temporal resolution are obtained. The parameterisation of convective cloud is described in Section 1.3.5.

In comparing broadband behaviour we obtain TOA measurements of all and clear-sky outgoing longwave radiation, along with incoming and outgoing shortwave radiation from our HadGEM2-A model run. The radiation code used by HadGEM2 is the Edwards-Slingo radiation scheme, which is a 'two-stream' scheme that solves for 6 wavebands in the shortwave, and 9 in the longwave (Edwards and Slingo, 1996).

2.2.2 ERA-Interim Reanalysis Data

The ECMWF Interim Reanalysis (ERA Interim) dataset covers the period from 1979 to the present and is the most recent ERA reanalysis available (Dee et al., 2011). The data incorporates observations from satellites, aircraft, sondes, balloons and in situ measurements, and the assimilation uses the ECMWF integrated Forecast System (IFS) model. It includes many advances with respect to ERA-40, including better horizontal resolution, improved model physics and the use of 4D-Var instead of 3D-Var (Simmons et al., 2007). ERA Interim fields of temperature, specific humidity and cloud fraction are obtained from the ECMWF database at 6-hourly time intervals for the period of 2009 at 15 of the 37 pressure levels available, with a horizontal resolution of 0.75 ° x 0.75 ° (spectral truncated T255 grid). Annual zonal pressure means are compared with the equivalent data from HadGEM2-A, whose hybrid height vertical co-ordinates are interpolated to the corresponding pressure levels. While temperature and cloud fraction biases are shown as absolute differences, specific humidity is given as a percentage bias (Δq) where:

$$\Delta q(\%) = 100 \times \frac{q_{HadGEM2} - q_{ERA}}{q_{ERA}} \tag{2.1}$$

This measure is chosen because the absorption of longwave radiation by water vapour is proportional to the logarithm of the water vapour amount, therefore the very low concentrations at lower pressures can be compared on the same scale with those at high pressures (Soden et al., 2005).

2.2.3 HIRS/4 Satellite Data

The 4th generation HIRS is a 20 channel passive infrared sensor with a 'stop and stare' cross-track scanner and 56 fields of view (FOV) in a single swath. It is carried by the MetOp-A satellite which operates in a sun-synchronous orbit with an ascending node local time of 21:31. HIRS/4 comprises 19 infrared channels: 12 thermal infrared (6.7μm to 15μm) defined as longwave, 7 near infrared (3.7μm to 4.6μm) defined as shortwave, and 1 visible channel (0.69μm). Table 2.1 gives the details of each channel. Of the 12 longwave channels, 1-7 are sensitive to CO_2 and are designed for measuring temperatures from near surface to stratosphere, 1 and 2 are stratospheric and the peaks of 3-7's weighting functions descend through the

Table 2.1: Details of MetOp-A HIRS/4 longwave channels. Approximate weighting functions (WF) are those of a U.S. Standard Atmosphere. CO_2 channels have a diminishing sensitivity to the ν_2 band with increasing channel. All channels are sensitive to temperature.

Channel Number	Central Wavelength (μm)	WF Peak (hPa)	WF Lower Bound (hPa)	WF Upper Bound (hPa)	Sensitivity
1	14.95	40	<0.1	250	CO_2 ν_2 (centre)
2	14.71	60	<1	300	CO_2 ν_2
3	14.49	100	<1	600	CO_2 ν_2
4	14.22	300	1	1000	CO_2 ν_2
5	13.97	500	1	surface	CO_2 ν_2
6	13.64	700	<5	surface	CO_2 ν_2
7	13.35	850	<5	surface	CO_2 ν_2
8	11.11	surface	350	surface	window
9	9.71	surface/30	<1	surface	O_3
10	12.47	surface	200	surface	H_2O ν_2 (weak) split window
11	7.33	500	40	1000	H_2O ν_2
12	6.52	300	20	600	H_2O ν_2 (near centre)

troposphere. 8 senses the surface, 9 is ozone, 10, 11 and 12 are lower, middle and upper tropospheric water vapour respectively. Channel 10 is a split window channel, partially absorbing water vapour but relatively transparent, often used alongside the highly transparent window channel 8 for water vapour retrievals. In terms of this study its behaviour is seen to closely resemble that of channel 8.

HIRS/4 differs from HIRS/3 in its increased footprint resolution (10km rather than 20km diameter at nadir), but the spectral characteristics are unchanged. The shape of the weighting functions for HIRS/3 are shown in Figure 2 of Li et al. (2000). Additional channel characteristics can be found in the NOAA KLM user's guide (NOAA, 2006). We focus on results for 4 of the HIRS/4 channels, chosen in such a way to summarise the features observed across all 12 longwave channels. These are channels 2,4,8 and 12. The study uses un-gridded all-sky brightness temperatures processed using the ATOVS and AVHRR Processing Package (Klaes et al., 2005) for the period March 2007 to December 2009, which is gridded onto a 1.875° longitude by 1.25° latitude grid (HadGEM2-A model resolution). A clear-sky HIRS product developed by NOAA (Shi and Bates, 2011) is matched pixel-for-pixel with the all-sky

data to identify clear-sky brightness temperatures which are then similarly gridded. Only the nadir-looking FOV 29 is used. All annual means are for 2009 because of a 2 month gap due to data quality in the clear-sky data in January and February 2008.

2.2.4 HIRS OLR Data

The HIRS OLR product was developed in the late 1980's by Ellingson et al. (1989a) and now provides a continuous record of data spanning more than 3 decades (Lee et al., 2007). It uses a multispectral regression technique to estimate OLR from radiances obtained from 4 of the HIRS channels: 3, 7, 10 and 12. A change of channels 10's spectral response function in the HIRS instruments developed after HIRS/2 means that the algorithm now uses channels 3, 10, 11 and 12. The operational HIRS OLR Climate Data Record (CDR) dataset contains monthly mean OLR fluxes at the TOA gridded to 2.5° x 2.5° resolution, and is a blend of the fluxes estimated from individual satellites to achieve better temporal integral accuracy. The CDR product has been validated against the CERES EBAF measurements over the 2000-2011 period, with a globally averaged difference of 0.6 Wm^{-2} (HIRS greater), and spatial differences of more than 2 Wm^{-2} found only in subtropical dry zones, equatorial strong convection regions and cold/dry/high elevations, possibly because HIRS OLR is thought to be overly sensitive to surface emission (Lee and Ellingson, 2013). We validate these calculations for the period of interest, 2009, in section 2.3.3. For temporal and spatial consistency with the HIRS narrowband analysis the ungridded HIRS OLR estimates are retrieved from MetOp-A only (Hai-Tien Lee, personal communication, 2013), gridded to 1.25° x 1.875° resolution in line with the model and compared with HadGEM2-A OLR data subsampled to MetOp-A local times. As the data has not been cloud cleared a corresponding clear sky analysis is not possible, hence CERES-EBAF data is utilised for this purpose.

2.2.5 CERES-EBAF Satellite Data

TOA observations of all and clear-sky OLR to compliment HIRS OLR data are obtained from the Clouds and the Earth's Radiant Energy System (CERES) (Wielicki et al., 1996), onboard polar orbiting satellites Terra and Aqua. CERES measures fil-

tered radiances in the reflected shortwave (0.3μm to 5μm), total (0.3μm to 100μm), and window (8μm to 12μm) regions. Longwave radiances are determined from the difference between the total and shortwave channel radiances. The Energy Balanced and Filled (EBAF) product (Loeb et al., 2009), adjusts the shortwave and longwave fluxes such that the global mean net TOA flux is equal to the estimated heat storage in the Earth system. It also supplements CERES measurements with those from geostationary satellites to improve diurnal coverage. The monthly CERES-EBAF product is also regridded, from 1 ° x 1 ° resolution to 1.25 ° x 1.875 ° to match the resolution of HadGEM2-A data.

2.2.6 RTTOV-10 Radiative Transfer Model

The Radiative Transfer model for TOVS version 10.2 (RTTOV-10) (Saunders et al., 2011) is run in forward atmospheric mode to simulate HIRS brightness temperatures from climate model output. Details of the code are given in Chapter 1, Section 1.4.4.

Cloud diagnostics from the climate model are sorted for each grid box for input into RTTOV as described below and shown as a process diagram in Figure 2.1. Liquid water contents (LWC) and ice water contents (IWC) are obtained by performing a unit transformation on all cloud condensates, multiplying mass fractions (kg/kg) by the layer atmospheric density to give liquid water content, convective water content and ice water content in g/m^3. "Empty clouds", which are anomalous clouds with a fraction but no water content (and vice versa), are identified and removed. Mixed phase cloud, the fractional overlap between liquid and ice cloud, is included in both the ice and liquid cloud fractions. It is relatively rare because HadGEM2 assumes it can only exist when the sum of the liquid cloud fraction (LCF) and the ice cloud fraction (ICF) is greater than 1. When mixed phase cloud is present the mixed phase fraction (MCF) is diagnosed from the difference between the sum of LCF and ICF, and the bulk cloud fraction (BCF). Then both the liquid and ice fractions are reduced by half of the mixed phase fraction as follows:

$$MCF = (LCF + ICF) - BCF \tag{2.2}$$

$$LCF' = LCF - \frac{MCF}{2} \tag{2.3}$$

$$ICF' = ICF - \frac{MCF}{2} \tag{2.4}$$

where LCF′ and ICF′ are the resulting pure liquid and ice stratiform fractions, which are then used to scale the corresponding hydrometeor concentration from grid box means to in-cloud values (convective cloud fraction is already given as an in-cloud value) as follows:

$$LWC_{incloud} = \frac{LWC_{gridboxmean}}{LCF'} \tag{2.5}$$

$$IWC_{incloud} = \frac{IWC_{gridboxmean}}{ICF'} \tag{2.6}$$

Stratiform liquid and ice cloud fraction are then scaled by the fraction of the grid box that is not convective to make room for the convective cloud fraction (CCF) as they are calculated separately in the climate model (see earlier description of the HadGEM2 convective scheme in section 1.2.3.1):

$$LCF_{final} = (1 - CCF) \times LCF_{incloud} \tag{2.7}$$

$$ICF_{final} = (1 - CCF) \times ICF_{incloud} \tag{2.8}$$

In previous versions of RTTOV the concentration of only one cloud type could be specified per grid box, requiring a choice to be made. However RTTOV-10 now accepts individual cloud water contents from up to 6 different cloud types. We filter concentrations into 5 of these: stratus continental, stratus maritime, cumulus maritime, cumulus continental clean and cirrus. Deep convective clouds contain both liquid and ice portions so a threshold temperature of 253.15 K (-20 °C) is applied to grid boxes containing convective cloud water. If the local temperature is below this then the cloud water is treated as cirrus, if not it is treated as liquid, and then partitioned into cumulus continental clean or cumulus maritime. This decision was made based on the convective cloud restrictions of the radiation code within the unified model: where water cloud is not permitted below -40 °C, nor ice cloud above 0 °C, hence our partition is the halfway point between these two. Stratiform liquid water content is partitioned into stratus continental or stratus maritime, and ice water content is designated as cirrus. Finally a single cloud fraction is passed to RTTOV which is simply the total of liquid, ice and convective cloud fractions. A monthly CO_2 concentration is calculated using linear interpolation from yearly values, the interaction of aerosols with longwave radiation has not been considered in this analysis.

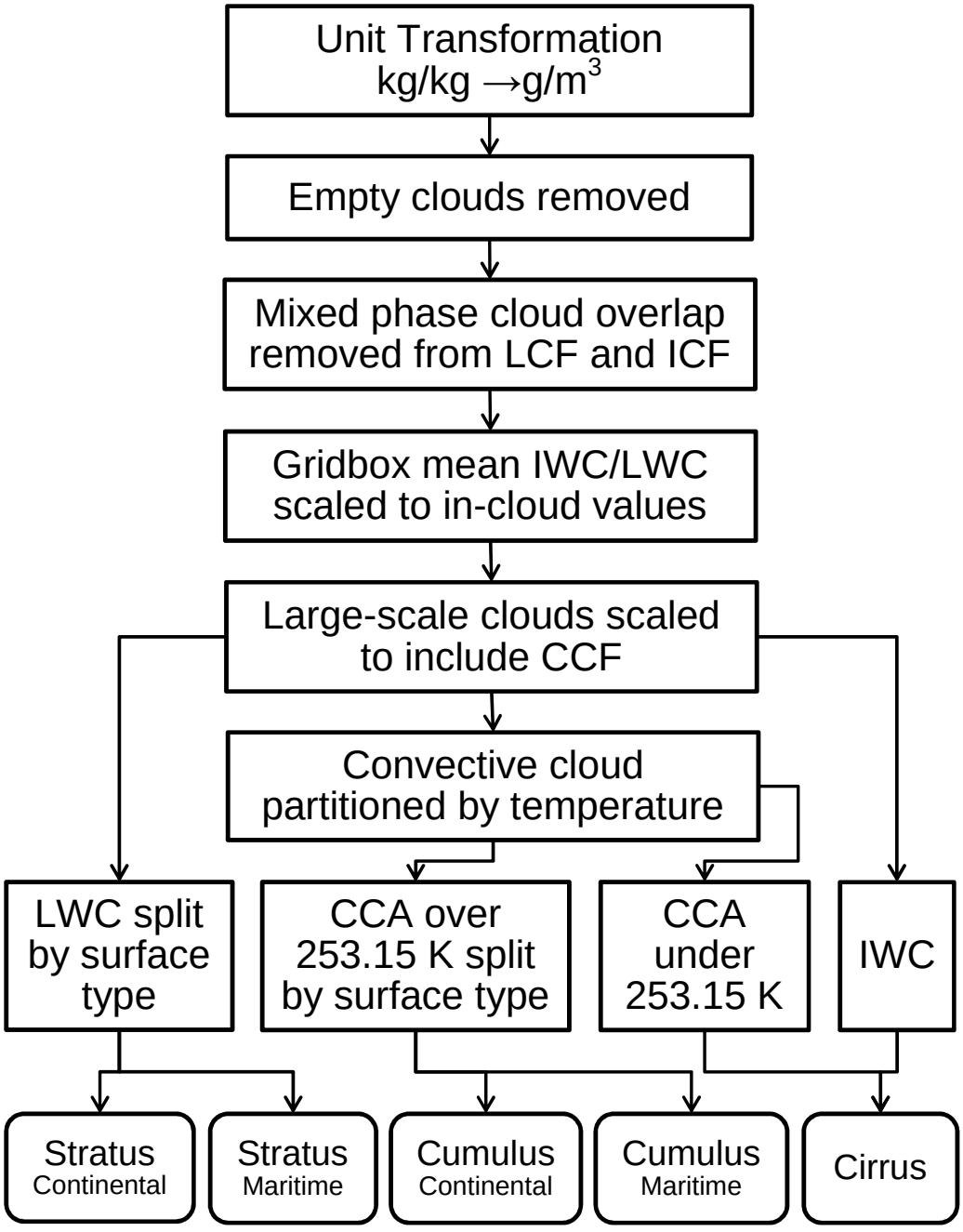

Figure 2.1: Process diagram that filters clouds from climate model output to RTTOV-10 input.

2.2.7 Model Sampling

2.2.7.1 Instantaneous vs. Monthly

Two different frequencies of climate model output are analysed in the study. The first are instantaneous values at 15 hour timesteps, each of which is processed through the radiation code and then averaged to give a monthly mean - referred to as 'instantaneous means' in the text. This frequency was chosen because over the course of 5 days 8 measurements are taken that sample the diurnal cycle at a resolution of 3 hours, but avoids the computational expense of sampling every 3 hours. The climate model has a 360-day year resulting in 48 sets of instantaneous data per month. The monthly mean values that the model calculates from the internal model timesteps every half an hour are also obtained and passed through the radiative transfer code - referred to simply as 'monthly means' in the text. All spatial and sensitivity studies are performed using instantaneous means.

2.2.7.2 Mimicking satellite trajectory

Climate model output is globally synchronous. Thus, for every timestep a global grid of values is produced at one UTC time. Local solar time is offset from this time by a factor dependent on longitude. MetOp-A has a local equatorial crossing time (LECT) of 21.30 for the ascending node and 09.30 for the descending node. As it is in a sun-synchronous orbit it will pass over any given sub-satellite point at the same local time. For the 65 °S to 65 °N latitude band all local-times sampled by the satellite will be within a 3 hour window centred on the LECT. Note that this assumes the satellite has no orbital drift, which is a good assumption for MetOp-A. The remaining local times are sampled when the satellite passes over higher latitude bands.

MetOp-A's LECT means that the midday peak of the diurnal cycle, which is particularly strong in the lower tropospheric channels 8 and 10 (MacKenzie et al., 2012), will be absent in the satellite data so the model must be sampled accordingly to avoid diurnal aliasing. The effect of this is investigated by calculating the global annual mean diurnal cycle of brightness temperatures simulated by the model for each channel for all local times, alongside those tracked by the satellite (Figure 2.2). The

mean of the MetOp-A subset of values within the 2 local time windows approaches the mean of all local-times to within 0.1 K for land, ocean and the global mean. This result is in line with previous findings (Allan et al., 2003), and while suggesting an analysis without satellite sampling would not yield significant errors in the global mean, there is a possibility that spatially errors could be seen over land, where the diurnal variability is larger in the lower tropospheric channels, and globally due to the diurnal cycle of clouds (Wylie, 2008).

Model data is sub-sampled to retain only those local times within the 3 hour bands shaded in Figure 2.2 for the 65 °S to 65 °N latitudes, and in the polar regions a 3 hour window around each satellite local overpass time at any given latitude is applied. This reduces the amount of model data to a quarter of its original size, so instead of 48 values all gridboxes will contain 12 over a month, 6 in the local morning and 6 in the local evening. The corresponding number of MetOp-A satellite measurements in each grid box varies depending on latitude (Figure 2.3). Whereas the gridboxes between 65 °S and 65 °N contain around 15 footprints each, polar gridboxes often contain double this amount, because even though the zonal width of a grid box reduces to 4.5 km every single satellite orbit passes close to the north and the south pole. This sampling frequency of a satellite simulated model with a 15 hour timestep is thus comparable with observations between 65 °S and 65 °N, and the reduced model sampling over the poles is unlikely to introduce errors because the polar diurnal cycle has a low amplitude compared to the annual cycle. It should be noted however that the inclusion of all data within a 3 hour window may have an effect on those channels, such as 8 and 10, which have a strong diurnal cycle. As can be estimated from Figure 2.2c brightness temperatures in channel 8 vary by approximately 5 K over land between 08:00 and 11:00, whereas over ocean the same quantity varies less than 1 K. This variation will not be present in observations so could introduce aliasing, however, constraining the time sampling window further would result in an insufficient number of model gridpoints for the comparison to be consistent. Satellite local-time sampling is not possible with the monthly averaged model output as each point is an average of all times over the month, an argument for why instantaneous data should be used for evaluating climate models with satellite data.

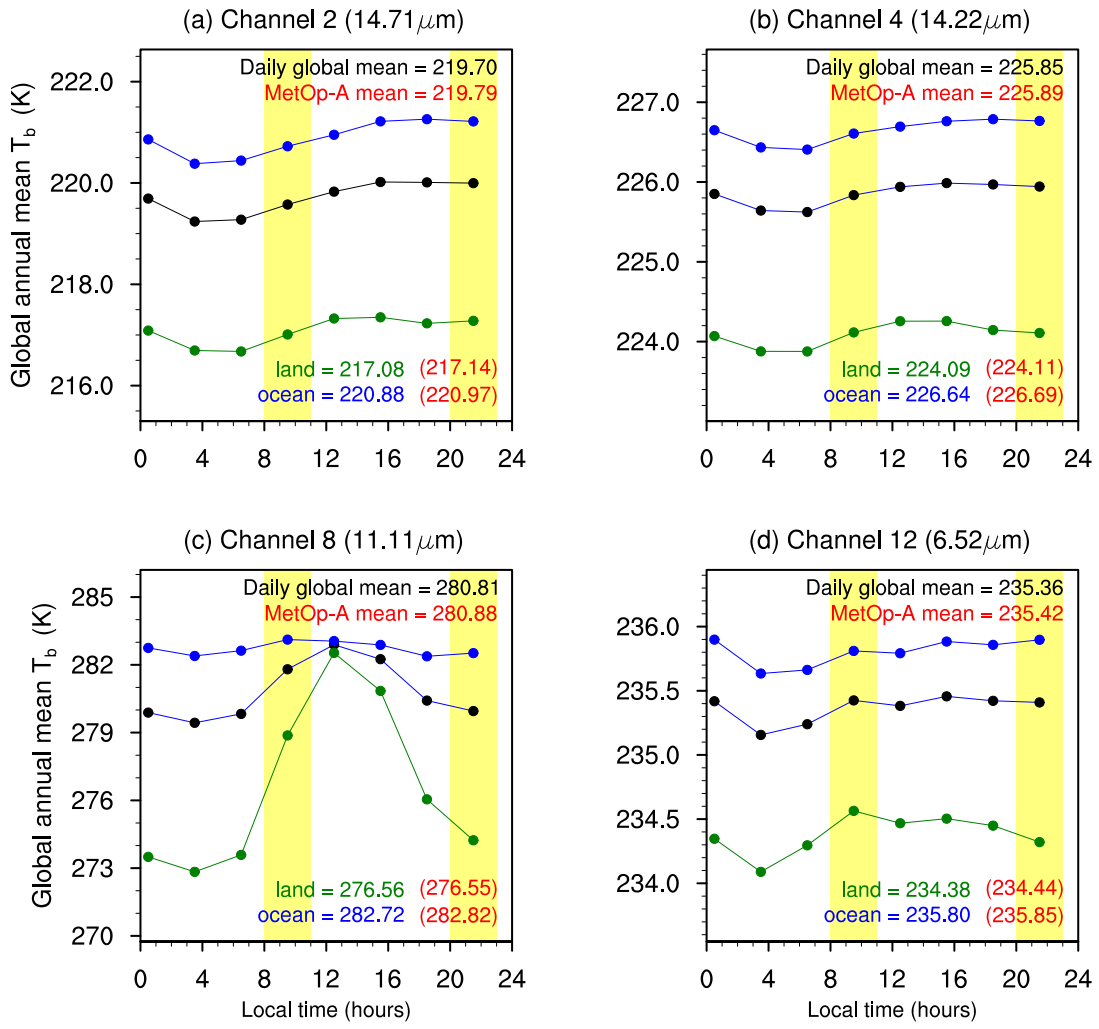

Figure 2.2: The global annual mean diurnal cycle of all-sky brightness temperatures in satellite simulated HIRS channels (a) 2, (b) 4, (c) 8, and (d) 12 for 2009. Each point is the 3 hour mean. Blue lines are ocean, green are land and black are global. Areas shaded yellow encompass the limited range of local times that MetOp-A samples in the 65 °S and 65 °N latitude band, for the ascending node (20:00-23:00) and the descending node (8:00-11:00). Numerical values show the annual global mean brightness temperatures for MetOp-A-like sampling in red, and model data at all local times in black with their corresponding ocean and land components. All units are in K.

2.2.7.3 Clear sky thresholds

The clear-sky HIRS data used was cloud cleared by Shi and Bates (2011) following the method detailed by Jackson et al. (2003), which combines spatial and temporal variations in the brightness temperature and applies thresholds to these variations to detect clouds. Typically, in any one day, we identify 20% - 23% of the all-sky pixels in a single FOV as clear, removing up to 80% of the data due to cloud contamination. A satellite pixel is designated as cloudy for the whole atmospheric column, regardless of whether the cloud is detected in the upper or the lower troposphere. This means that in a channel sensitive to a particular band of pressures the fraction of the globe marked as clear-sky will be underestimated. For example, when the clouds are stratified by height, clear fractions as high as 67% (high), 82% (middle) and 76% (low) are found (Wylie et al., 2005). This undersampling is less of an issue when creating gridded monthly composites however, as it is likely that over the course of a month at least one pixel in every gridbox will be identified as clear.

The corresponding climate model clear-sky distribution is difficult to identify as the horizontal resolution of the model is low relative to a HIRS footprint. Therefore specifying whether a gridbox is clear or cloudy requires a degree of approximation as each one will likely contain regions of both, as summarised by the 2-dimensional cloud fraction. Using all-sky profiles and then assuming no clouds would introduce a moist bias into the clear-sky brightness temperatures, as the water vapour input will still be reflective of a sky that includes clouds because the clouds are positively correlated with water vapour, particularly in humid tropical regions. This is the opposite of the problem seen in clear-sky satellite measurements, where it is possible to only select pixels of pure clear-sky, creating a world with unrealistically low levels of humidity (John et al., 2011). Compounding both these water vapour biases would be particularly detrimental to HIRS channels 10 - 12. Similarly, errors arise from using only grid boxes where the cloud fraction is zero as this results in very sparse sampling. To find a middle ground for these unavoidable disparities we follow the traditional method of imposing a cloud fraction threshold to the GCM data, below which the gridbox is considered clear. For example a threshold of less than 10% cloud fraction means that brightness temperatures from only those pixels with a total column cloud fraction of less than 10% are included in the clear-sky global

mean. The aim is to balance sampling of a sufficient number of grid boxes, with retention of clear-sky atmospheric conditions (specifically water vapour).

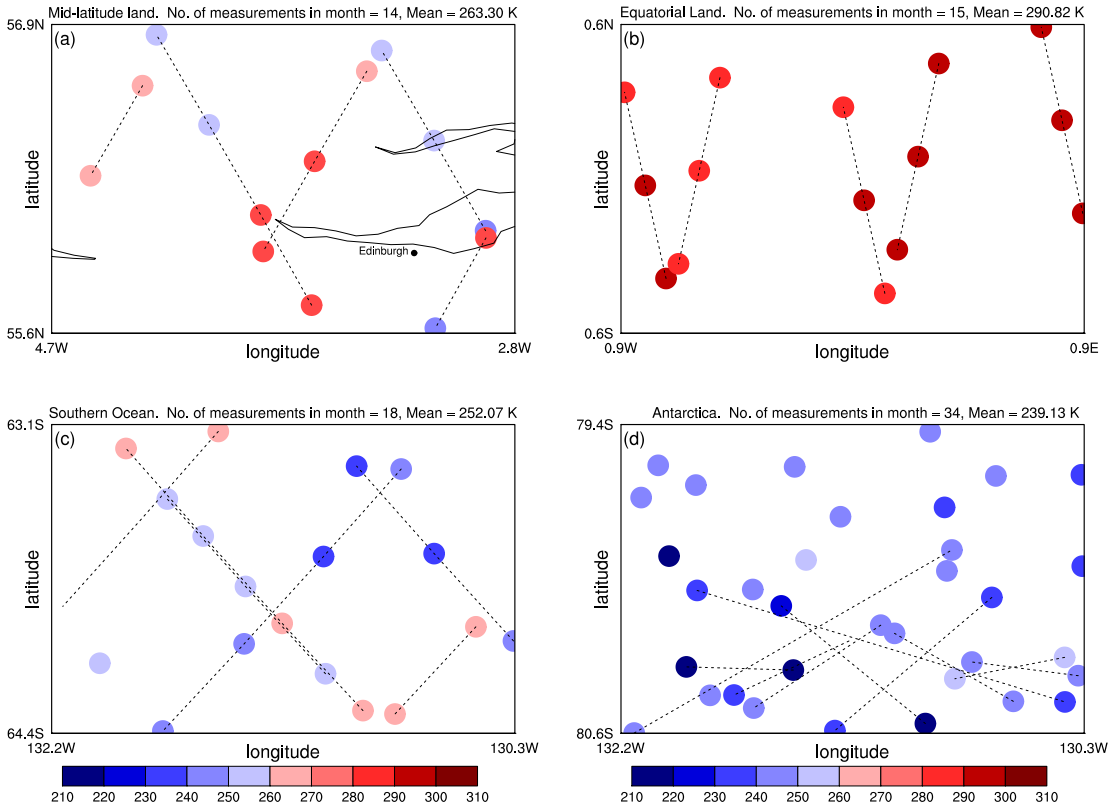

Figure 2.3: HadGEM2-A size gridboxes containing all-sky channel 8 brightness temperatures for all MetOp-A HIRS footprints (FOV 29) in July 2009 for (a) Midlatitude land, (b) Equatorial land, (c) Southern Ocean and (d) Antarctica. Colours refer to the brightness temperature given in the key and dashed lines give an indication of satellite trajectory. All units are in K.

Previous studies sampling HIRS clear-sky brightness temperatures have used fixed thresholds of 30% (Iacono et al., 2003), 40% threshold (MacKenzie et al., 2012) and 50% (Allan et al., 2003). To investigate the effect of making this threshold choice we create gridded clear-sky composites with thresholds of 40%, 30%, 20% and 10% and compare each one with the clear-sky satellite measurements.

2.2.7.4 Sensitivity tests

To explore the sensitivity of the radiative transfer code to different cloud related model inputs we perform some simple tests by uniformly altering one input to RTTOV-10 at a time on all model levels. We alter only one aspect of the existing cloud distribution and do not change the timing or how frequently the clouds appear, which would require changing thresholds within the parametrisation scheme. Each test and its description is listed in Table 2.2. These are designed only to give an idea of how much RTTOV-10 responds to each field and are not representative of reality.

Additionally the sensitivity of the radiances to the choice of ice parametrisation is examined. The 4 options for converting ice water content and/or temperature to effective diameter are listed in Chapter 1, Table 1.3 and are all tested with both hexagonal and aggregate crystals shapes, giving 8 combinations. Consistency for the remainder of the simulations within this thesis is retained by using a single combination based on the findings of Vidot et al. (2011), which concluded that specifying the crystal shape as aggregates and using the Wyser method (Wyser and Yang, 1998) to convert ice water content to effective diameter gave results that best approached observations.

Table 2.2: Description of each sensitivity test. All tests apart from the monthly mean are performed on all 576 instantaneous model output files over the 360 day year and then averaged to give the 2009 annual mean.

Test	**Description**
CONTROL	15 hourly model output. Clouds processed as described in section 2.2.6
Monthly mean model output	As control but monthly mean files produced directly from the climate model are used as inputs to RTTOV-10.
CLEARSKY <40% cloud fraction	The same cloud type partitioning as the control run. Only those gridboxes where the 2 dimensional cloud fraction was less than 40% are retained.
CLEARSKY <30% cloud fraction	The same cloud type partitioning as the control run. Only those gridboxes where the 2 dimensional cloud fraction was less than 30% are retained.
CLEARSKY <20% cloud fraction	The same cloud type partitioning as the control run. Only those gridboxes where the 2 dimensional cloud fraction was less than 20% are retained.
CLEARSKY <10% cloud fraction	The same cloud type partitioning as the control run. Only those gridboxes where the 2 dimensional cloud fraction was less than 10% are retained.
Clouds shifted X level/s up	The same cloud type partitioning as the control run initially. All cloud properties from each level are then used as inputs to the level X level/s above. This leaves X level/s at the bottom of the atmosphere cloud free and X cloud level/s are lost at the top.
Cold convective cloud not marked as cirrus	As control but convective cloud at temperatures lower than 253.15K is not partitioned as cirrus.
Large-scale only - no convective cloud	As control but convective cloud is not introduced, thus large-scale cloud is not scaled down to include it.
Ice fraction increased by 100%	As control but when ice cloud exists the fraction is doubled (including low temperature convective clouds already partitioned as cirrus). Total cloud fraction is capped at 1.
Ice water content increased by 100%	As control but when ice cloud exists the water content is doubled.
Liquid fraction increased by 100%	As control but when liquid (large-scale) cloud exists the fraction is doubled. Total cloud fraction is capped at 1.
Liquid water content increased by 100%	As control but when liquid cloud (large-scale) exists the water content is doubled. All other cloud properties remain the same.
Convective fraction increased by 100%	As control but when convective cloud exists (after low temperature clouds have been partitioned as cirrus) the fraction is doubled. Total cloud fraction is capped at 1.
Convective water content increased by 2100%	As control but when liquid cloud (large-scale) exists the water content is multiplied by 22. This is designed to approximate the liquid water content from a typical cumulus cloud, see model description of the convective water threshold in Chapter 1 Section 1.3.5

2.3 Results

2.3.1 Global mean comparison by month

On a global mean basis, biases between model and observations for channels 2,4,8 and 12 (Figure 2.4) have different magnitudes depending on the channel and method of sampling, but do not seem to show any year-to-year differences over the 3 years compared. Stratospheric channel 2 (Figure 2.4a) exhibits an average positive bias of 1 K with little difference between all and clear-sky (for the instantaneous means). Being a region that rarely contains clouds (with the exception of polar stratospheric clouds, which are part of HadGEM2's cloud scheme), this is expected and therefore all disparities between model and observations must be clear-sky in origin, such as errors in the temperature or water vapour profiles. Channel 4 (Figure 2.4b) does better with all-sky and clear-sky biases remaining stable at 0.5 K and -0.5 K respectively.

The largest biases are seen in all-sky comparisons of window channel 8 (Figure 2.4c), with model brightness temperatures approximately 6 K warmer than observations for instantaneous means, and around 7 K for monthly means. We interpret this as too much radiation being emitted from lower levels of the troposphere where the average temperature is warmer. The magnitude of this bias is not reflected in the clear-sky equivalent, which varies between -0.5 K and 1.5 K with a more pronounced annual cycle. Splitting the bias into its land and ocean components reveals the majority of the variability is coming from the land where the peak reaches 3 K in September and the trough reduces to -0.5 K in February, yet the ocean bias remains more stable around 1 K all year round. These clear-sky land errors are attributed to uncertainty in the land surface temperatures, as unlike SSTs, these are not prescribed.

Channel 12 (Figure 2.4d) shows the most sensitivity to the method of all-sky and clear-sky sampling. For the former there is an average difference of 2 K between instantaneous mean and monthly mean all-sky data, produced by the non-linearity of the radiative transfer equation with respect to water vapour. Channel 4 peaks at approximately the same weighting function (300 hPa), but does not show the same behaviour because it is insensitive to water vapour. Both of these channels are only affected by very high clouds, but channel 4 seems to suggest that they have

little effect on the method of calculating the monthly average, probably due to the relatively low amount of clouds at this level.

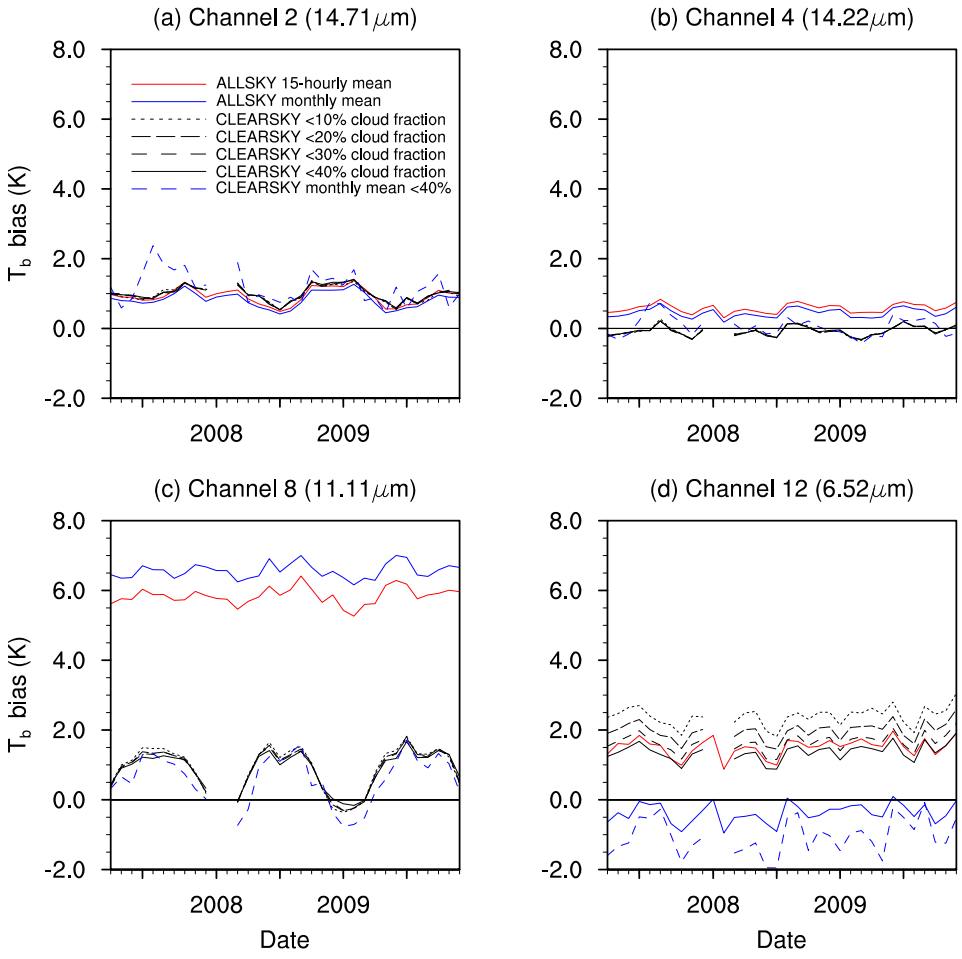

Figure 2.4: Variation of monthly global mean brightness temperature bias (model - satellite) with time for HIRS channels (a) 2, (b) 4, (c) 8 and (d) 12. Allsky: The mean of 15 hourly instantaneous data (a total of 48 files per month) is shown in solid red and the monthly mean data calculated within the climate model is shown in solid blue. Clear-sky: Different cloud fraction thresholds calculated from instantaneous 15 hourly data are shown in black, the dashed blue line is the 40% cloud fraction clear-sky bias constructed from the model monthly mean data. All latitudes seen by the satellite are included (81.25 °S - 81.25 °N)

Channel 8 shows a 1 K bias difference between methods and has a weighting function that peaks at the surface, thus is affected by all clouds in the atmospheric column, of which there are more near the surface. As the satellite measures radiance from instantaneous atmospheric fields on a continual basis, which are then used to calculate the monthly mean, the model instantaneous means are closer in construction to the satellite product. The significant differences between all-sky instantaneous and monthly mean radiances in low cloud studies and, even more importantly, upper tropospheric water vapour studies indicates that the former method should preferentially be used, however for wavelengths less sensitive to these components, such as channel 2 near the centre of the CO_2 ν_2 band, this is not as important because very similar values are obtained.

Erratic differences of the order of 0.5 K to 1 K, between instantaneous mean and monthly mean clear-sky biases are present in all channels, and are even greater (up to 4 K, depending on the instantaneous clear-sky threshold) in channel 12. Further investigation reveals this is due to inadequate coverage by clear-sky monthly mean data, explained as follows. In any 1 month up to 25% of the model data is identified as clear, however, the conditional inclusion of any monthly pixel based on: a) there being a corresponding clear satellite pixel at the same location to avoid spatial biases, and b) there being a minimum of 9 pixels present at that location in the year to avoid seasonal biases, brings the number of gridboxes remaining to below 10%. But with the instantaneous process before these steps are taken a 48 member composite of clear-sky data has been created for each month leaving far more data in the monthly average, and nearly 60% remains in the annual mean.

For clear-sky instantaneous means there is surprisingly little difference between the biases resulting from the different model cloud fraction thresholds used for most of the channels. This is reassuring given the fact that the threshold choices are relatively adhoc, and thus it is concluded that 40% is preferable to use as more gridboxes are included in the clear-sky composite. In channel 12, however, there is a spread exceeding 1 K between the 10% and 40% thresholds, with the latter being closer to observations. This separation can be attributed to the positive correlation between water vapour and cloud cover, where a higher threshold such as 40% will have an elevated water vapour concentration compared with a lower threshold like

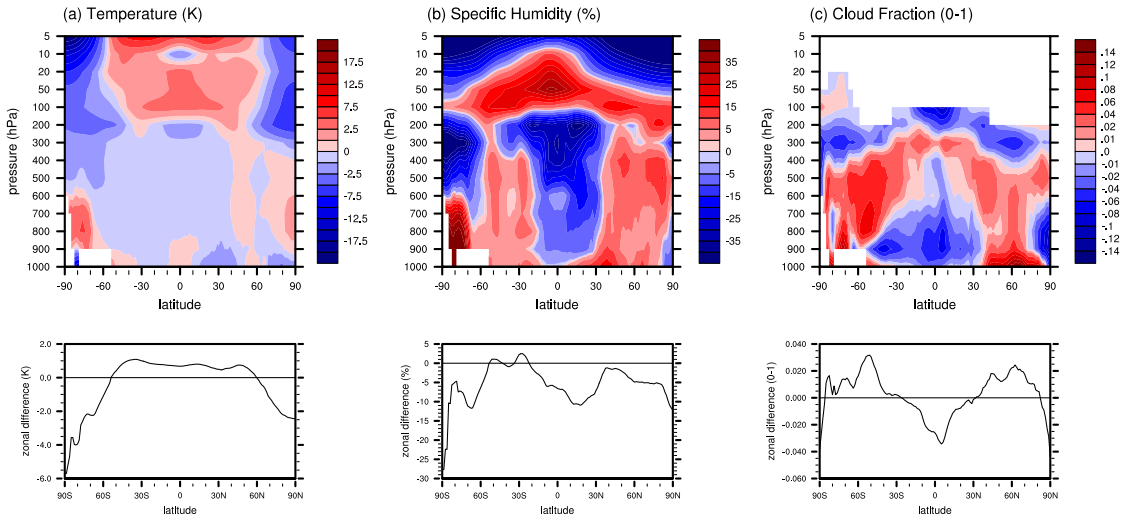

Figure 2.5: 2009 Zonal-pressure differences between HadGEM2-A and ERA-Interim geophysical quantities (a) absolute temperature (K), (b) percentage difference in specific humidity (% of kg/kg - described in section 2.2.2) and, (c) absolute cloud fraction (0-1)

10%, so radiation with wavelengths sensitive to water vapour will be emitted from a higher/colder region of the atmosphere above the heightened humidity distribution.

It is inconsistent, therefore, that the higher threshold is performing better than the lower, because the former has a humidity distribution less reflective of clear-sky. This is possibly due to the quality of the simulated water vapour in the model. A recent study of humidity biases in GCMs identified HadGEM1 as one of only 3 models with a consistent dry bias throughout the troposphere, meaning radiation will emanate from an atmospheric level too low (John and Soden, 2007). In general most models simulate a dry bias in the boundary layer and a larger moist bias in the free troposphere. There was no focus on improving the representation of humidity between HadGEM1 and HadGEM2 (Collins et al., 2008), thus it is reasonable to suggest that this bias still exists in HadGEM2. Indeed, the percentage difference in specific humidity between ERA-Interim and HadGEM2-A in Figure 2.5b shows a strong negative/dry bias across much of the troposphere in the 30 °S - 30 °N region, which is much stronger than the midlatitude positive/moist biases also present. The elevated water vapour concentration in the 40% clear-sky threshold could be compensating

somewhat for this existing error, to a greater extent than lower thresholds, cancelling errors and bringing the clear-sky bias closer to 0 K. This heightened sensitivity of channel 12 to model clear-sky thresholds has strong implications for estimates of longwave cloud forcing, as previously highlighted by Sohn et al. (2010), on top of sampling only meteorological conditions unusually free of cloud. All conclusions drawn from humidity studies that use clear-sky data only must be viewed with caution in light of this result.

2.3.2 Spatial distribution of annual bias

De-constructing these global biases spatially reveals that in the window channel positive/warm all-sky tropospheric biases are dominant in regions associated with deep convective activity (Figure 2.6c), regions which, by definition, are absent in the corresponding clear-sky analysis (Figure 2.7c). The annual global mean is 274.72 K as measured by HIRS, and 280.57 K as calculated by the model. Zonally, the bias is strongest in the equatorial region (the annually averaged ITCZ), widening over land to encompass all of South America north of Argentina, all non-arid central-west regions of Africa, and in the Indo-Pacific warm pool (20 °S - 20 °N, 60 °E - 180 °E) including the land regions of India, Bangladesh, Sri Lanka and Indonesia. This pattern corresponds closely to regions identified with maximum cirrus occurrence resulting from anvils on top of deep convective plumes associated with the ITCZ and seasonal monsoonal circulations, and additionally from a layer of thin cirrus (see Figure 1 of Sassen et al. (2008)).

There are negative/cold biases over the Tibetan Plateau and the east coastal zone of Africa, and to a lesser extent in the South American low-level jet region and the Arabian Peninsula. This pattern also shows up in the clear-sky equivalent and therefore must be associated with surface temperatures. The Tibetan Plateau in particular is a difficult region to simulate, with an average elevation exceeding 4.5 km and containing the worlds third largest store of ice. It has a distinct regional climate that climate models have difficulty capturing (Zhou and Yu, 2006).

There are generally smaller positive biases over the ocean, particularly around the

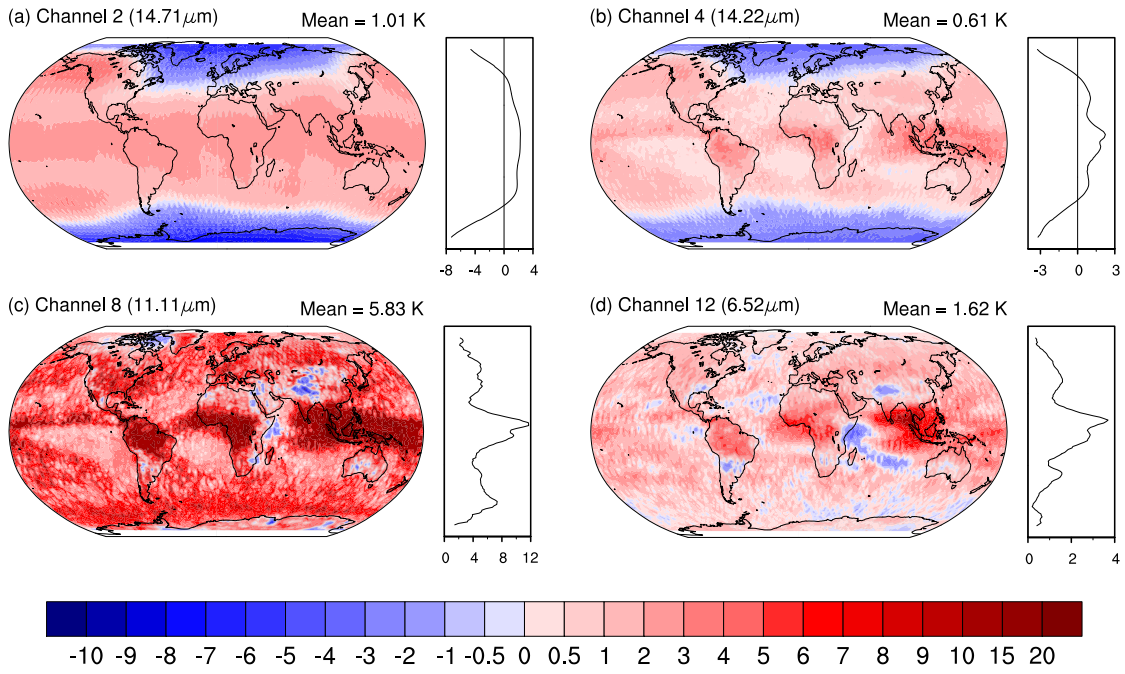

Figure 2.6: Maps of all-sky annual mean brightness temperature biases for 2009 (model - satellite) with zonal mean plot for HIRS channels: (a) 2, (b) 4, (c) 8, and (d) 12. Only pixels where no months are missing were included in the annual mean. Units are in K.

equatorial cold tongue, the southern Atlantic and the Indian ocean region west of Australia. These subsidence regions west of the subtropical continents are dominated by widespread low stratus cloud which is not distinguished in the infrared because cloud top temperatures are similar to the sea surface temperatures which are prescribed in the model. Strong biases observed in other regions must therefore originate from the mid to upper troposphere, and because the window channel is sensitive to no other atmospheric constituents apart from clouds (and a small contribution from the water vapour continuum), we can deduce that the reason for these biases are clouds which are present in the satellite's FOV but are absent in the climate model at higher levels. This conclusion is corroborated by comparing model mean vertical cloud fractions with the equivalent quantity in ERA-Interim (Figure 2.5c). The uppermost level of cloud fractions is up to 12% too low in the model, across all latitudes. Even though in mid latitude regions the mean of the column averaged cloud fraction is overestimated, the satellite instrument only senses radiation emitted from

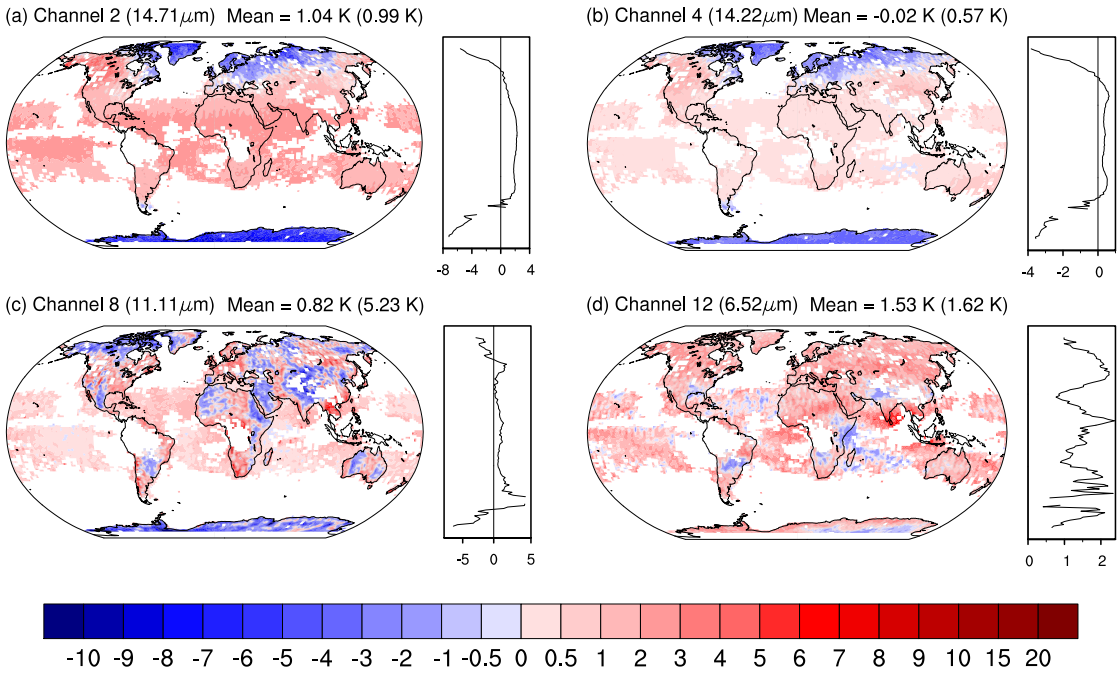

Figure 2.7: Same as Figure 2.6 but for the clear-sky. The model clear-sky cloud fraction threshold is 40%. Only pixels with no more than 3 months missing are included in the annual mean. Areas shaded white correspond to missing data. The figure in brackets is the all-sky bias masked by the areas where the clear-sky is not missing. Units are in K.

the top cloud layer. One possible contribution to this apparent lack of clouds could be the mis-timing of the daily convective maximum, as discussed in Chapter 1, Section 1.3.5, which peaks too early in the model (at noon rather than 18:00 to 21:00), so that with the reduced local times sampled by MetOp-A the peak is included in observations but missed by the model.

The spatial signature of the deep convective bias can also be seen in channel 4 (Figure 2.6b), which will only be affected by the very tops of deep convective clouds. Channel 12 has a weighting function that peaks at a similar level and the same pattern of positive bias is observed in Figure 2.6d. However, accepting HadGEM2 has a dry upper troposphere as discussed in section 2.3.1, a general lack of water vapour could be contributing to this bias (meaning radiation will be emitted from too low a level in the atmosphere), as well as missing water vapour that is associ-

ated with the presence of clouds. Additionally HadGEM2 appears to have a warm tropopause bias of up to 3 K around 100 hPa in the equatorial regions (Figure 2.5a), which will cause a positive bias in the highest cloud top emission, by virtue of this temperature difference alone. Quantification of this bias is estimated in Section 2.3.3.

Stratospheric channel 2 shows very different behaviour (Figure 2.6a and Figure 2.7a). There is a low warm bias (less than 2 K) for the majority of the 65 °S to 65 °N band, and a strong cold bias at latitudes greater than 60 °S/N that peaks at the poles. This channel also displays the most spatial variability throughout the year (not shown) with a strong northern hemisphere cold bias in the boreal winter months: November, December, January and February, alongside warm southern hemispheric biases, and the same pattern with the polarity flipped in the months of May, June, July and August. When averaged annually the result is the dual pole pattern that is observed and the slight seasonal cycle observed in Figure 2.4a arises because the boreal summer pattern has lower northern hemispheric warm biases allowing the cold bias to dominate.

The reason why the model is in excess of 5 K colder at the stratospheric winter pole is not immediately clear, but two possibilities are the way the stratosphere is treated by the radiative transfer model, and the climate model. Channel 2 has a weighting function that broadly peaks at 60 hPa but contains contributions from between 300 hPa and below 1 hPa. The 51 reference pressure levels that RTTOV-10 uses to interpolate input profiles onto extends up to 0.005 hPa, and in a change to RTTOV-9, does not impose a hidden level here with the same variable values as the top-most input level, removing an isothermal layer between the climate model top and the top of the radiative transfer model. Inspection of the HadGEM2-A data reveals minimum pressures of about 0.9 hPa at the winter poles, which is covered by RTTOV-10, and means the vertical extent of the channel's weighting function falls within the climate model levels, however even though the absence of any input data between 0.9 and 0.005 hPa is likely to affect the simulated radiation to an extent, it is unlikely it would be responsible for the strength of the biases seen in Figures 2.6a and 2.7a.

The 38 level configuration of HadGEM2-A that is used is considered a low-top model, and has a course resolution in the stratosphere. Recent studies have shown that the low model lid at about 39 km does not simulate stratospheric circulation properly, in comparison with the high-top 60 level configuration, which extends up to about 84 km and has more than double the stratospheric resolution (Hardiman et al., 2012). In general, it is found that large cold biases in the high latitude middle stratosphere (10 to 30 hPa) are an anomalous feature of low-top models, which are absent in their high-top counterparts, and are thought to be due to problems with the dynamics of planetary waves in the stratosphere (Charlton-Perez et al., 2013; Cordero et al., 2006). These cold polar biases in the stratosphere below 200 hPa are evident when compared with the ERA-Interim temperature fields (Figure 2.5a). As 14.71μm is near the centre of the CO_2 ν_2 band which is extremely sensitive to temperature changes (see Figure 2b of Huang et al. (2007b)), temperature errors will show up strongly in these channels. It is therefore concluded that the inability of the low-top version of the model to reproduce the Brewer Dobson circulation in the stratosphere accurately is responsible for these polar biases, but further clarification of this point is beyond the scope of this study. Even though these biases are large, they are localised and balanced in the global mean by a widespread region of positive bias in the extra-polar areas, hence will not show up in the estimate of the OLR global mean.

Containing contributions from both the stratosphere and the troposphere, channel 4 (Figure 2.6b) seems to represent a transition between this high latitude cold bias behaviour and the equatorial warm bias behaviour seen in the tropospheric channels, as both patterns can be seen, but at lower magnitudes. These two 'modes' of bias compensate to give a low global mean of 0.61 K, whereas in the clear-sky equivalent (Figure 2.7b), a higher proportion of the equatorial warm mode is absent, bringing the global mean down to -0.02 K .

The source of the seasonal cycle seen in the clear-sky biases in Figure 2.4c is due to large areas of cool bias over land in the boreal winter months balancing warm biases over sea, whereas in the boreal summer land biases become largely warm, with the peak of this behaviour occurring in July. This is likely to be due to the diurnal aliasing of warmer temperatures occurring at local times up to 11:00 in the model which are absent in the 09:30-only sampling by the satellite instrument. Figure 2.7c

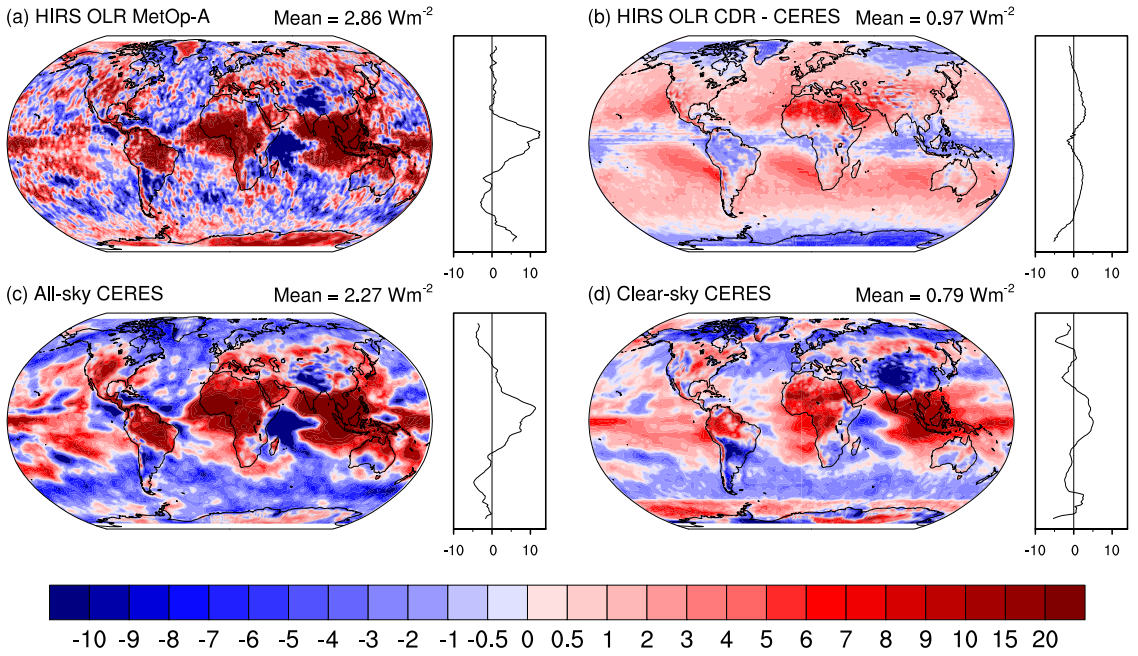

Figure 2.8: (a) All-sky OLR differences between HadGEM2-A and the OLR estimated from HIRS channels on MetOp-A. The model retains only those local times sampled by the satellite as described in section 2.2.7.2. (b) OLR difference between the HIRS OLR CDR product (a blend of measurements from the various satellites carrying HIRS and thus including all local times) and the CERES EBAF product. (c) All-sky and, (d) clear-sky OLR bias between HadGEM2-A simulations and CERES EBAF observations. Zonal means are shown to the right of maps. All data is the 2009 annual mean and only latitudes 81.25 °S - 81.25 °N are included. Units are Wm^{-2}.

displays what appears to be the global mean of this aliasing behaviour in the form of 'striping' of positive and negative biases over the land regions, with widths consistent with a 3 hour time window. It is possible that the mis-timing of convection also contributes to this pattern also because the warm surface temperatures associated with convection will be absent in model gridpoints sampled between 20:00 to 23:00. The ocean biases are low overall which is to be expected from an atmospheric only run in line with prescribed SSTs.

Table 2.3: 2009 broadband TOA global mean radiative fluxes from HadGEM2-A and HIRS OLR for all local times, and Metop-A subsampled times (column in italics). CERES EBAF data is also shown. Only latitudes 81.25 °S - 81.25 °N are included and net is taken as being in the downwards direction. Units are Wm^{-2}.

Component	HadGEM2-A	CERES	*HadGEM2-A (MetOp-A)*	HIRS OLR (CDR)	HIRS OLR (MetOp-A)
Incoming solar	343.1	341.8	*384.5*	-	-
All-sky					
Outgoing longwave	242.3	240.1	*242.5*	241.0	239.7
Outgoing shortwave	98.8	99.5	*120.3*	-	-
Net	**1.9**	**2.2**	***21.7***	**-**	**-**
Clear-sky					
Outgoing longwave	267.2	266.4	*267.0*	-	-
Outgoing shortwave	54.1	52.1	*61.2*	-	-
Net	**21.8**	**23.3**	***56.4***	**-**	**-**

2.3.3 Broadband OLR

Figure 2.8a shows all-sky broadband biases reproduced in a manner temporally and spatially consistent with the previous narrowband comparison, as the OLR data is constructed solely from MetOp-A HIRS radiances and the model data is subsampled to match the satellites orbit. The absolute flux values in Table 2.3 show that while the complete set of HadGEM2-A data and the MetOp-A sampled data are similar to within 0.2 Wm^{-2} for the longwave, differences of up to 40 Wm^{-2} are found for the shortwave, due to the larger variability in the diurnal cycle of incoming and reflected solar radiation (for illustration of this point see Figure 10 of Ramanathan (1987)). This highlights the need for satellite like sampling in these types of GCM evaluation studies. The HIRS OLR algorithm is evaluated against CERES data in Figure 2.8b for all local times and is shown to have a less than 1 Wm^{-2} difference in the global mean, with zonal means rarely exceeding 2 Wm^{-2}. Hence it is expected that using CERES instead of the HIRS OLR dataset would produce similar results, which can be seen by comparing Figures 2.8a and 2.8c. The former is more noisy due to the fact only one satellite is included. The difference between these experiments is 0.59 Wm^{-2} which gives us confidence that conclusions can be drawn from the clear-sky CERES experiment in Figure 2.8d.

Using either all-sky result, it is clear that the global mean OLR in the all-sky is overestimated in the model, but the bias is relatively low at 2.86 or 2.27 Wm^{-2}

(Figure 2.8a and c). However, the zonal means reveal that this is due to a fortuitous cancellation between a wide band of positive errors in the tropical latitudes between 25 °N/S and negative errors at higher latitudes particularly across the Southern Ocean. As discussed in Section 2.3.2 the warm tropopause bias in HadGEM2 temperatures which reaches 3 K will also contribute to OLR biases from high clouds. Using the Stefan-Boltzmann equation (Black-body irradiance, $F = \sigma T^4$, where σ is the Stefan-Boltzmann constant and T is the temperature) at average temperatures at this level (around 196 K), a 3 K bias has a flux effect of around 5 Wm^{-2}, which is approximately half of the bias in these latitudes.

A similar spatial pattern is seen in clear-sky OLR biases (Figure 2.8d), but a reduced positive bias in the tropics leads to enhanced compensation overall and the global mean appears better at 0.79 Wm^{-2}. It is possible that part of this positive pattern of bias is due to deficiencies in the cloud screening mechanisms in both the CERES product and the climate model. Another possibility is the lack of treatment of aerosols in the longwave component of the Edward-Slingo broadband radiation code, which could lead to an overestimation of OLR over regions of high mineral dust such as the Sahara. It cannot be clearly identified whether the corresponding absence of aerosol treatment in the specific configuration of RTTOV-10 used produces a similar clear-sky positive bias in channels that are sensitive to dust, because the diurnal aliasing from the 3 hour model time sampling appears to dominate the pattern of biases (Figure 2.7c), however, it is likely that this effect would be a contributing factor to the bias over Northern Africa.

To obtain an idea of how well these biases compare with the bands isolated by the HIRS sensor we use the Stefan-Boltzmann equation to convert broadband flux to the effective temperature of the Earth. Effective temperature differs from brightness temperature in that the former has no dependence on the direction of propagation (measured in solid angle) of the received radiation. The two are not equivalent and are only compared here to give an indication of the magnitude of possible differences. Effective temperature biases of the order of 0.6 K for all-sky and 0.2 K for clear-sky are estimated, an order of magnitude less than those in the HIRS channel 8. This is surprising as the the window region (10.5μm - 12.5μm) contributes more radiance per wavelength to the total OLR than all other wavelengths in the spectral range

covered by the HIRS longwave channels by a factor of 1.25 to 1.5 (see Figure 3 of Harries et al. (2008) for an example of this).

The dominance of the window region in the mid infrared is the reason it was originally the only waveband used to estimate the total OLR via a regression model using window measurements from the scanning radiometer onboard NOAA-1 to NOAA-5 (Gruber, 1977; Gruber and Winston, 1978). There are clear uncertainties in using only one spectral region to estimate the total OLR, however the subsequent development of the HIRS OLR climate dataset which uses multiple regression on four wavebands still attributes more than 50% of its weighting to channel 10 (12.47μm), which, in the absence of clouds is very sensitive to the near-surface (Lee et al., 2007). We conclude that the strong positive bias observed in the window region in Figure 2.6c would alone have a greater effect on the OLR than observed and the tolerable errors in Figure 2.8a and 2.8c reveal that other spectral regions must be providing compensatory negative biases.

Inspection of the whole OLR radiance spectrum reveals a contribution of equal, or sometimes greater magnitude (depending on the latitude and season) than the window region in the far infrared band (FIR), which we define as wavelengths between 15 - 400 μm (25 - 667 cm^{-1}). In the clear-sky the FIR is modulated by water vapour absorption and emission in the pure rotation band, The effect of a cloud on the longwave spectrum is to give the FIR more weight than in the clear-sky case, as by Wien's Law ($\lambda_{\max} = 2898/\text{Temperature}$, where λ is wavelength) the peak emission at typical cloud top temperatures is strongly dominated by FIR wavelengths. Up to 45% of the all-sky OLR from the Earth is made up of these wavelengths (Harries et al., 2008).

Previous studies with a line-by-line model have shown that within a tropical cirrus cloud, net absorption of radiation occurs in the window region and net emission occurs in the FIR, with little change to other wavelengths, including the water vapour ν_2 band which actually displays a slight absorption (Maestri and Rizzi, 2003). Though both the pure rotational and ν_2 bands are primarily sensitive to water vapour, they show very different contributions to the OLR, particularly in the presence of clouds.

This is emphasised by the relatively small difference (0.09 K) between the all and clear-sky biases in channel 12 (Figures 2.6d and 2.7d) revealing that clouds contribute little to the errors in this band, in comparison with the 5.01 K difference seen in channel 8 (Figures 2.6c and 2.7c). We have shown that absorption (removal of radiance/brightness temperature) is lacking in the model all-sky window region, suggesting an overall cloud deficit at top levels. It therefore corresponds by energy balance considerations (for example see Figure 1a of Maestri and Rizzi (2003)) that emission in the FIR could be lacking, leading to an underestimation of radiance/brightness temperature at these wavelengths. Therefore even though channel 12, which is sensitive to the vibrational-rotational bands of water vapour shows a 1.62 K positive all-sky bias it is possible that the FIR could display a negative bias, which could be responsible for the widespread negative regions in Figures 2.8a and 2.8c. Alternatively, the errors in these regions could originate from other parts of the spectrum outside of the 12 bands sampled by HIRS, which includes the lower intensity part of the window region from 7.33 - 9.71 μm, and the remaining part of the water vapour ν_2 region with wavelengths below 6.52 μm.

Exploring biases in the FIR requires satellite observations that isolate this waveband, but unfortunately the region has been little observed. The only such instrument to have sampled a portion of the FIR in isolation is the Infrared Interferometric Spectrometer (IRIS) that flew onboard the Nimbus 4 satellite between April 1970 and January 1971 and observed just the 400 - 600 cm^{-1} (16.7 - 25 μm) portion (Harries et al., 2001). A newly-developed instrument as part of the Far-Infrared Spectroscopy of the Troposphere (FIRST) project has been tested by NASA using balloon flights but is yet to be part of a satellites payload (Mlynczak et al., 2006). However, recent studies by Huang et al. (2013, 2010) and Chen et al. (2013) have estimated FIR radiances using correlations between far and mid infrared wavelengths for different scene types. This method may allow evaluation of the FIR in the absence of direct measurements and is the subject of Chapter 3.

2.3.4 Sensitivity tests

Figure 2.9a displays the range of annual mean biases obtained across all 12 longwave channels for the all and the clear-sky. It should be noted that while the level of peak

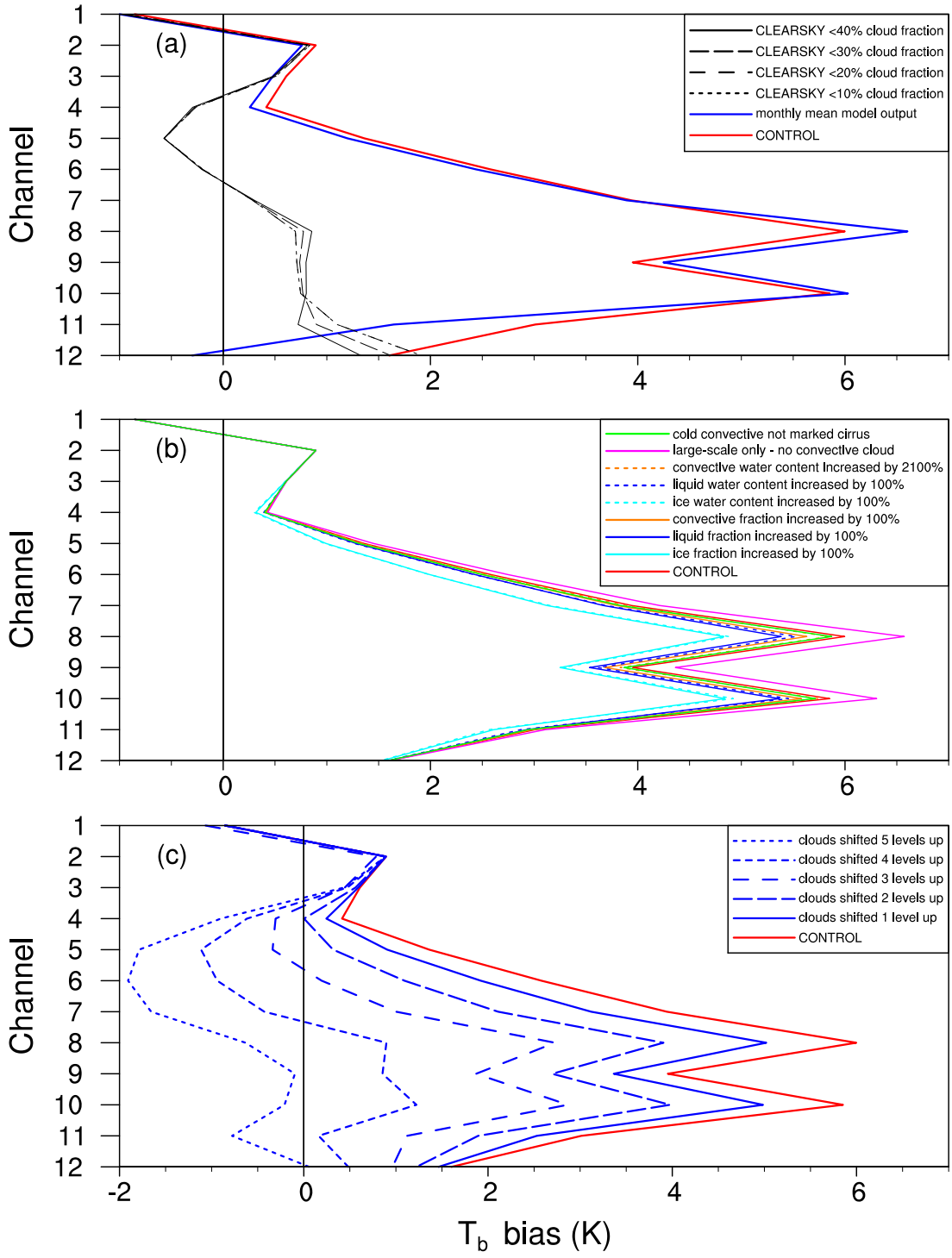

Figure 2.9: Annual global brightness temperature bias (model - satellite) for 2009 for all-sky instantaneous means compared with: (a) monthly means, clear sky biases also shown, (b) tests based on perturbing model cloud parameters and (c) tests based on shifting model cloud levels. All HIRS longwave channels are shown.

emission for channels 1 to 8 can be interpreted as decreasing from the stratosphere to the surface, channel 9 has a broad emission throughout the atmosphere, and channels 10 to 12 increase in height (see Table 2.1 for weighting functions). The following subsections describe the effects of perturbing cloud properties from the control state.

2.3.4.1 Increasing cloud properties

Altering cloud fractions and concentrations provides a test of the macro and microphysical properties associated with the existing cloud distribution within the model, otherwise known as the cloud amount when present. Here we only increase cloud properties where they already exist, which therefore cannot highlight whole regions of cloud absence. It is seen that no change of cloud properties alters the bias significantly (Figure 2.9b). Doubling the fraction of cirrus clouds has the largest effect, particularly in the window region (channels 8 and 10) where the bias reduction is in excess of 1 K with respect to the control. Further investigation reveals a higher annual mean fraction of ice clouds than either liquid or convective in the original model overall (Figure 2.10), possibly attributable to the inclusion of snow in its ice cloud output (in contrast to the absence of rain in its water clouds). As RTTOV only accepts a total cloud fraction on each level it is not able to weight the cloud types present according to their individual fraction, therefore when cirrus is doubled the greater initial fraction results in a greater final fraction, possibly explaining why changes to ice cloud has the greatest sensitivity. Additionally, as was identified in section 2.3.2, the pattern of prominent positive bias in tropical deep convective regions reveals a lack of longwave absorption at high levels, often corresponding to the locations of ice anvil cloud tops. It is therefore possible that the increase of cirrus clouds goes some way to compensate for their absence in the model.

Increasing the hydrometeor concentration in the clouds has less of an effect than increasing the fraction for every type shown, indicating that the clouds that exist are already at, or near, saturation. The effect of removing convective clouds increases the bias by a maximum of 0.5 K as seen in channel 8. As described in section 2.2.1, the diagnostic scheme in HadGEM2-A requires the large-scale cloud fraction be scaled down to include convective cloud, and thus the total fraction does not change significantly when they are included, unless the convective cloud fraction

is much larger than the large-scale fraction. As shown in Figure 2.10c the latter is not likely, particularly as large convective anvils are cold enough to be partitioned as cirrus (which is partly why Figure 2.10b has more cloud at high levels). Extra cloud concentration is always added when convective clouds are present however, so the main effect they have is to increase the overall water concentration in equatorial convective regions, which appears to have a minimal effect. Limited though these convective water content values are by a precipitation threshold of 0.08 g/m^3, multiplying the concentrations by 22 to approach values within real convective clouds (1.76 g/m^3) also has little effect.

2.3.4.2 Shifting cloud properties vertically

Shifting model cloud properties vertically upwards before input into RTTOV provides a rudimentary tool to see where vertical regions of cloud deficiency lie. Raising cloud top heights in the troposphere reduces the simulated brightness temperature because the infrared radiation is now being emitted from a cooler level, and as the tropospheric brightness temperatures have been shown to be largely overestimated in the climate model this brings the bias down significantly in all tropospheric channels, see Figure 2.9c. These tests are the only ones we perform where clouds are added to regions where the model might produce none, and of all the sensitivity tests performed this one has by far the greatest effect on the radiation bias. For example, in channel 8 raising the clouds by 4 levels reduces the bias to an amount commensurate with clear-sky values. In channel 4 an elevation of 2 levels minimises the RMS error, 5 levels is needed to do the same in channel 12 and due to the lack of clouds in the stratosphere, a negligible effect is seen with any vertical movement in channel 2.

The spatial pattern of biases produced by each channel when cloud properties are raised to the level where the global error is minimised is shown in Figure 2.11. By comparing channel 8 with the equivalent plot in Figure 2.6c it can be seen that the global mean bias is lower due to cancellation of errors, positive biases in deep convective regions are reduced and negative biases in regions with low positive values originally have been created. This fits with the zonal estimate of model cloud biases produced with ERA Interim data in Figure 2.5c. The introduction of negative biases

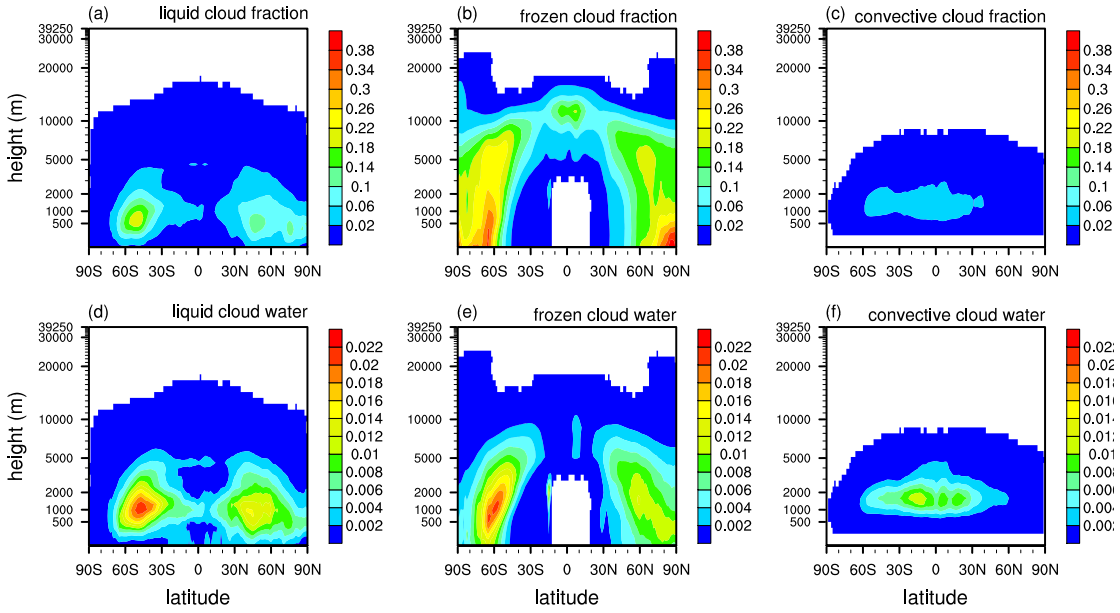

Figure 2.10: 2009 annual zonal mean cloud properties on model levels, for liquid, frozen and convective cloud types. (a), (b) and (c) are cloud fractions (0-1%); (d), (e) and (f) are cloud water contents (g/m^3). Data has been cloud partitioned following the method described in the RTTOV-10 methodology in section 2.2.6

could result from the upward shift of overestimated cloud from the broad layer under the top layer of underestimated cloud. It is important to note that ERA Interim clouds are themselves calculated as a parametrisation, and as such are not as reliable as observations. A known quality issue that affects the ERA Interim cloud data is an underestimation of low cloud cover under certain conditions, however as radiation is emitted from the highest cloud level in any vertical column this does not significantly affect our interpretation. Similar cancellations can be seen in channels 4 and 12 (Figure 2.11b and d), the former only requiring a 2 level rise as it has lower annual global mean biases to begin with, and the latter requiring a 5 level rise but only due to its low sensitivity to the vertical movement of clouds, thus only small improvements occur with each perturbation. This is because channel 12 is more responsive to water vapour which is not altered. It is clear that a blanket shift of clouds vertically does not resolve the problem of under absorption of long wave radiation in the model, the apparent better agreement in the global mean being due to introduction of further compensatory biases. Biases are more the result of general errors with the spatial and fractional occurrence of clouds - problems

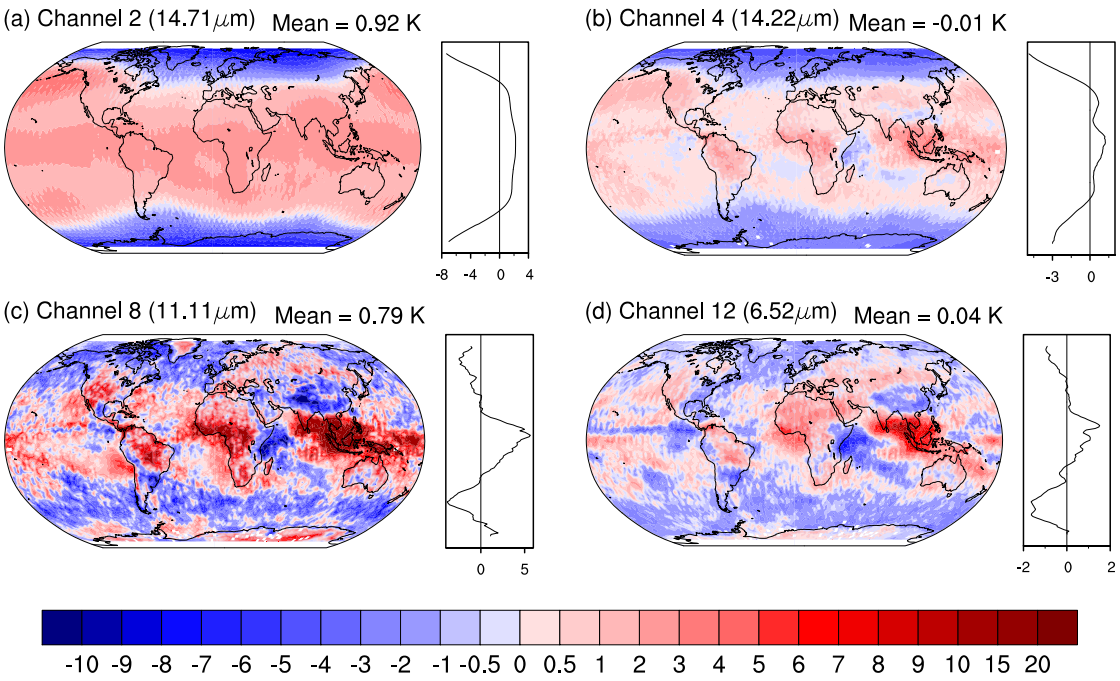

Figure 2.11: As Figure 6 but with clouds raised the number of levels that minimises the error in each channel which is: (a) 0, (b) 2, (c) 4 and, (d) 5. Units are in K.

which are related to the parametrisation scheme, rather than because they are occurring at too low a level, a result that agrees with previous findings (Li et al., 2013).

2.3.4.3 RTTOV ice parameterisations

Figure 2.12 shows the range of biases obtained using all possible combinations of ice cloud parameterisations provided in RTTOV-10. The maximum difference between schemes is 2.5 K in channel 10 (split-window), which is between the Wyser and Yang (1998) method and aggregate ice crystals and the Boudala et al. (2002) method with hexagonal crystals. Both crystal shapes for the Wyser and Yang (1998) and the McFarquhar et al. (2003) method cluster around the same values, whereas results for the Boudala et al. (2002) and the Ou and Liou (1995) methods are more spread out. The 40% reduction in window channel biases brought about by selecting the parameterisation that exhibits the lowest values is still not sufficient to reduce them to below 3 K.

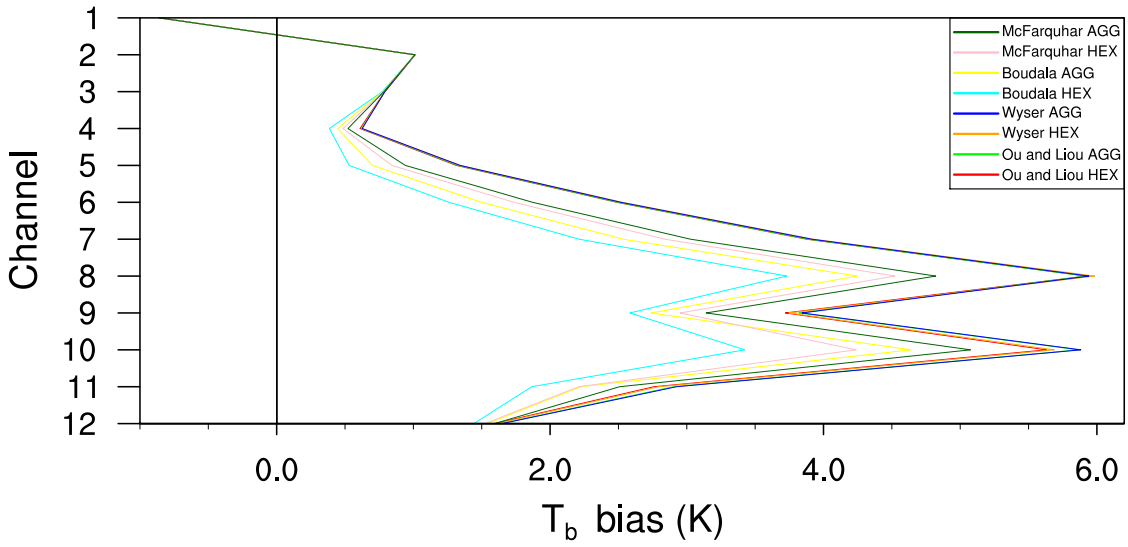

Figure 2.12: Annual global brightness temperature biases (model - satellite) for all ice cloud parametrisations available in RTTOV-10. Data is for the whole of 2009.

2.4 Conclusions and Discussion

Brightness temperatures from longwave bands observed by the HIRS instrument are used to evaluate those simulated by HadGEM2-A for the all-sky, alongside a broadband comparison. The same experiment is conducted with the clear-sky. The RTTOV-10 radiative transfer code with multi-level input for 5 different cloud types simulates the satellite measurements. The key findings are:

- Simulated all-sky brightness temperatures are too high in tropospheric channels, particularly in the window region. The strongest biases dominate in the equatorial land regions and the Indo-Pacific warm pool where deep convective clouds are present. These differences are considerably larger than the uncertainty in MetOp-A HIRS brightness temperature measurements.
- Clear-sky biases are lower than all-sky, by a factor of up to 6 in the window channels, even when compared with all-sky biases that are masked by the equivalent clear-sky regions. Spatial compensation contributes somewhat to these low biases, however.

- Global mean biases in the CO_2 ν_2 upper tropospheric/lower stratospheric channels appear better, however strong cold biases centred at both poles arising from the poor representation of the stratospheric Brewer Dobson circulation in the low-top HadGEM2-A model compensate for warm biases in the remaining regions.

- Clear-sky biases produced using four different cloud fraction thresholds between 10% and 40% are very similar, suggesting a choice of 40% is robust and preferable as a greater amount of data is sampled. Constructing the clear-sky from monthly mean output leaves too little data to give meaningful results and should be avoided.

- An exception to the previous point is the 6.3 μm water vapour ν_2 band, which has a strong sensitivity to the choice of clear-sky threshold due to the positive correlation between water vapour and cloud cover. We hypothesise that unavoidable moist water vapour biases accompanying these thresholds compensate to some extent with an existing upper tropospheric dry bias in the climate model. Using all-sky data in spectral regions sensitive to water vapour has the advantage of avoiding problems associated with the process of estimating the clear-sky.

- A far greater agreement is observed between broadband OLR observations and modelled radiances for both the all and clear-sky, suggesting a cancellation of errors across the entire longwave spectrum, with unseen negative biases originating from spectral regions not observed by the HIRS/4 instrument. A lack of high level clouds leading to less emission at FIR wavelengths could be compensating for too much emission at window wavelengths.

- Simple sensitivity tests show that dramatically altering existing cloud properties has little effect on the bias, however raising cloud a maximum of 5 atmospheric levels minimises the error in cloud contaminated channels, but this is due to the introduction of compensating biases. Sensitivities to the way ice clouds are parameterised in RTTOV-10 display a range of up to 2.5 K in window channels but biases in these channels still exceed 3 K for all choices.

Our results are consistent with previous findings that model simulations in cloudy conditions generally overestimate longwave brightness temperatures (Rizzi, 1994; Chevallier et al., 2001; Chevallier and Kelly, 2002), and that climate models share

common biases such as underestimating total cloud, particularly mid and high-topped cloud (Kay et al., 2012). Whereas the Huang et al. (2007a) examination of the infrared spectrum simulated by the GFDL model shows compensating biases that are positive in the window region and negative in the H_2O ν_2 band for the all-sky, HadGEM2-A shows positive biases in both these regions, although those in the latter are a factor of 3 less than those in the former. Though worrying in terms of each model's inability to reproduce the details of the OLR spectrum this at least shows two of the world's climate models are independent in this respect. All of the HIRS longwave channels are biased positively (apart from channel 1, which is due to errors in the low-top model's stratosphere), suggesting that wavelengths not covered by the HIRS instrument are likely to be biased negatively to offset this and produce the low OLR error observed. As the bulk of the OLR is made up from the window and the water vapour rotational band (far infrared wavelengths greater than 15 μm), it is suggested that the latter region contains these errors. This is plausable even with the positive biases seen in H_2O ν_2 band because the rotational band is highly sensitive to clouds, whereas the former is not.

Like most climate modelling centres, the radiation balance in HadGEM2 is controlled primarily by tuning cloud-related parameters (Martin et al., 2011), this option is attractive as it is well know that the representation of cloud processes in GCMs is uncertain, which gives considerable leeway for choice of parameters. Apart from a recent study of the MPI model (Mauritsen et al., 2012) the process of how a model is tuned is not well discussed in the literature, thus we cannot say which tuned cloud parameters are contributing to inaccurate simulations of spectral radiance. The global mean agreement of the modelled net flux with observations is reasonable for the current configuration, however observed TOA outgoing fluxes have uncertainties that approach $\pm$ 4 Wm^{-2} due to possible measurement errors, with OLR being the most uncertain (Stephens et al., 2012). Thus it is entirely possible that fluxes are tuned to the wrong targets. As values become more constrained with improved measurements the model will have to be retuned, which will likely alter cloud properties. However, on a positive note, in contrast to the majority of models (e.g. see Figure 1. of Wang and Su (2013)), much smaller biases are seen in the clear-sky than the all-sky for both the OLR and channels sensitive to clouds. As the tuning process in models is performed for the all-sky it can often mask errors in geophysical quantities

such as temperature. Conversely for HadGEM2-A though, the errors in clear-sky properties appear to be relatively low.

Sole use of TOA radiation cannot give a full insight into the areas of weakness in HadGEM2's cloud parametrisation because it is a cumulative product of the vertical cloud distribution, as well as other atmospheric components. Additionally, as clouds are opaque to infrared wavelengths most radiation is emitted only from the highest clouds of sufficient thickness, which reveals little about those below. Even when the only clouds in the column are low, such as in the stratocumulus regions, they often cannot be seen because their low cloud tops are of a similar temperature to the surface. However, our sensitivity tests on different spectral regions narrow down the possible sources of error, revealing deficiencies in the cloud microphysics are less likely to be contributing than a general lack of cloud in the right places at the right quantities, which has the greatest effect in higher levels of the troposphere at tropical latitudes. This is a problem linked to the way the large-scale and convective cloud parametrisation schemes specify the necessary conditions to diagnose the presence of clouds. Because some error patterns coincide with regions dominated by particular cloud types, such as those associated with deep convection, we may attribute problems to the representation of these clouds. One possibility being the mis-timing of the daily convective maximum, which is known to peak too early in the model (at noon rather than 18:00 to 21:00), so that with the reduced local times sampled by MetOp-A the peak is included in observations but missed by the model.

Simulated radiation studies such as this are a valuable tool for independently verifying the combined radiative effects of climate model output outside of the standard broadband comparison, and can be used to complement more direct evaluations of geophysical cloud properties within climate models.

Chapter 3

IASI OLR Product

3.1 Introduction

Because different thermal wavelengths are sensitive to different atmospheric components, remotely sensed hyperspectral and narrowband radiance measurements contain valuable information about atmospheric, surface and cloud properties, and also reveal fingerprints of long-term climate trends (Harries et al., 2001). Additionally they have a unique value in evaluating climate models (Goody et al., 1998). As such there is a need for detailed and complete satellite observations of terrestrial outgoing longwave radiation (OLR) in the 25 - 3000 cm^{-1} wavenumber range (3 - 400 μm wavelength) at the spectral level (Anderson et al., 2004). At the present time, however, there is no satellite instrument in operation that isolates a substantial part of the OLR with the longest wavelengths, known as the Far Infrared (FIR).

The FIR, which we define as those wavenumbers between 25 - 650 cm^{-1} (15 - 400 μm), is modulated by water vapour absorption in the pure rotation band and, to a lesser extent, the water vapour continuum. For the all-sky Harries et al. (2008) estimate that about 45% of the total OLR from the Earth is from the FIR. Although individual transitions in this region are low in energy because rotational transitions are lower in characteristic frequency than vibrational transitions, the combined intensity of outgoing radiance at these wavelengths is large and absorption is so strong that over much of the FIR the troposphere is nearly opaque. For this this reason

emissions occur mostly in the upper tropospheric and stratospheric regions.

A number of potential uses arise from resolving the FIR with satellite measurements (Mlynczak et al., 2004). Currently retrievals of upper tropospheric water vapour (UTWV) by space-borne instruments exclusively focus on the vibrational-bending mode (ν_2) which is centred at 1595 cm^{-1} (6.3 μm). However research has shown that the radiance from the rotational mode may be up to 6-7 times more sensitive to water vapour changes than the ν_2 mode (Rizzi et al., 2002; Huang et al., 2007b). Harries et al. (2008) estimate the accuracy of the retrieval performance of the FIR to be comparable to, and sometimes slightly better than, an equivalent mid infrared sounder. Given the disproportionally large role that UTWV has in modulating the Earth's radiation balance relative to the fraction of total atmospheric water it makes up, improving the accuracy with which its vertical distribution is measured would have far-reaching benefits. Additionally, continuum absorption, where the absorption of radiation by water vapour varies smoothly with wavelength is an area that is still not fully understood (Shine et al., 2012) and recent case studies have identified discrepancies in the strength of FIR continuum of up to 50% from estimates based on theory (Green et al., 2012). Because the relative humidity is expected to remain constant, the water vapour mixing ratio will increase in a warmer world (Soden and Held, 2006). Given that water vapour is the most important atmospheric gas in terms of greenhouse effect (Miskolczi and Mlynczak, 2004), and given that peak greenhouse forcings occur in the far infrared which implies a strong contribution in directing future climate change (Sinha and Harries, 1995), it is vitally important that we increase our understanding of the role of the FIR with global, long-term observations. Particularly as due to its complexity it is unlikely that global climate models get the impact of feedbacks on the FIR under changing climate right (Harries et al., 2008).

Cirrus clouds have a significant effect on the OLR balance as their cold tops essentially shift radiative emission to lower frequencies, with a higher proportion of the OLR coming from the FIR. The amount of emission is strongly connected with the cloud's height and temperature structure (Maestri and Rizzi, 2003) so essentially clouds can be characterised by their spectral signatures. Rizzi and Mannozzi (2000) estimate that the ratio of FIR to OLR increases by approximately 30% from a clear

scene to a cloudy scene, with stronger effects being seen in ice clouds (Wang et al., 2014; Dessler and Yang, 2003; Mannozzi et al., 1999). With the recent increase of available global cloud property datasets afforded by the range of instruments on the A-Train satellite group, there is a need to gain corresponding complete descriptions of the clouds in terms of their spectrally resolved radiative properties, including over the FIR.

Current operational space borne hyperspectral sounders such as the Atmospheric Infrared Sounder (AIRS) (Chahine et al., 2006) or the Infrared Atmospheric Sounding Interfermeter (IASI) (Blumstein et al., 2004) have been designed to measure only the mid infrared part of the OLR. Photons at FIR frequencies have lower energies than typical band gap energies so suitable photodiodes are difficult to make. Mercury Cadmium Telluride (HgCdTe) detectors such as those used within the IASI instrument can be designed for lower frequencies, however a 650 cm^{-1} cut off is common due to the enhanced sensitivity required to measure below this threshold. In order to maintain the high signal to noise ratio the detector needs to be cooled significantly to reduce the number of photons generated by the detector itself and achieve the precision required. Microwave satellite detectors such as the Microwave Limb Sounder (MLS) or the Advanced Microwave Sounding Unit (AMSU) sense wavelengths that fall just longer than the FIR, however they use very different radiance measurement technologies. Both of these restrictions from either side of the FIR result in an unmeasured segment of electromagnetic radiation that has generally only been observed as part of the total infrared radiation by broadband devices.

Currently the only spaceborne instrument to spectrally resolve part of the FIR has been the Infrared Interferometer Spectrometer (IRIS) which flew onboard the Nimbus 3 and Nimbus 4 satellites in 1969 and 1970 respectively (Hanel et al., 1972). It had a maximum wavenumber of 400 cm^{-1} (25 μm) and a spectral resolution of 2.8 cm^{-1}. Since then, a limited number of instruments have been developed to measure part of, or all of, the FIR. Some have been part of balloon-borne and ground-based campaigns, such as the Atmospheric Emitted Radiance Interferometer (AERI) (Turner et al., 2004), and the Radiation Explorer in the Far InfraRed (REFIR-BB/PAD) (Esposito et al., 2007), whose measurements have been used to test the representation of the FIR by line-by-line radiative transfer models (Bianchini et al., 2008). Aircraft

campaigns using instruments such as the Tropospheric Airborne Fourier Transform Spectrometer (TAFTS) Green et al. (2012), REFIR-PAD (Palchetti et al., 2008), and the Interferometer for Basic Observation of Emitted Spectral Radiance of the Troposphere (I-BEST) Masiello et al. (2012), have been used to gain insights into the FIR continuum. Though these airborne experiments do prove useful for testing parametrisations in radiative transfer models, only spaceborne instruments can give the full Earth coverage of sufficient temporal length needed for climate studies.

Recently, much work has been put into developing and testing a detector proposed for a spaceborne mission with a response in the 50 - 2000 cm^{-1} range at high spectral resolution (approximately 0.643 cm^{-1}). The Far-Infrared Spectroscopy of the Troposphere (FIRST) instrument (Mlynczak et al., 2004) has detectors that are cooled to 4.2K with liquid helium to achieve the necessary sensitivity (for comparison the optical core of IASI is 91.3K). Initial comparisons of FIRST measurements taken on balloon flights against theoretical calculations and spectral overlaps with coincident satellite instruments show excellent fidelity (Mlynczak et al., 2006), however, despite high priority recommendations (see Board et al. (2007)) there is currently no scheduled launch date for its deployment, even though it is often noted that the FIR has been measured extensively and directly on every planet in the solar system except Earth (Hanel, 2003).

Historically, when parts of the infrared spectrum are unmeasured from space the remaining bands have often estimated through alternate means. Previous studies have sought to reproduce total OLR from narrowband and hyperspectral sounders with the combined motivations of validating current operational broadband sounders, mitigating them against potential failure and gaining wider diurnal coverage. The absence of an instrument that measured total outgoing LW flux in the 1970's led to its estimation using a single waveband in the 800 - 950 cm^{-1} window region (10.5 - 12.5μm) from the two-channel scanning radiometer onboard the NOAA-1 to NOAA-5 satellite platforms via a non-linear regression model derived from radiative transfer calculations applied to 99 different atmospheric profiles (Gruber, 1977; Gruber and Winston, 1978). As the reference broadband results are obtained from a radiative transfer code this method is termed 'theoretical'. Alternatively, Ohring et al. (1984) used the Earth Radiation Budget (ERB) broadband OLR measurements on

the Nimbus 7 satellite as a reference to obtain regression coefficients between these and window band observations from the Temperature Humidity Infrared Radiometer (THIR) instrument on the same satellite at collocated footprints. This method is termed 'empirical', because actual measured data is used as a reference.

There are uncertainties involved in using only one narrow band to estimate the entire OLR because the atmospheric information contained in one spectral region is limited, eg. see Gruber et al. (1994). An early theoretical OLR product derived with a multi-spectral regression technique used the 4 infrared channels from the Medium Resolution Infrared Radiometer (MRIR) on the Nimbus-3 satellite (Raschke et al., 1973). This method has been adapted for use with the High Resolution Infrared Sounder (HIRS) instruments that have been operational since 1978, thus providing a continuous longterm surrogate for total OLR (Ellingson et al., 1989a). The product has been continuously developed since its creation and has demonstrated extremely high correlations with CERES broadband data (Lee et al., 2007). Recently, Sun et al. (2010) have used the empirical approach to derive broadband data from AIRS using the CERES outgoing LW flux to generate regression coefficients from principal component analysis of AIRS radiances.

Traditionally, these methods employ data from instruments that fly on polar orbiting satellites which are beneficial for global climate studies in terms of their high spatial coverage. However, as they are restricted to monitoring each subsatellite point just twice a day they fall short of the requirements for diurnal analyses. Geostationary satellites, on the other hand, complete a full Earth scan in approximately 30 minutes thus capturing the daily variability, but are restricted to one nadir location with views at increasingly unfavourable angles away from the subsatellite point. Gube (1982) was the first to use geostationary radiances from the 2 infrared channels (10.2 - 13 μm and 5.7 - 7.5 μm) on the METEOSAT-1 satellite to estimate total OLR flux theoretically. Schmetz and Liu (1988) modified this approach using METEOSAT-2 data to include a better treatment of limb-darkening using the method developed by Abel and Gruber (1979), and Cheruy et al. (1991) calculated the relationship between METEOSAT-2 data and collocated footprints from broadband Earth Radiation Budget Experiment (ERBE) measurements to produce empirical regression coefficients. The Geostationary Operational Environment Satellite 6 (GOES-6) Imager window

channel (10.2 - 12.2 μm) has also been employed in an empirical estimation of OLR fluxes using ERBE data (Minnis et al., 1991), and Lee et al. (2004) blended HIRS OLR fluxes from polar satellites with GOES-8 Imager data to provide OLR data to incorporate multi-spectral information on temperature and humidity at different elevations, with wider diurnal coverage.

The body of work that exists surrounding the derivation of broadband OLR from narrowband mid infrared measurements is extensive and on-going, however, as regards spectrally resolved measurements in the FIR, progress is limited to a handful of studies. Huang et al. (2006) use clear-sky radiances from the IRIS instrument to predict fluxes in its uncovered spectral regions below 400 cm^{-1} and above 1400 cm^{-1} by assuming a linear relationship between these regions and fluxes in the H_2O ν_2 band and a narrow window region. Regression coefficients between measured and unmeasured wavebands are obtained from calculated radiances using the MODTRAN radiative transfer model applied to simulated profiles from the GFDL AM2 global climate model. These coefficients are then applied to IRIS to simulate the whole OLR. Huang et al. (2008) adapt this theoretical method for the hyperspectral Atmospheric Infrared Sounder (AIRS) to derive spectral fluxes in its uncovered wavebands using principle component analysis. A complete set of clear-sky fluxes from 10 to 2000 cm^{-1} are calculated at 10 cm^{-1} intervals, and validated with broadband observations using collocated CERES data for the tropical oceans. Corresponding studies were carried out for cloudy data (Huang et al., 2010), and additional years (Huang et al., 2013). Chen et al. (2013) extend this work to include land and extra-tropical ocean regions using clear-sky data only.

In lieu of complete FIR observations we follow a theoretical approach and develop an algorithm to 'fill in the gaps' of the available data, but with a spectral resolution and range of estimated wavenumbers that is an advance on previous studies. To do this we use the IASI instrument which measures in the mid infrared, originally designed to fulfil both meteorology requirements of high spatial coverage, and atmospheric chemistry needs such as accuracy and detailed vertical resolution (Clerbaux et al., 2009). IASI has 4 times as many channels as the AIRS instrument for the same range of thermal infrared wavelengths, and is free from gaps over the whole spectral range. It is part of the payload of the MetOp-A satellite, which provides a differently timed

polar orbit and hence a different sampling of the diurnal cycle to existing satellites that carry broadband instruments. In the absence of any current spaceborne instrument that isolate the FIR our new algorithm has the potential to provide valuable proxy measurements, within the limitations of the spectroscopy implemented in the radiative transfer code, that is used to derive the prediction model. To ensure high accuracy we use the Line-By-Line Radiative Transfer Model (LBLRTM) (Clough et al., 1992, 2005) available publicly at `http://rtweb.aer.com`, which has a long and successful heritage of being at the leading edge of the field, is continually updated and has been well validated, see for example (Shephard et al., 2009; Delamere et al., 2010; Alvarado et al., 2013).

This study differs from most of its associated predecessors by remaining in the directional radiance regime, with no attempt made to translate unfiltered IASI radiances or the total integrated OLR product to flux densities at this stage. Flux is calculated by integrating the measured radiance over all solid angles, which can be split into zenith and azimuth angles. The outgoing radiation field is strongly anisotropic and must be estimated using a predetermined model, of which many exist involving varying degrees of sophistication and assumptions. These can be either theoretically determined using radiative transfer model calculations of flux or empirically derived using satellite measurements over several different viewing angles and locations, for example see Clerbaux et al. (2003); Loeb et al. (2003); Kato and Loeb (2005). The resulting Angular Distribution Models (ADMs) relate the radiance measured at a single angle to irradiance estimated over all angles, and as such introduce a further level of uncertainty into the validation, which can be up to 2.3% for recent satellite products (Instantaneous LW TOA flux: see the CERES Terra Edition3A SSF Data Quality Summary). To avoid confusion we use the abbreviation INLR (Integrated Nadir Longwave Radiance) to refer to the extended spectrum of IASI radiances that has been integrated over all wavenumbers, and is distinct from OLR which is synonymous with the integrated fluxes. This approach has the advantage of allowing for a cleaner comparison with climate model simulated satellite products. The adaption of the methodologies adopted in this study for the additional calculation and evaluation of flux quantities are left for future studies.

We use a theoretical based regression technique similar to the one used to derive

OLR from the HIRS instrument based on physical atmospheric profiles which is described in section 3.2.2. In order to verify the extended IASI spectrum we compare the calculated INLR with broadband CERES instruments on other satellites, which avoids the introduction of compounded errors from radiative transfer model evaluations. Section 3.2.4 explains how times and locations are identified where the path of MetOp-A crosses those of the Aqua and Terra satellites, both of which carry CERES instruments. By restricting this set further to only nadir looking views the instruments will sense the same atmospheric path at the same time, providing the opportunity for indirect validation of the new IASI product. Results of this, and a global composite comparison, are presented in section 3.3.1 and section 3.3.2 respectively. Finally the complete constructed IASI spectrum is presented in the remaining sections 3.4.1, 3.4.2 and 3.4.3.

3.2 Data and Methodology

3.2.1 IASI Level 1c and Combined Sounding Products Data Set

The IASI Flight Model 2 (FM2) instrument is onboard the MetOp-A satellite launched by EUMETSAT in October 2006 which operates in a sun-synchronous orbit. It is a 8461 channel passive sounder that measures in the mid infrared spectral region between 645 - 2760 cm^{-1} (3.62 - 15.5 μm) at a 0.25 cm^{-1} sampling interval with no gaps. The apodised level 1c radiances have a 0.5 cm^{-1} resolution. The effective field of view (EFOV) is a 2 x 2 matrix of 4 circular instantaneous fields of view (IFOV) that each have an approximate footprint diameter of 12 km at nadir. There are 30 EFOV per scan line which takes 8 seconds to complete and had a maximum scan angle of 48.3 ° in the across track direction. In its nominal mode IASI uses a view of an internal blackbody and deep space once every scanline to calibrate on-board, as described by Simeoni et al. (2004). It is thought to have an average absolute radiometric accuracy of 0.5K, measured in brightness temperature (personal communication with EUMETSAT).

We restrict the data to the IFOVs with the smallest satellite zenith angles in order to

retain only nadir looking pixels. There are 4 IFOVs with angles less than 1.5 ° which are indices 57, 58, 63 and 64 in the across track direction and have viewing angles of 1.34 °, 1.37 °, 1.41 °, and 1.39 ° respectively. Alongside the level 1c radiances clear-sky flags are obtained from the related level 2 combined sounding products to construct an equivalent clear-sky product. Cloud detection in IASI pixels is performed from a choice of 5 separate tests, involving window channels, AMSU-A, AVHRR and CO_2 slicing, depending on the quality of the input data.

3.2.2 Method for Estimating OLR from IASI

The methodology and correlation coefficients derived in this section were developed by Dr. Hai-Tien Lee[1]*. He also prepared the 4 Figures. The application of the coefficients to IASI data, and the interpretation thereof in the remainder of the chapter were my own work.*

Strong correlations are found between frequencies in the LW spectra with similar spectroscopic properties. Unmeasured radiances with FIR wavenumbers between 25 and 650 cm^{-1} and those between 2760 and 3000 cm^{-1} (which we will term near infrared (NIR) radiances) can be estimated from IASI observations. For example, FIR wavenumbers in the strong H_2O rotational band at 25.25 cm^{-1} have strong correlations with those in the centre of the 667 cm^{-1} CO_2 and 1533 cm^{-1} H_2O ν_2 bands by virtue of their similar sensitivity to high altitude temperatures (Figure 3.1). However the 1533 cm^{-1} band is physically more similar to frequencies in the FIR and therefore has comparably larger correlations.

Adapting the simulation methodology of Ellingson et al. (1989a), the Line-By-Line Radiative Transfer Model (LBLRTM) is used to simulate LW spectra over the spectral range 25-3000 cm^{-1} at 0.5 cm^{-1} resolution with radiosonde data from 1600 soundings (Phillips et al., 1988). This dataset was carefully compiled by Dr. Norman Phillips with the purpose of creating a representative sample of the range of conditions found in the atmosphere, and has been demonstrated to be adequate enough to base global models upon, see Ellingson et al. (1989b). The following details from

[1]Email: lee@umd.edu Address: Earth System Science Interdisciplinary Center, University of Maryland, College Park, Maryland, USA

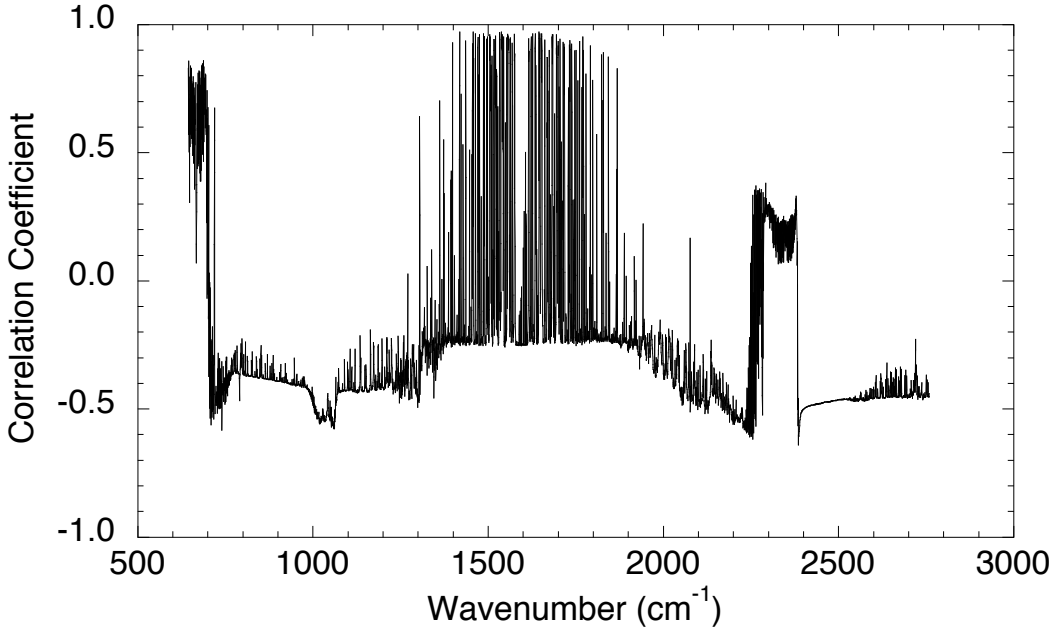

Figure 3.1: Linear correlation coefficients between the radiance at 25.25 cm^{-1} and the rest of the spectrum. Data is simulated by the LBLRTM from Phillips Soundings. Work pertaining to this figure was completed by Hai-Tien Lee.

Ellingson et al. (1989a) describe the dataset. Each sounding includes temperature values at 65 different pressure levels from 0.1 to 1000 mb and mixing ratios of H_2O and O_3 in the corresponding 64 layers. The soundings were compiled from radiosonde ascents from land and ocean stations between 30 ° S and 60 ° N and the soundings were equally divided between tropical (30 ° S - 30 ° N) and midlatitude (400 summer and 400 winter) conditions. The O_3 data was chosen to be climatologically consistent with the temperature profiles, and the stratospheric H2O mixing ratio is assumed to be 3 ppmm. A second set of cloudy simulations was obtained by inserting a cloud into each profile at a particular level (randomly distributed) to give 3200 different conditions, 1600 clear and 1600 cloudy. The water vapour profile was not altered when a cloud layer was included and the clouds were nearly uniformly distributed in low (950 - 850 mb), middle (675 - 525 mb) and high (400 - 240 mb) layers. Clouds are all considered to have 100% horizontal coverage of the profile. Those with cloud top pressures greater than 450 mb are assumed to be spectrally black whereas the high level clouds are assumed to have the spectral properties of cirrus given by Haurwitz

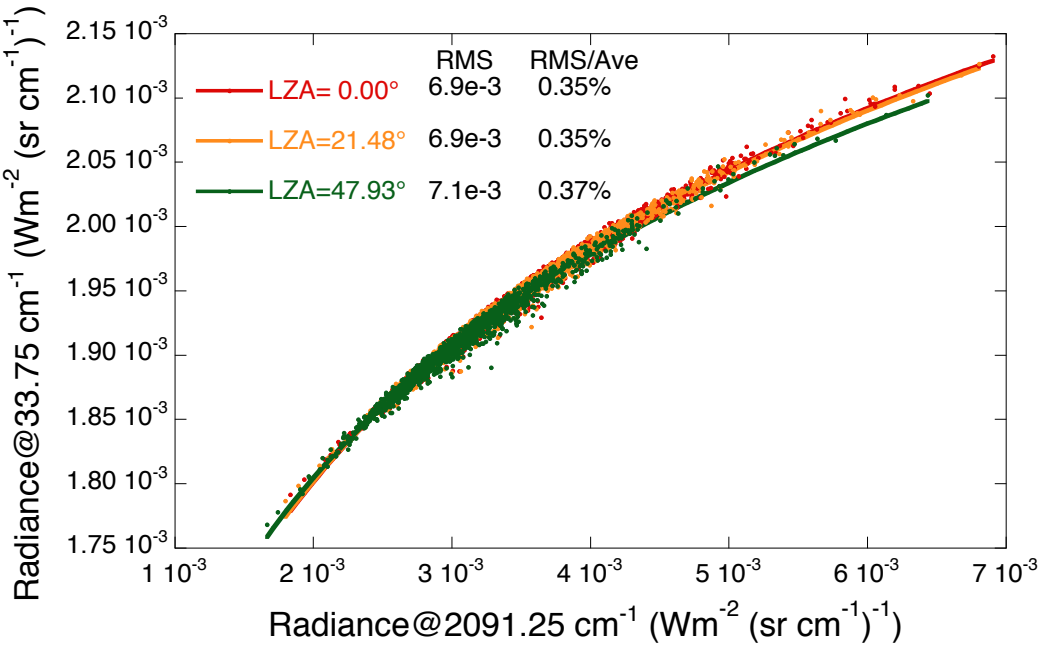

Figure 3.2: Relationship of radiances at 33.75 cm^{-1} and 2091.25 cm^{-1} simulated by LBLRTM from Phillips Soundings, where the scatter points and fitting curve are based on data for local zenith angle 0 ° (red), 21.48 ° (orange), and 47.93 ° (green), respectively. Units are $Wm^{-2}sr^{-1}(cm^{-1})^{-1}$. Work pertaining to this figure was completed by Hai-Tien Lee.

and Kuhn (1974).

Several regression model formulations were investigated for the purpose of NIR/FIR radiance prediction. A log-log transformation was found to provide the optimal performance in minimization of estimation errors and regression residual distributions. This empirical behaviour can also be explained physically, as transmittances vary with optical path via an exponential relationship and hence the model will be approximately linear. Figure 3.2 shows an example of the log-log relationship between radiances at 33.75 cm^{-1} and the channel that has a maximum correlation with it (2091.25 cm^{-1}).

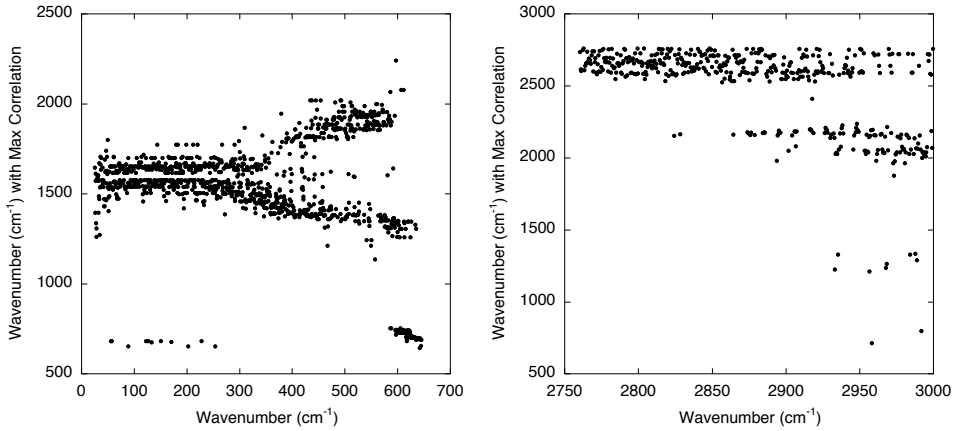

Figure 3.3: The wavenumbers of IASI observed radiance spectrum (y-axis) that show empirically the maximum correlation coefficients for the FIR (left) and NIR (right) wavenumbers (x-axis), based on a log-log transformation. Work pertaining to this figure was completed by Hai-Tien Lee.

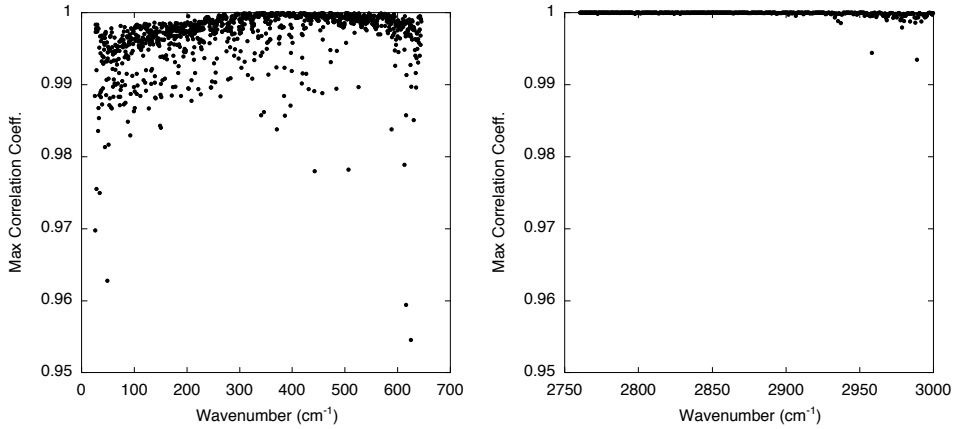

Figure 3.4: The maximum correlation coefficients between wavenumbers in the FIR (left) and NIR (right) and the corresponding predictor wavenumbers shown in Figure 3.3. Work pertaining to this figure was completed by Hai-Tien Lee.

The best predictor channels are selected as those with maximum correlation coefficients between the log-radiances (Figure 3.3) whose values are shown in Figure 3.4. For this application the local zenith angle is restricted to the nadir cases. The prediction equation to estimate the radiance $I_{\nu_{FIR/NIR}}$ in either the FIR or NIR regions

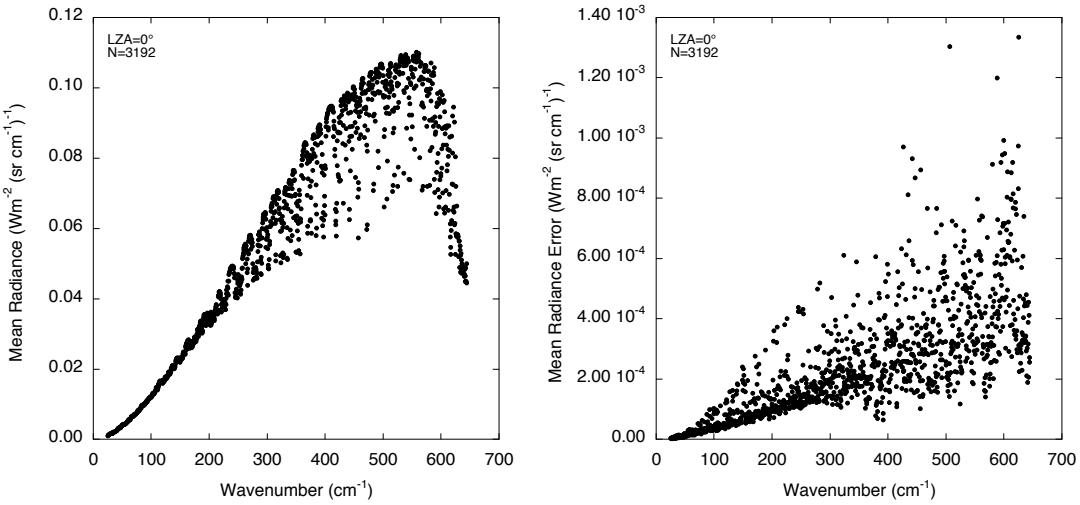

Figure 3.5: The mean FIR radiance spectrum based on all LBLRTM simulations performed with the 3192 radiosonde profiles (left), and the spectral radiance estimation errors (regression rms errors) associated with them (right). All simulations shown are for a local zenith angle of 0 °.

at wavenumber ν can be written as,

$$\ln(I_{\nu_{FIR/NIR}}) = a_0 + a_1 \ln(I_{\nu_{predictor}}) \tag{3.1}$$

where $I_{\nu_{predictor}}$ is the radiance observed by IASI at the predictor wavenumber ($\mathrm{Wm^{-2}sr^{-1}(cm^{-1})^{-1}}$) and a_0 and a_1 are the calculated regression coefficients. The mean spectral radiance calculated by LBLRTM for each wavenumber in the FIR is shown in the left panel of Figure 3.5 and has a total integrated value of 36.32 $\mathrm{Wm^{-2}sr^{-1}}$. The corresponding value for the NIR region is 0.028 $\mathrm{Wm^{-2}sr^{-1}}$. The root mean square (rms) errors in the regression model serves as the theoretical estimates for the modelling uncertainties in the reconstructed spectrum. The right panel of Figure 3.5 shows these errors for the FIR region. The root mean square of the sum radiance errors, including cancellations from positive and negative values, is 0.054 $\mathrm{Wm^{-2}sr^{-1}}$ over all simulated regions which gives a total relative error of 0.15%. Individual root mean square relative errors are shown in Figure 3.6 which shows a very low dependency on wavenumber.

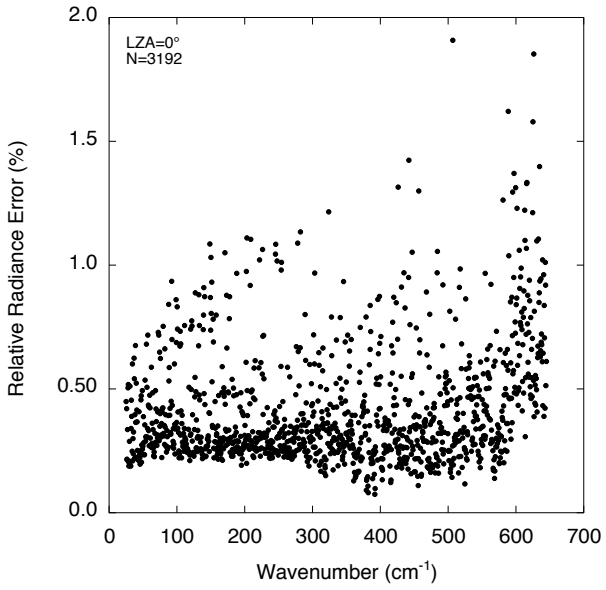

Figure 3.6: Relative radiance estimation error for the FIR region. Calculated from the root mean square values of the radiance errors divided by the mean radiance spectrum (the right and left plots of Figure 3.5 respectively).

3.2.3 CERES Single Scanner Footprint (SSF) Ed3A

The INLR product constructed from the extended IASI radiances is compared with the existing CERES directional radiance product. The CERES SSF Edition 3A dataset is obtained from the Atmospheric Science Data Center at the NASA Langley Research Center for both the Terra and Aqua polar orbiting satellites (Wielicki et al., 1996). In the cross-track scanning mode there are 90 FOVs in a single scanline with a 25 km footprint at nadir, however in terms of measurements and products it usually considered at a resolution of about 20 km. The swath takes 6.6 seconds to complete and has a maximum scan angle of 65.8 °. For the present study only pixels with the minimum satellite zenith angles, which are less than 1 ° (FOV 45 and 46) are selected to retain only nadir-looking views. Cloud properties for CERES instruments are inferred from the Moderate-Resolution Imaging Spectroradiometer (MODIS) imager which flies on the same satellites, and are based on threshold tests with adjacent channels (Minnis et al., 2004). Each satellite carries 2 identical CERES instruments. For the data acquired, Flight Model 1 (FM1) on Terra and Flight Model 3 (FM3) on Aqua are operational in the cross-track mode.

CERES measures filtered radiances in terms of physical origin (i.e. thermal or solar), rather than imposing wavelength boundaries, however approximate ranges for the 3 channels are reflected shortwave (SW) (0.3 - 5 μm), total (0.3 - 200 μm), and window (8 - 12 μm). LW radiation is determined from a weighted combination of measurements from the other channels and hence all emitted thermal radiances that fall within the 0.3 - 200 μm (50 - >3000 cm^{-1}) range are included.

Relative errors due to the process of unfiltering radiances are found to be generally less than 0.2% in the LW (Loeb et al., 2001). The uncertainty in net TOA flux due to absolute calibration uncertainty including the radiance-to-flux conversion is 2% in the SW channel and 1% in the total channel at the 95% confidence level (Priestley et al., 2002). Since nighttime LW radiation is based only on the total channel the uncertainties are essentially the same at 1%. For the daytime combining the uncertainties of the SW channel yields an estimate of around 2.1%, which produces an average daily LW uncertainty of 1.5% (see appendix of Loeb et al. (2009) for the derivation). Given that the the present study uses CERES unfiltered radiances only, contributed uncertainties from the radiance-to-flux conversion do not apply, but as these errors are unknown the total level of uncertainty has an upper bound of about 1.5%.

Determining absolute radiometric calibration uncertainty once in-orbit is dependent on a reference instrument and it remains a challenge to achieve a reference traceable to international standards. This is a problem of such critical importance that it led to the formation of an international effort called the Global Space-Based Intercalibration System (GSICS) (Goldberg et al., 2011). The current CERES Edition-3 product established FM1 as the reference to place all the CERES instruments of the same radiometric scale and as such will contain fewer correction uncertainties. All flight models were corrected for spectral darkening at shorter wavelengths (<1 μm) due to UV exposure which caused degradation in both the SW channel and the shorter wavelength region of the total sensors. Studies that use an edition of CERES prior to Edition 3 will be subject to this error, which overestimates flux by as much as a 0.8% (CERES LW flux daytime for FM1 and FM3: see the CERES Terra and Aqua Edition3A SSF Data Quality Summary). Further refinements for the spectral correction have been proposed for the CERES Edition 4 production (Thomas and Priestley, 2014). This revision is expected to improve the accuracy and stability of CERES data, particularly over the daytime land scenes. The present study uses

CERES Edition 3 data and as such, it is important to be aware of the possible errors relating to this version.

3.2.4 Identifying Simultaneous Nadir Overpasses

Two satellites in sun-synchronous polar orbits with different equatorial crossing times will cross in the polar regions at approximately the same north/south latitude each time. When radiometers from both satellites view the same nadir scene at the same time this is called a simultaneous nadir overpass (SNO). Using SNOs is preferable to comparing composite measurements over the same time period because individual scene differences between cloud and surface properties are avoided. This study uses the database of predicted SNOs provided by the National Calibration Center of NOAA; available at http://ncc.nesdis.noaa.gov/SNO/SNOs//NCC_SNOs_prediction_service.html which makes SNO predictions based on the SGP4 orbital perturbation model (Cao et al., 2004).

Aqua has local equatorial crossing times (LECTs) of 13.30 (ascending) and 01.30 (descending), and Terra has LECTs of 22.30 (ascending) and 10.30 (descending). MetOp-A has an ascending node of 21:30 and a descending node LECT of 09:30. 2012 SNOs between MetOp-A and Aqua, and MetOp-A and Terra, are first filtered following the criteria set out in the methodology of Cao et al. (2005a). This specifies that at the SNO: 1) the time difference between nadir pixels is less than 30 seconds and, (2) the distance between nadir pixels is less than the diameter of one footprint. Based on the average of the 20 km CERES pixel and the 12 km IASI pixel this threshold is set to 16 km. This yields approximately 100 SNOs for each satellite pair over the course of a year. Using the predictions the closest matches in terms of time and distance were identified in the satellite data for the most nadir-looking field of views for each instrument. The resulting locations of IASI pixels identified as SNOs are shown in Figure 3.7. By virtue of their different equatorial crossing times MetOp-A and Aqua SNOs all lie around 74 ° N/S and MetOp-A and Terra SNOs all lie around 81 ° N/S. We estimate the biases for the rest of the globe by additionally performing a composite comparison of OLR products in section 3.3.2.

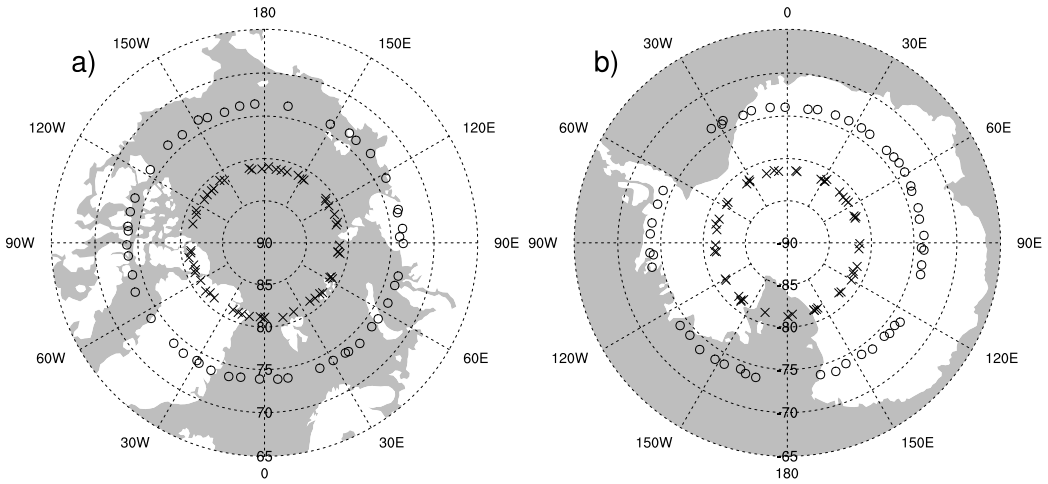

Figure 3.7: Locations of nearest nadir viewing SNOs, chosen as described in section 3.2.4 between Metop-A and Terra (inner crosses) and Aqua (outer circles) for a) the Arctic, and b) Antarctic, for 2012.

3.3 Validation of INLR with CERES

3.3.1 Simultaneous Nadir Overpasses

For maximum consistency with CERES, IASI INLR radiances are cut off at the 50 cm^{-1} lower wavenumber limit, and integrated over all remaining radiances up to 3000 cm^{-1}. INLR estimates from coincident IASI and CERES pixels generally lie close together, with the majority falling within 2 $Wm^{-2}sr^{-1}$ of each other (Figure 3.8). In general differences will be introduced by the slightly different nadir angles and footprint sizes between CERES and IASI, and the accuracy of the colocations. Absolute values range from 30 to over 80 $Wm^{-2}sr^{-1}$ yet there is no identifiable relationship between scene radiance and bias indicating the IASI algorithm is robust against profile conditions at these latitudes. Nighttime radiances show a slightly higher correlation (0.99) compared with daytime scenes (0.98). Whether the lower daytime correlation originates from errors in the SW channel involved in estimating daytime CERES radiances, solar backscatter contamination of either instrument or the increased variability of daytime radiances is beyond the scope of this study.

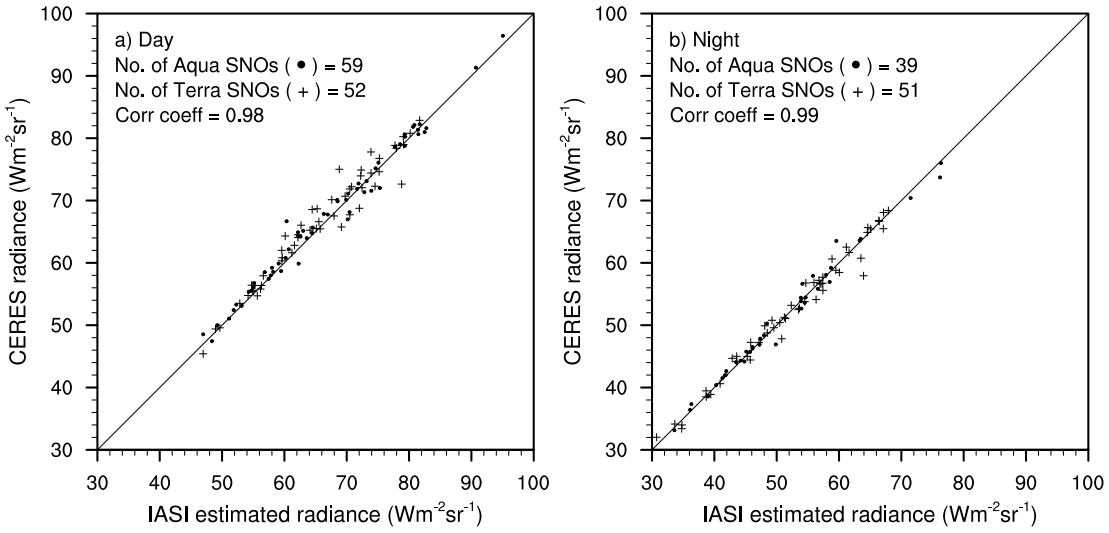

Figure 3.8: Absolute values of instantaneous LW radiances constructed from IASI on Metop-A against CERES measurements for both the Terra and Aqua satellites at closest SNO events for 2012 for a) day, and b) night.

Table 3.1: Instantaneous biases between CERES and IASI INLR at SNO events with standard errors. Standard errors are the standard deviations divided by the square root of the total number of points. Units are $Wm^{-2}sr^{-1}$. Figures in brackets are relative differences between the bias and the mean radiation measured by both CERES and IASI.

	All times	Day	Night
Both	0.33 ±0.11 (0.50%)	0.61 ±0.17 (0.95%)	-0.02 ±0.14 (0.01%)
Aqua	0.33 ±0.14 (0.57%)	0.48 ±0.20 (0.78%)	0.11 ±0.19 (0.25%)
Terra	0.32 ±0.18 (0.50%)	0.76 ±0.28 (1.15%)	-0.12 ±0.2 (-0.17%)

The same results shown as absolute biases (CERES - IASI) are presented as a time series in Figure 3.9, revealing no dependency of error upon season. Table 3.1 breaks down these biases by CERES instrument. Mean IASI INLR values are about 0.3 $Wm^{-2}sr^{-1}$ lower than CERES when all local times are considered, and individual differences are generally within ±6 $Wm^{-2}sr^{-1}$. Larger biases appear to be associated with partly cloudy or overcast scenes and are likely due to horizontal cloud inhomogeneity in the region of the SNO which can have a large effect on the height, and hence temperature/radiance of emission.

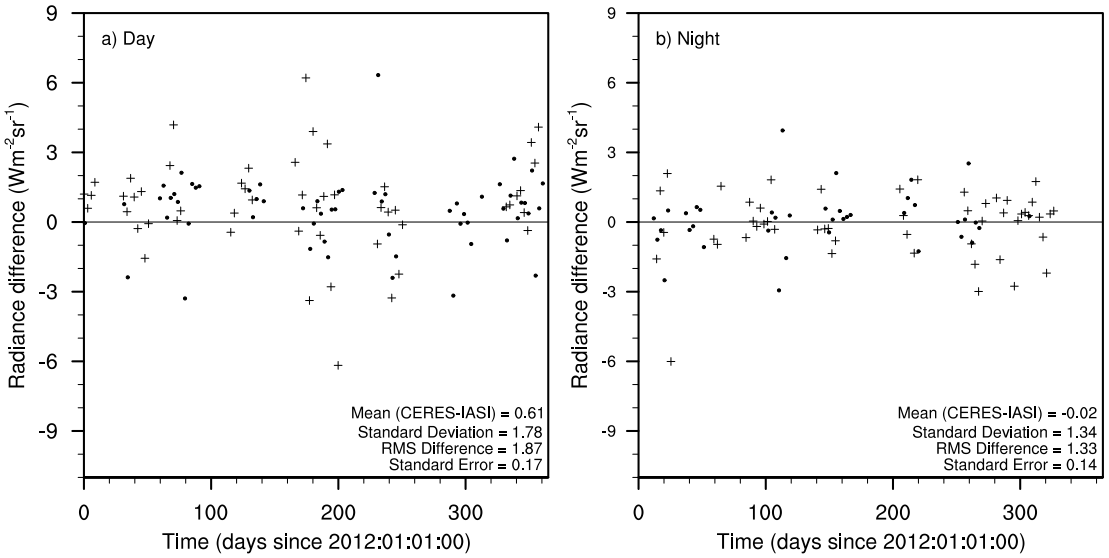

Figure 3.9: Time series of LW radiance bias at SNOs between CERES and IASI for 2012 for a) day and b) night. CERES measurements from Terra are marked with crosses and those from Aqua are shown as dots.

When relative differences are considered this corresponds to LW radiances that are 0.5% higher in CERES than IASI. Split into day and nightime scenes it is apparent that this bias is dominated by daytime pixels as the mean nighttime relative error is only 0.01% whereas daytime differences are 0.95%. This could be related to the CERES Ed4 findings about the SRF correction determination method. All relative differences are well within the uncertainty range of CERES unfiltered radiance based on absolute radiometric calibration uncertainty and relative unfiltering errors as detailed in section 3.2.3. Given that the original correlation co-efficients between radiances were calculated using only tropical and mid-latitude profiles, the fact that the algorithm performs so well in polar regions shows that it is highly robust under different scene types.

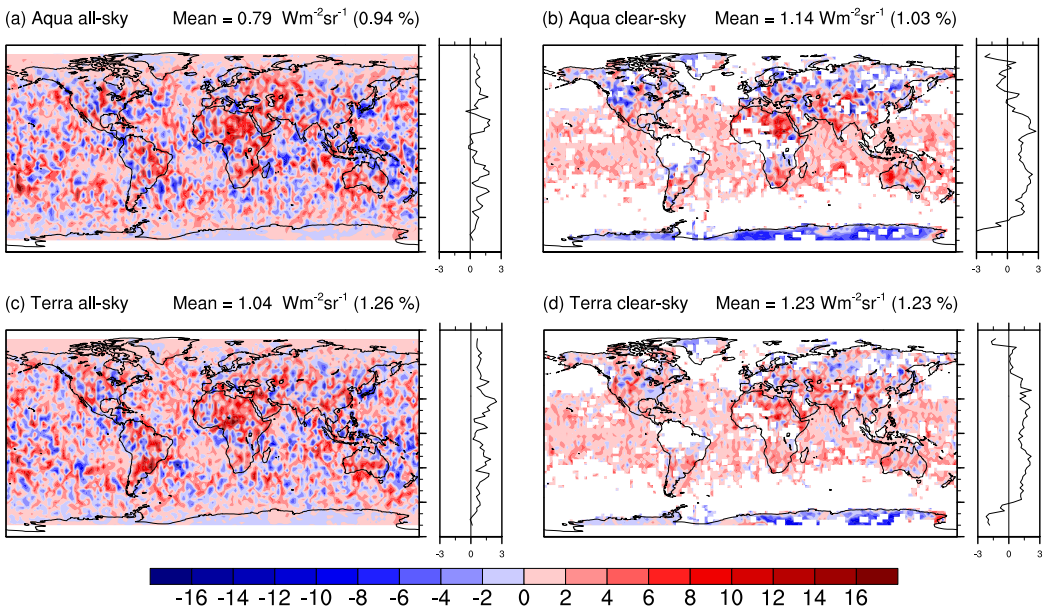

Figure 3.10: Differences between monthly gridded and averaged total LW radiances (CERES - IASI) at all available local times in April 2012 for: a) Aqua all-sky, b) Aqua clear-sky, c) Terra all-sky, and d)Terra clear-sky. Zonal means are shown to the right. Units are $Wm^{-2}sr^{-1}$. Figures in brackets are relative differences between the bias and the mean radiation measured by both CERES and IASI.

3.3.2 Global composite INLR

In order to obtain an estimate of the magnitude of extra-polar biases, gridded and averaged nadir data from CERES (Aqua and Terra) for the whole month of April 2012 is compared with the equivalent constructed INLR composite from IASI (Figure 3.10). For a single day there are approximately 40,000 pixels collected for each instrument, binned to a 2.5° x 2.5° grid. Global mean biases split into day and night time scenes along with the differences between Aqua and Terra are also shown in Table 3.2.

Table 3.2: Global mean biases between IASI INLR and CERES instruments for April 2012. Units are $Wm^{-2}sr^{-1}$. Figures in brackets are relative differences between the bias and the mean radiation measured by both CERES and IASI. Italic figures in brackets are the biases split by land and ocean respectively.

	All times	Day	Night
Aqua CERES - IASI			
All-sky	0.79 (0.94%)	1.44 (1.65%)	0.16 (0.18%)
Clear-sky	1.14 (1.03%)	3.03 (3.00%)	0.46 (0.22%)
Terra CERES - IASI			
All-sky	1.04 (1.26%)	1.40 (1.65%)	0.70 (0.87%)
Clear-sky	1.23 (1.23%)	1.80 (1.81%)	1.16 (1.15%)
Terra - Aqua CERES			
All-sky	0.26 (0.32%)	-0.04 (-0.01%)	0.54 (0.69%)
Clear-sky	0.08 (0.17%)	1.28 (1.27%)	0.72 (0.94%)

The IASI INLR product continues to be underestimated with respect to CERES when the whole globe is averaged together, with a bias that is about 3 times greater than the SNO mean bias for both Aqua and Terra (0.79 and 1.04 $Wm^{-2}sr^{-1}$, with a relative error of 0.94 and 1.26% respectively) in the all-sky. This increase is not wholly unexpected due to the nature of the compositing process and it is likely to be dominated by diurnal variations, which is evident from the general noisiness of the data in Figure 3.10. More extreme differences can be seen over land and deep cloud regions where diurnal variations are greatest. Dealing with clear-sky pixels only removes the cloudy part of this diurnal variation. On a daily basis clear-sky is identified in 15% of the data, but when gridded and averaged over the month 70% of the globe has clear-sky data. As CERES and IASI use different methods to detect clouds it is possible that they would interpret the cloudiness of the same scene differently thus incorporating a possible systematic bias into the clear-sky comparisons, which are all observed to be higher than their all-sky equivalents.

The difference due to the 3 hour local time difference between Terra and Aqua (0.26 $Wm^{-2}sr^{-1}$ in the all-sky) indicates time sampling issues are not relatively significant, though a longer time period would undoubtedly reveal clearer patterns. Data volume issues prohibit testing this currently. As with the SNO comparison biases between OLR products are significantly larger in the daytime which falls in line with the ex-

isting correction error identified in the Ed3 CERES data mentioned in section 3.2.3. However, with the exception of daytime clear-sky differences between Aqua CERES and IASI, relative mean biases are still within the uncertainty ranges estimated for CERES for all time periods and given the uncontrollable factors involved in the composite process this gives us confidence that the algorithm used to estimate IASI OLR is spatially robust.

3.4 Spectral IASI OLR

3.4.1 Instantaneous spectral IASI OLR

Example extended instantaneous IASI radiance spectra from 17th April 2012 show that the estimated FIR contributes between 42 - 64% to the total INLR depending on the scene type (Figure 3.11). This is within the range of previous estimates (Harries et al., 2008). We present night time scenes which is when the FIR is particularly dominant as temperatures fall. In the daytime, however, higher surface temperatures often allow the window region to reach higher intensities when there is little or no cloud (Lindfors et al., 2011). In non-cloudy cases temperature is the dominating factor controlling the total intensity of LW radiance received at the TOA. For example, the spectrum over the Sahara (Figure 3.11c) emits about double the total radiance as that over Antarctica (Figure 3.11d). However when clouds are present their height and coverage can have a highly significant influence. For example it is certain that the temperature in the tropics will be higher than that in Antarctica, and yet Figure 3.11a and Figure 3.11d have similar values of total INLR. This is because it is likely that deep convective cloud brings the height of tropical emission to the cold upper troposphere where photons have lower energies. Clouds give more weight to the FIR as part of the INLR overall. The desert and the tropics are both warm regions and yet the FIR contributes 42% of the former clear dry case and 62% of the latter moist cloudy case, which is almost a third greater. The low stratiform clouds that are prevalent over midlatitude land will not have as large an effect on the whole spectrum (Figure 3.11b), but emission in the window region is still reduced with respect to the FIR.

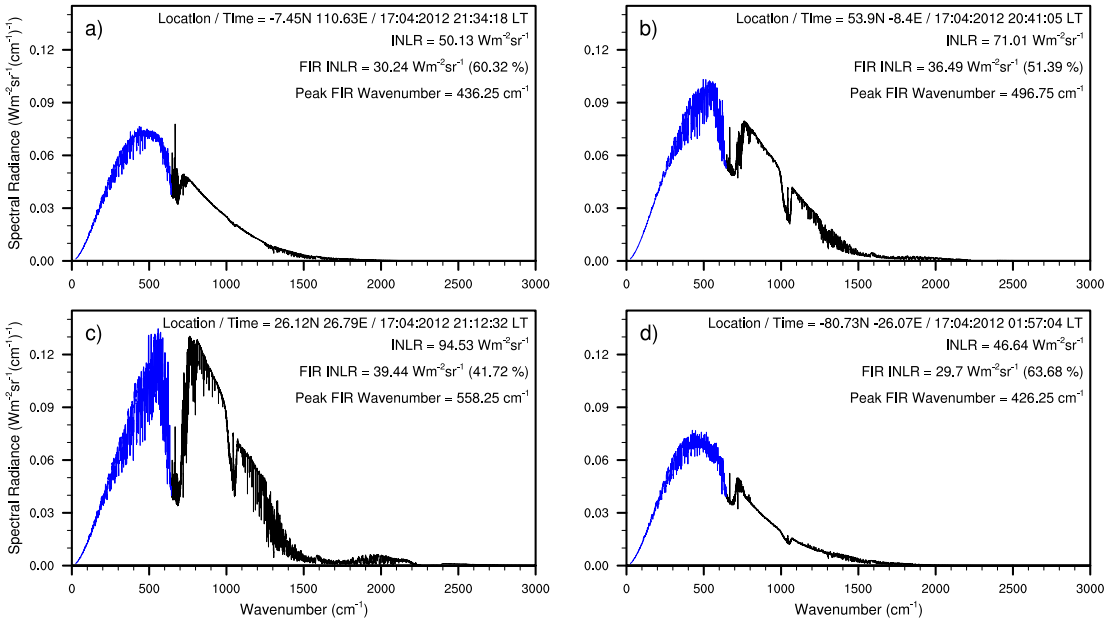

Figure 3.11: The total outgoing longwave spectral radiance (25.25 - 2999.75 cm^{-1}) constructed from IASI measurements (black) and estimated far infrared radiances (blue) for 4 instantaneous scenes over: a) tropical equatorial land, b) midlatitude land, c) the Sahara desert, and d) Antarctica. All are night-time scenes from the 17th April 2012.

3.4.2 Mean clear and cloudy spectral IASI OLR

When split into global mean clear and cloudy scenes an average of 47% of the total LW radiance comes from wavenumbers less than 645 cm^{-1} when clouds are always present, and 44% when the atmospheric column is clear (Figure 3.12a). The peak wavelength of emission also shifts from 558.25 to 513.25 cm^{-1} in the cloudy only case. The NIR region constructed from a similar method contributes near-negligible radiances of 0.03 $Wm^{-2}sr^{-1}$ (0.04%) in cloudy cases and 0.05 $Wm^{-2}sr^{-1}$ (0.06%) in clear cases. This is a region of partial transparency and hence like the 800 - 1250 cm^{-1} window dominates more in the clear-sky.

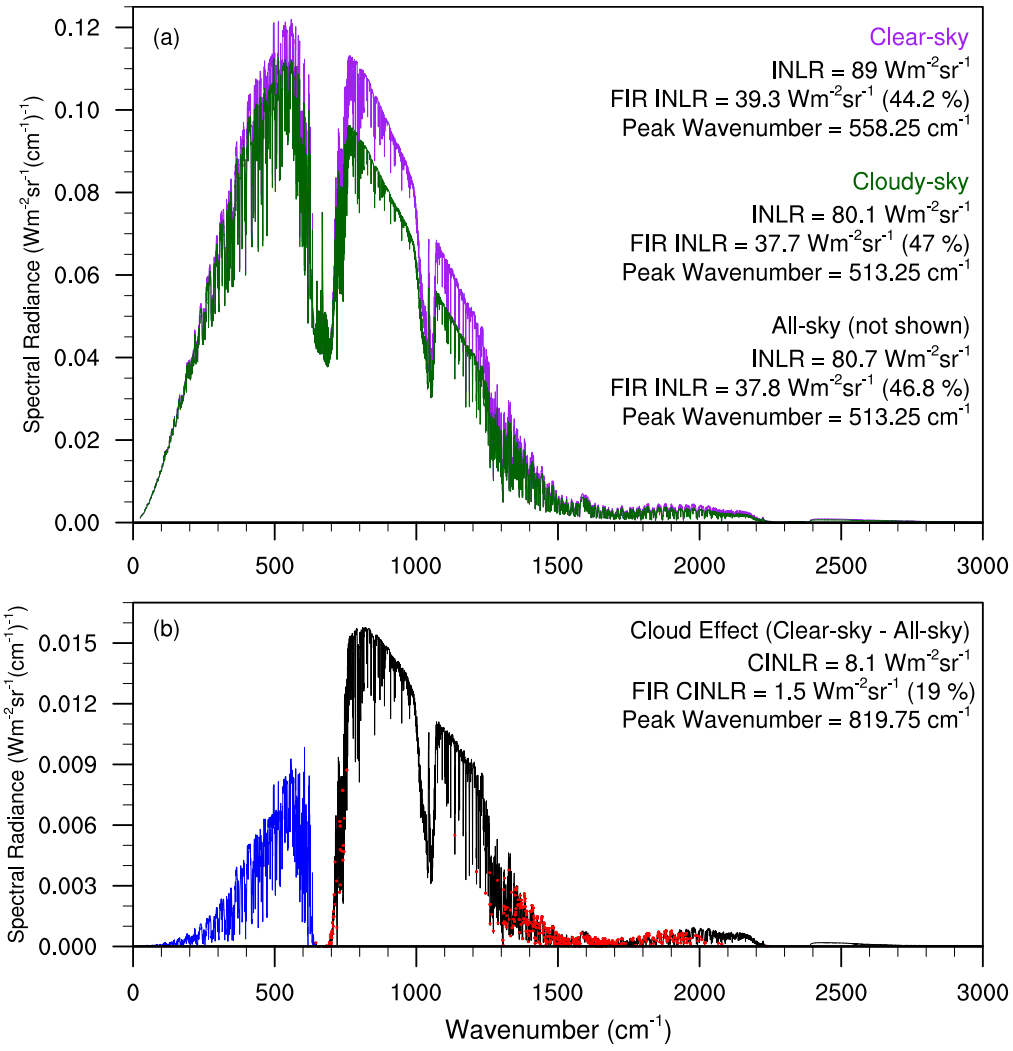

Figure 3.12: The outgoing longwave spectral radiance constructed from IASI data globally averaged for: a) clear (purple) and cloudy (green) pixels. Numbers in parentheses are the fractional FIR contributions to the total LW broadband INLR. The all-sky curve is between the clear and cloudy curves but is not plotted for clarity. b) The difference between the clear-sky and all-sky spectrum's constructed from IASI measurements (black) and estimated far infrared radiances (blue) from predictor wavelengths in the mid infrared with the highest correlations (red dots). The number in parentheses is the fractional contribution of the FIR INLR (FIR CINLR) to the total INLR (CINLR). Data is the area weighted mean of April 2012.

The difference between the averaged clear and all-sky is equivalent to the effect of a cloud and is often know as cloud radiative forcing (CRF) or cloud radiative effect (CRE). Figure 3.12b shows CRF values for the whole LW spectrum, with a total value of 8.1 $Wm^{-2}sr^{-1}$ Note that our definition of CRF is in terms of radiance, not flux. In general there is more outgoing radiation at all wavenumbers in the clear-sky because liquid clouds are nearly opaque to the whole OLR spectrum and re-emit at lower temperatures/energies than the clear-sky case. Wavebands at 0 - 200 cm^{-1}, 650 - 700 cm^{-1} and around 1500 cm^{-1} are strongly sensitive to rotational water vapour transitions, CO_2 ν_2 transitions and the vibrational ν_2 water vapour transitions respectively, and as such peak emissions are in the upper troposphere/lower stratosphere where clouds are few and hence the CRF is low. Even though in the cloudy case the FIR represents a more significant proportion of the total OLR, the clear-sky still emits more over this wavelength range in terms of absolute magnitude. Although the majority energy in cloud radiative forcing are distributed over the atmospheric window spectral interval, the FIR still accounts for 19% of the total CRF.

3.4.3 Maps of INLR, FIR and window wavebands

Spatially, all-sky IASI INLR averaged over the whole month of April 2012 peaks in the clear desert and extra-tropical subsidence regions around $\pm 20\,^{\circ}$. In the latter low maritime clouds emit radiation at high temperatures similar to those at the surface (Figure 3.13a). Deep convective clouds over the intertropical convergence zone, Indo-Pacific warm pool and monsoon regions of Africa and South America reduce INLR because emission is from high, cold cirrus cloud tops. Correspondingly these regions also have the highest CINLR values (Figure 3.13b), as the difference between the all and the clear-sky is at a maximum.

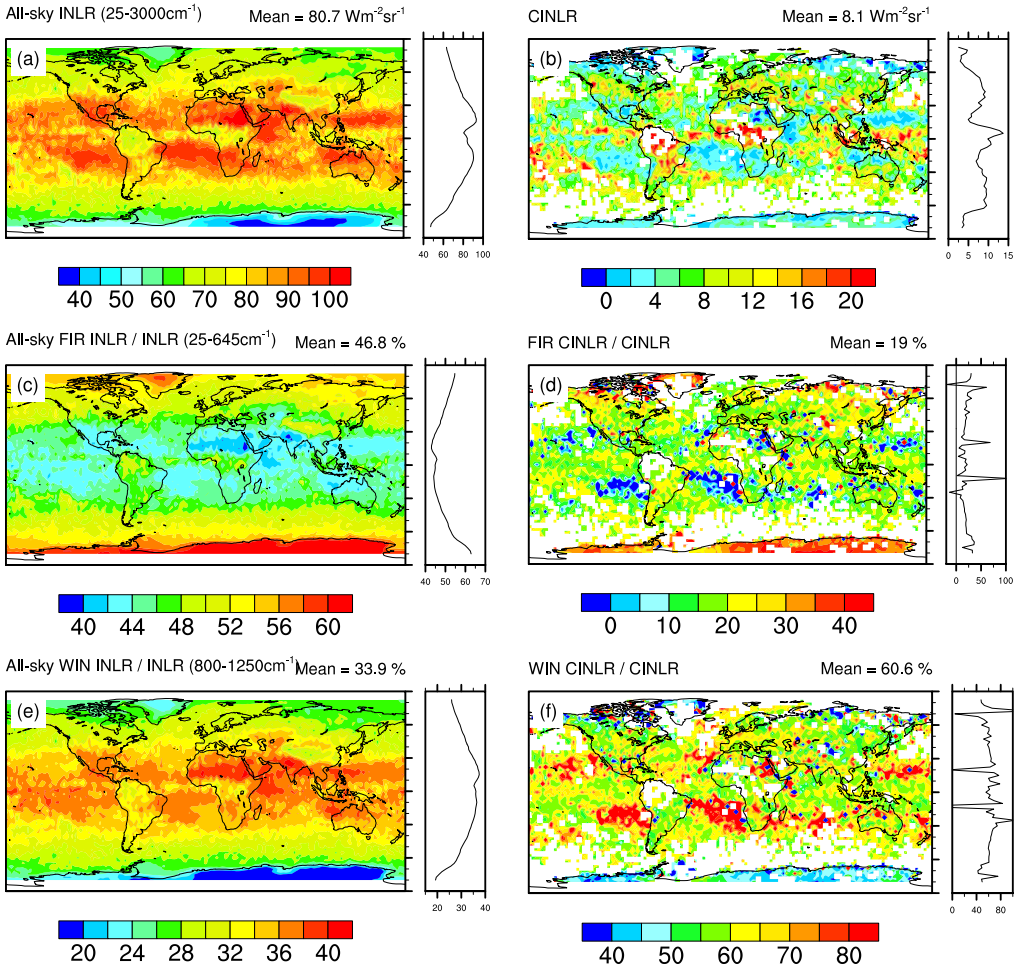

Figure 3.13: INLR and CINLR maps created from all April 2012 pixels binned to a 2.5 by 2.5 grid and averaged. Zonal means are shown to the right of each map. On the left hand side is all-sky: a) INLR, c) FIR as a percentage of INLR, e) the window region as a percentage of INLR. On the right is CINLR (clear-sky - all-sky) for: b) INLR, d) the percentage of CINLR that is FIR, f) the percentage of CINLR that is in the window region. Note that the colour scales are different for every panel. Missing data is shown in white.

An unexpected feature of this plot are occasional negative CINLR values, bordering the polar continents. These values tend not to be lower than -1 $Wm^{-2}sr^{-1}$. CINLR is generally a positive quantity, i.e. if a cold cloud is added to any particular clear-

sky scene instantaneously the radiation emitted from the top of the cloud will be reduced with respect to the clear-sky amount. However, when a lower tropospheric temperature inversion is present, clouds can be warmer than the surface. These clouds are particularly common over the Antarctic Plateau in austral winter as a result of the snow-surface emissivity being greater than the atmospheric emissivity, meaning that the surface will loose energy and cool rapidly whereas the overlying air will retain its heat for longer (Hudson and Brandt, 2005). Additionally cloud detection algorithms often struggle in the polar regions due to lack of thermal contrast between ice covered surfaces and cloud tops. Temperature inversions are also a prominent feature of the subtropical trade wind regimes produced by the subsiding air masses in the descending branches of the Hadley and Ferrel cells. As the mass descends the pressure increases and its volume decreases adiabatically, and hence as the energy is unable to be dissipated as heat its temperature rises warming the air and producing shallow cumulus clouds with a higher temperature than the surface. Examples of this behaviour are visible in the data around $\pm 20\,^{\circ}$ in Figure 3.13b.

The proportion of the radiance spectrum that falls within the FIR waveband peaks in the coldest latitudes of Antarctica as most of the outgoing photons have very low energies and hence low wavenumbers (Figure 3.13c). It is also higher in regions of greater cloud cover, and this can be identified in the deep convective cloud regions with respect to the surrounding clearer areas, such as over the Sahara. The FIR and the window (WIN) waveband between 800 and 1250 cm^{-1} (Figure 3.13e) are inverse to one another in terms of zonal variability, i.e. when the FIR contribution is higher the WIN contribution is lower and vice versa. However, the FIR contributes an average of 40% more to the INLR overall in terms of absolute magnitude. In terms of contribution to the CINLR though, the WIN is 3 times greater on average than the FIR (Figure 3.13d and f), but again the patterns of zonal variability are inverse to each other. Interestingly, in the subtropical subsidence regions there are some negative values of CINLR in the FIR, meaning the average all-sky radiation is more than the average clear-sky at these wavenumbers. As the total INLR and the WIN CINLR are still positive in (most of) these locations these cannot be attributed solely to temperature inversions. It is possible to speculate about the cause of this behaviour, for example, clear skies associated with humid conditions and trade wind inversion clouds associated with dryer conditions would result in a higher emission

level for the FIR. It could also be the case that the FIR is more sensitive to a false diagnosis of a cloudy sky pixel as clear than the whole spectrum overall. As a result of these negative FIR CINLRs, the corresponding positive WIN CINLRs peak at these locations because they are now contributing more to the positive total INLR CINLR. This value is still low due to these two parts of the spectrum cancelling with one another, something that would go un-observed with a purely broadband analysis.

3.5 Conclusions and Discussion

In this chapter we have shown that IASI can be used to simulate the entire range of wavenumbers (25 - 3000 cm^{-1}) needed to estimate the total spectrum of outgoing longwave radiances at a sampling resolution of 0.5 cm^{-1} in the far infrared (<645 cm^{-1}) and the near infrared (>2600 cm^{-1}). The method is based on theoretical correlations between measured and un-measured parts of the spectrum, derived using simulations from the line-by-line radiative transfer code LBLRTM applied to 3200 measured atmospheric profiles. Broadband observations on other satellite platforms place constraints on the total radiant energy which effectively provides a direct comparison of the simulated regions, assuming the parts of the spectrum where CERES overlaps with IASI are fully in agreement, within the bounds of uncertainty introduced by calibration differences and other factors. This uncertainty is quantified at an upper limit of 1.5% for LW CERES radiances, and coincident all-sky measurements between IASI and CERES at simultaneous nadir overpasses in polar regions show mean differences of about 0.3 $Wm^{-2}sr^{-1}$ (0.5% relative difference), which is well within this range. This is a strict test of the regression model, given that the two sets of measurements are completely independent and approximately 50% of the INLR is being estimated.

Instantaneous examples of the simulated spectrum show the far infrared contributes between 43 - 64% to the total INLR with a global weighted average of 47% in the all-sky and 44% in the clear-sky. The results of our comparison are consistent with previous values proposed in the literature (45% for the all-sky, Harries et al. (2008)). This study serves as a proof of concept of the usefulness of IASI for estimating the

terrestrial far infrared at an unprecedented level of spectral resolution. Quantities such as cloud radiative forcing which are commonly studied only as a single integrated quantity across the longwave spectrum contain much more information when examined on a spectral level, and in the absence of any corresponding empirical data in the FIR region this product provides a 'next best' alternative. Application of the reconstructed FIR to studies of cirrus clouds has not been explored here, due to the limited knowledge of the spectroscopy and optical properties of these types of clouds which is inherent in the LBLRTM model. This study strengthens the case for a spaceborne far infrared instrument with which to further validate and develop this model on a spectral level.

It is feasible that this product could be developed by applying angular distribution models to the radiances to give flux estimates using a similar approach taken by previous studies (e.g. Huang et al. (2008)), and as such IASI has the potential to be supplement existing broadband instrument observations. The algorithm as it stands is self-contained for all scene types, however, as anisotropy varies considerably with scene the regression algorithm could be customised to consider cloud cover, surface type and further inhomogeneities. Other inclusions in the construction of the model, such as instrument noise and determination of the optimal spectral interval size for the predictors could additionally refine the models performance further in the future. Given that IASI will eventually be carried by 3 different MetOp satellites in the same local-time orbit, and IASI - New Generation proposed for the second generation of MetOp satellites will have even higher sampling resolution (0.125 cm^{-1}, Crevoisier et al. (2013)), this provides the possibility of a product with valuable length and the ability to be inter-satellite calibrated between instruments.

Chapter 4

IASI OLR Model Evaluation

4.1 Introduction

Outgoing longwave radiation (OLR) resolved at the spectral level is a highly useful quantity because it gives information not only on the underlying climate variables such as clouds, temperature and atmospheric gases, but also contains the fingerprint of long-term climate response (Goody et al., 1998). For example, Harries et al. (2001) examined different parts of the spectra measured by two different orbiting spacecraft 27 years apart in 1970 and 1997 and inferred global changes in five different greenhouse gas concentrations, providing direct experimental evidence for an increase in the greenhouse effect over this time period. The ability of a global climate model (GCM) to reproduce the finer details of the OLR spectrum is a stringent test for a large range of geophysical variables and their vertical distributions, and also calls into question issues surrounding radiative tuning (Turner and Tett, 2013). Although it is possible to simulate the full range of spectrally resolved OLR from GCM output using a line-by-line radiative transfer code such as the Line-By-Line Radiative Transfer Model (LBLRTM) (Clough et al., 1992, 2005), this involves great computational expense for the volume of globally gridded data produced, and evaluation is not something that has been possible in the past due to the lack of corresponding high resolution observations.

The construction of a verified and complete high resolution OLR spectrum from ex-

tended Infrared Atmospheric Sounding Interfermeter (IASI) satellite observations, as detailed in Chapter 3, provides a new opportunity to circumvent these issues. It is important to remember that OLR in this context refers to nadir radiances and not flux. An equivalent model product can be simulated from GCM data using the fast Radiative Transfer model for TOVS 10 (RTTOV-10) which contains IASI as part of its simulation suite. The same process of applying predictors to the satellite measurements (described in section 3.2.2) can be applied to the model simulated radiances, with appropriate modifications, to produce a directly comparable model product.

This approach also has the advantage of allowing the RTTOV-10 code to be tested, by comparing constructed broadband values with those produced by the existing GCM radiation scheme, which separates the errors introduced by the GCM from errors introduced by the different treatments of radiation as outlined in Chapter 1, (Sections 1.3.6.1 and 1.4.4). This is a particularly important step as there have been several recent developments applied to the cloud scheme in RTTOV-10 that require verification. A recent assessment of RTTOV simulations of the IASI instrument has indicated that all-sky radiances show high sensitivity to cloudy inputs (crystal shapes, particle size, and cloud water content) which can reach several kelvin, and the authors conclude that the uncertainties in computed brightness temperatures are above acceptable ranges for data assimilation (Faijan et al., 2012). As modern day data assimilation requires increasingly more and more complex cloud inputs testing this aspect of the code is a vital step.

In Chapter 2, the model was evaluated in 12 narrow wavebands corresponding to the positions of the HIRS longwave channels (listed in table 2.1). An important conclusion drawn was that greater agreement is observed in an equivalent broadband analysis than in the 12 narrow bands sampled by HIRS, with particularly large differences seen in the window (WIN) channels. This suggested a possible cancellation of errors in the region outside of the instruments spectral coverage. This chapter allows this hypothesis to be tested by presenting a comparison of the extended IASI spectrum which not only allows examination of the biases in the gaps between HIRS channels, but also gives unprecedented insight into the far infrared (FIR) region from 25 to 645 cm^{-1}, and the near infrared (NIR) region that extends from 2760 up to

3000 cm^{-1}. This is beyond the coverage of any multi spectral infrared sounder in current space borne operation.

The FIR has been shown on an instantaneous basis to account for up to 65% of the OLR by intensity (Figure 3.9). Given this large proportion it is possible that existing biases in this region of a GCM's radiation code could contribute significantly to the total bias. Huang et al. (2007a) perform a similar hyperspectral evaluation of the GFDL AM2 climate model using convolved AIRS fluxes over the 650 - 1650 cm^{-1} range for ocean scenes to reveal negative biases in the water vapour ν_2 region (around 1533 cm^{-1}), speculating further negative biases in the FIR region to compensate for more prominent positive biases in the window region. In a separate study, the authors estimate fluxes for the uncovered bands below 400 cm^{-1} and above 1400 cm^{-1} for the clear-sky tropical oceans and the results corroborate this hypothesis (Huang et al., 2006). The 3 longwave HIRS channels that are sensitive to water vapour (channels 10,11 and 12) all display positive anomalies for HadGEM2 simulated brightness temperatures, hence negative biases, if they exist, must originate from other spectral regions. As the ν_2 vibrational bending mode of water vapour extends from 1200 - 2200 cm^{-1} and the ν_3 asymmetric stretching mode is from 2600 - 3000 cm^{-1}, behaviour in these regions is yet to be seen fully, and hence this analysis is highly instructive in revealing heretofore unknown biases for the HadGEM2 GCM.

The FIR wavenumbers below 645 cm^{-1} in the IASI OLR product were constructed via a regression technique that associates each line in the FIR with a line in the IASI wavenumber domain that displays a maximum correlation with it. These correlation coefficients are in excess of 0.99 (Figure 3.4) and the resulting radiances are verified via the results presented in Section 3.3.1. These comparisons infer that the constructed region is an accurate 'proxy' for the FIR, and as such can be used to investigate atmospheric constituents that influence it. This region is dominated by the rotational band transitions of water vapour, so for clear-sky data the representation of this type of low energy absorption in the model can be isolated. In the all-sky the FIR contains detailed information about the spectral signature of cirrus clouds. Yang et al. (2003) perform a modelling study that shows when a cloud is either optically thin, or optically thick, the 800 - 1250 cm^{-1} mid infrared range is sensitive to small ice particles, however, much greater sensitivity is observed in the FIR region, at times reaching a factor of 10 more. Because of the strong absorption

by lower tropospheric water vapour in the FIR, the surface and lower atmosphere are opaque to radiation below 400 cm^{-1}, and as water vapour concentrations at these levels are far reduced this isolates the upper tropospheric ice cloud signal (Kratz, 2002).

It is known that the inhomogeneous nature of ice clouds, which have to be streamlined in climate models, contribute to their poor representation (Jiang et al., 2012; Waliser et al., 2009). Additionally, the interaction between radiation and ice particles is complex and highly sensitive to the individual form of ice (Kristjánsson et al., 2000), hence the simulation of ice cloud-radiative effects in GCMs has multiple layers of difficulty (Liou, 1986). The existence of 'dirty windows' in the FIR, where weak absorption at certain wavelengths renders the atmosphere more transparent (Rathke et al., 2002), provides vertically resolved information on the quality of ice cloud parametrisation within the GCM, not necessarily visible in the mid infrared region. It has already been inferred using the window region in the HIRS analysis (Section 2.3.4.2) that clouds are too low throughout the models atmospheric column, and the addition of a resolved FIR provides the potential for more thorough insights on the cloud types contributing to this bias.

4.2 Data and Methodology

4.2.1 HadGEM2-A

The HadGEM2-A climate model dataset for 2009 is the same as that used in Chapter 2, Section 2.2.1 for the HIRS evaluation. As both the HIRS and IASI instruments fly onboard MetOp-A the same satellite time sampling methodology as detailed in section 2.2.7.2 is applied to IASI simulations. Following the findings based on model choices presented in Section 2.3.1, instantaneous output obtained at 15 hour intervals is first processed through the RTTOV satellite simulator and the resulting radiances/brightness temperatures are composited into a single month. As a 40% cloud fraction threshold was found to be sufficient for approximating clear-sky pixels this threshold is reused in the present study, however, given the sensitivity of the water vapour bands to this threshold as reported in section 2.3.1, it is important to

be aware of possible errors relating to this choice when examining clear-sky model biases at wavenumbers affected by water vapour transitions.

4.2.2 RTTOV-10

Climate model data is run offline through the RTTOV-10 radiative transfer code, in the same manner as in Section 2.2.6, but simulating the IASI instrument. The same cloud partitioning methodology applied to the HIRS simulation is used, as shown in the process diagram in Figure 2.1. All 8461 of the instruments channels are simulated for every gridpoint in the time reduced satellite sampled dataset and the coefficients used to calculate wavenumbers uncovered by the IASI instrument (see Section 3.2.2) are applied to the appropriate output radiances. For every file of simulated mid infrared radiances obtained, 2 separate files of predicted radiances are produced for both the far infrared (1240 channels) and the near infrared (480 channels). Finally these 3 files are concatenated to yield the complete simulated OLR spectrum from 25 - 3000 cm^{-1} (10181 channels).

4.2.3 IASI OLR

Full details of the IASI instrument onboard the MetOp-A satellite are given in Chapter 3 Section 3.2.1. Following the same methodology observations are filtered for the 4 most nadir looking views, and pixels flagged as clear are used to construct an equivalent clear-sky product. The percentage of pixels identified as clear varies between 12 and 20% for a single orbital file. In order to make the comparison with climate model data consistent, the order of applying predictor coefficients and gridding the satellite data is reversed compared with the method used to construct the monthly composite in Section 3.3.2. To explain, as each climate model file yields only 1 simulated radiance at every gridpoint, it must be assumed that it is the average result for the entire gridbox, therefore, to make the satellite product comparable all measurements that fall in the same gridbox over a similar time period must be averaged. The time period for climate model output is every 15 hours which results in either 1 or 2 outputs on any given day, hence it is appropriate to average the satellite radiances on a daily basis. This results in approximately 10 daily observations per equatorial gridbox reducing to about 2 or 3 per polar gridbox, however more of the

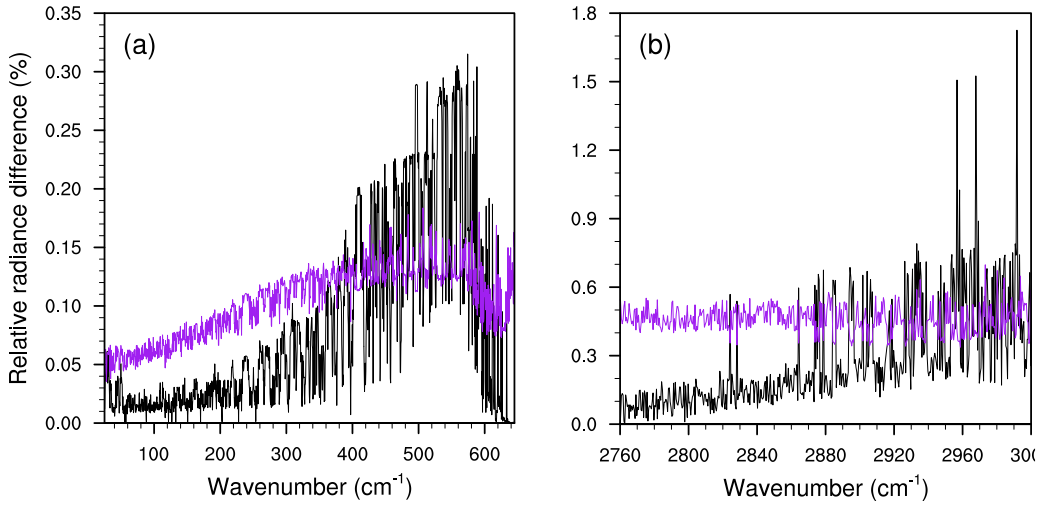

Figure 4.1: Global mean relative radiance differences between averaging processes for a) the FIR, and b) the NIR, for the composite of all IASI measurements taken in January and July 2009. The order of differencing is predictor coefficients applied first then averaged (standard method), minus averaging first then applying the predictor coefficients (model evaluation method). This difference is then divided by the radiances produced using the standard method to give the relative difference. The black lines are all-sky and the purple lines are clear-sky.

polar gridboxes are filled over a single day. Predictor co-efficients are then applied to these results to produce the extended OLR spectrum. As the prediction equation (equation 3.1) uses a log transform the operation is non-linear and the order of averaging has an impact on the results. Global mean relative differences between radiances obtained using both processes are shown in Figure 4.1 for the parts of the spectrum that are estimated using the algorithm. Relative differences barely exceed 0.3% for the FIR, with the NIR showing some slightly higher spikes of up to 1.8% at upper values, however the very low radiances at these wavenumbers are a contributing factor. Overall these differences are much lower than the biases expected to be seen in the model to satellite comparison based on the results yielded in the HIRS analysis and this averaging process is not expected to impact results significantly.

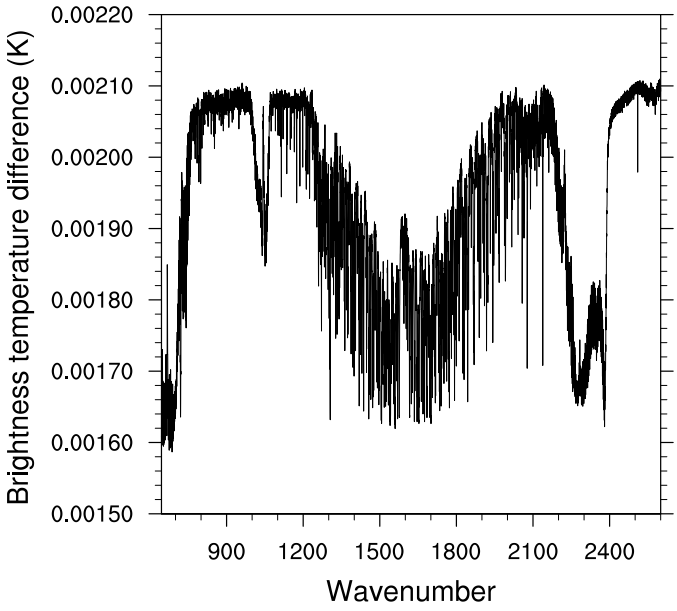

Figure 4.2: Global mean brightness temperature differences between the offline processing of the Planck equation on simulated radiances and direct RTTOV-10 output for the composite of all IASI measurements taken in January 2009.

4.2.4 IASI Brightness Temperatures

As demonstrated in Chapter 2, brightness temperature is a useful way to present radiance in order to interpret the level of emission with a temperature-like quantity. The satellite data obtained for IASI does not include brightness temperature variables, but owing to the high spectral sampling interval (0.25 cm^{-1}) and high resolution (0.5 cm^{-1} FWHM) of the IASI instrument each channel can effectively be thought of as monochromatic. This allows IASI brightness temperatures to be accurately calculated by inversion of the Planck equation to the form given in equation 1.6. Note that this is in contrast to the HIRS instrument where the width of each channel spans several wavenumbers and a 'band correction' must be applied to the brightness temperature conversion to account for the irregular spectral response function.

Equation 1.6 is applied to every wavenumber in the extended OLR spectrum of the satellite data to obtain the equivalent brightness temperatures. RTTOV calculates brightness temperatures from radiances so in order to verify that it produces the

same result as the equation applied to satellite data, the RTTOV calculated brightness temperatures for all IASI channels are obtained, and compared with brightness temperatures produced by applying equation 1.6 to RTTOV radiances offline. Differences are below 0.0021 K for all wavenumbers considered, which is less than a 0.001% relative error even on the lowest brightness temperatures found over the globe, and which is possibly due to rounding errors (Figure 4.2). To be consistent with the method used in the observations, the offline method of calculating brightness temperatures is used on radiances produced by RTTOV-10.

4.2.5 Radiance to Flux Estimation

In order to compare spectral radiance biases with equivalent broadband results, such as those presented in Chapter 2, Section 2.3.3, it is useful to make an estimate of the directionally integrated OLR fluxes, measured in Wm^{-2}, from the nadir viewing OLR radiance product, measured in $\mathrm{Wm}^{-2}\mathrm{sr}^{-1}$. Fluxes are calculated in HadGEM2 using a two-stream approximation, where the angular variation of the radiance field is represented by an upwards and downwards diffuse flux (full details given in Section 1.3.6.1). Directionally dependent radiation is not calculated explicitly in the GCM, hence it is necessary to approximate the angular variation of the simulated IASI OLR product to calculate the equivalent flux. The quantity that describes this is called an anisotropic factor which is a value close to 1 that describes how much the flux $F_j(\theta_0)$ differs from an isotropic radiance field given by equation 1.7. The set of anisotropic factors that determine the TOA flux are given by a function called an Angular Distribution Model (ADM). The variation for an instantaneous measurement of radiance $I_j(\theta_0, \theta, \phi)$, for a given scene type j, is the set of anisotropic factors $R_j(\theta_0, \theta, \phi)$ which is calculated by:

$$R_j(\theta_0, \theta, \phi) = \frac{\pi I_j(\theta_0, \theta, \phi)}{F_j(\theta_0)} \tag{4.1}$$

R depends on solar zenith angle θ_0, viewing zenith angle θ, and viewing azimuth angle ϕ (see Figure 1.1 for a schematic of these).

Angular distribution models are predetermined, even for satellite measurements, because instruments only measure radiances in certain viewing directions (Kato and

Loeb, 2005). ADMs vary with the properties of the scene in question with strong sensitivities to the following; cloud fraction, cloud height, cloud optical depth, cloud phase, precipitable water, aerosol optical depth, surface skin temperature and surface type. Previous studies have shown that ignoring the scene type results in significant errors in the calculated flux (Loeb et al., 2000). For longwave measurements the dependence of R_j on solar zenith angle and viewing azimuth angle is negligible, apart from a weak azimuthal dependency in clear land conditions. As the viewing zenith angle for both observations and climate model data are constant at near zero degrees, anisotropic factors are considered to be purely a function of scene type in this study.

Loeb et al. (2003) estimate broadband ADMs using an empirical approach, whereas Huang et al. (2008) derive ADMs that are spectrally dependent. In order to estimate the spatial variability of anisotropy using broadband data an empirical approach based on coincident measurements from instruments onboard the same satellite is applied in order to calculate mean anisotropic factors for globally gridded scenes. These factors can then be used with gridded model data. Equation 4.1 is applied to instantaneous IASI OLR radiances and HIRS OLR fluxes at points where the footprints of both instruments overlap. The HIRS OLR product is described in section 2.2.4 and uses a regression algorithm to calculate fluxes from radiances measured in 4 of the HIRS longwave channels. The error in the regression process is a function of viewing zenith angle and for nadir views is about 3.5 Wm^{-2} (Hai-Tien Lee, Personal Communication 2014), the corresponding error in the IASI OLR product was estimated at approximately 1 $\mathrm{Wm}^{-2}\mathrm{sr}^{-1}$ in Chapter 3, Section 3.3.2.

The collocation criteria chosen requires that the centre of both pixels are within 6 km of each other, when the times of both instruments swaths are closest. Given the diameter of the nadir field of view for the HIRS instrument is 10 km, and the equivalent for IASI is 12 km, this ensures at least half of the footprint overlaps. This results in up to 2500 collocated points being identified in a single day. Instantaneous anisotropic factors from the whole of 2009 are gridded to the same resolution as the climate model (1.25 ° latitude x 1.875 ° longitude) and averaged. Finally, these factors are applied to model simulated IASI OLR radiances by inverting equation 4.1 to calculate the IASI flux. As anisotropic factors are strongly scene specific the averaging process will almost certainly introduce some errors into the results which

are difficult to estimate, however seeing as all climate models produces quantities that are gridbox averages this approach is not inconsistent, and serves to give a best estimate of the global spatial variability of R_j .

4.3 Results

4.3.1 Radiances

Model radiances simulated using the method described in Section 4.2.2 are presented in this section along with their biases. These are shown spectrally and additionally as integrated quantities across all wavenumbers to give spatial and seasonal OLR biases.

4.3.1.1 Spectral comparison

The top part of Figure 4.3 presents the complete all-sky OLR spectrum simulated by HadGEM2-A via RTTOV-10, which has an annual global mean broadband radiance of 85.61 $Wm^{-2}sr^{-1}$. The red lines displaying Planck functions give an indication of the temperature of the level of emission of the received radiation at each wavenumber. The common features of OLR curves are outlined in Chapter 1, Section 1.1.4. The bottom part of Figure 4.3 shows the cloud radiative forcing (Equation 1.6) and equates to a total broadband value of 4.24 $Wm^{-2}sr^{1}$. The effect of clouds on the spectrum is seen most in the window band which contributes 57.4% of the total OLR CRF, and is due to the clouds perturbing radiation all the way down to the surface. The FIR contributes a fraction less than half this amount (21.8%), due to the opacity of the lower troposphere elevating the level of emission where only the tops of clouds can have an effect.

The difference between these modelled and observational spectra are shown in Figure 4.4a for the all-sky. There is an overestimation of radiance at nearly all wavenumbers with a total integrated bias of 4.52 $Wm^{-2}sr^{-1}$ (5.6% of the OLR), the majority of which (two thirds) originates from the window region, with the FIR contributing around a fifth of the total. Low biases are seen in regions where radiation is emitted

from high in the troposphere and stratosphere, such as the CO_2 band from 600 - 700 cm^{-1}. By virtue of the high level of emission this band is rarely affected by clouds. The clear-sky equivalent (4.4b) shows a much reduced bias of 0.39 $Wm^{-2}sr^{-1}$ and individual wavenumber errors in both the FIR and the WIN regions are small, rarely exceeding 0.0020 $Wm^{-2}sr^{-1}$ in magnitude whereas all-sky biases in the window region reach as high as 0.0090 $Wm^{-2}sr^{-1}$.

In the all-sky, there is no appreciable compensation between one spectral band and another, which is surprising given the size of the biases in the window region. One would expect to see biases of opposite sign bringing the overall integrated value down. The isolation of the cloud effects in Figure 4.4c strongly suggests that these biases are dominated by cloud errors because the magnitude of the bias is nearly equal to that in Figure 4.4a and the shape is a near reflection of it. This is further corroborated by the reduced biases in the FIR region which is sensitive to only upper clouds, whereas the window channel has the potential to sense the clouds throughout the whole atmospheric column. The cloud radiative forcing is underestimated by 4.13 $Wm^{-2}sr^{-1}$, which equates to 50% less than the observational CRF (8.35 $Wm^{-2}sr^{-1}$) and is a significant difference. Only 16% of this bias, however, is coming from the FIR region, with over 50% originating from the WIN. This region is measured directly by IASI so is not subject to uncertainties associated with the method of estimating the FIR.

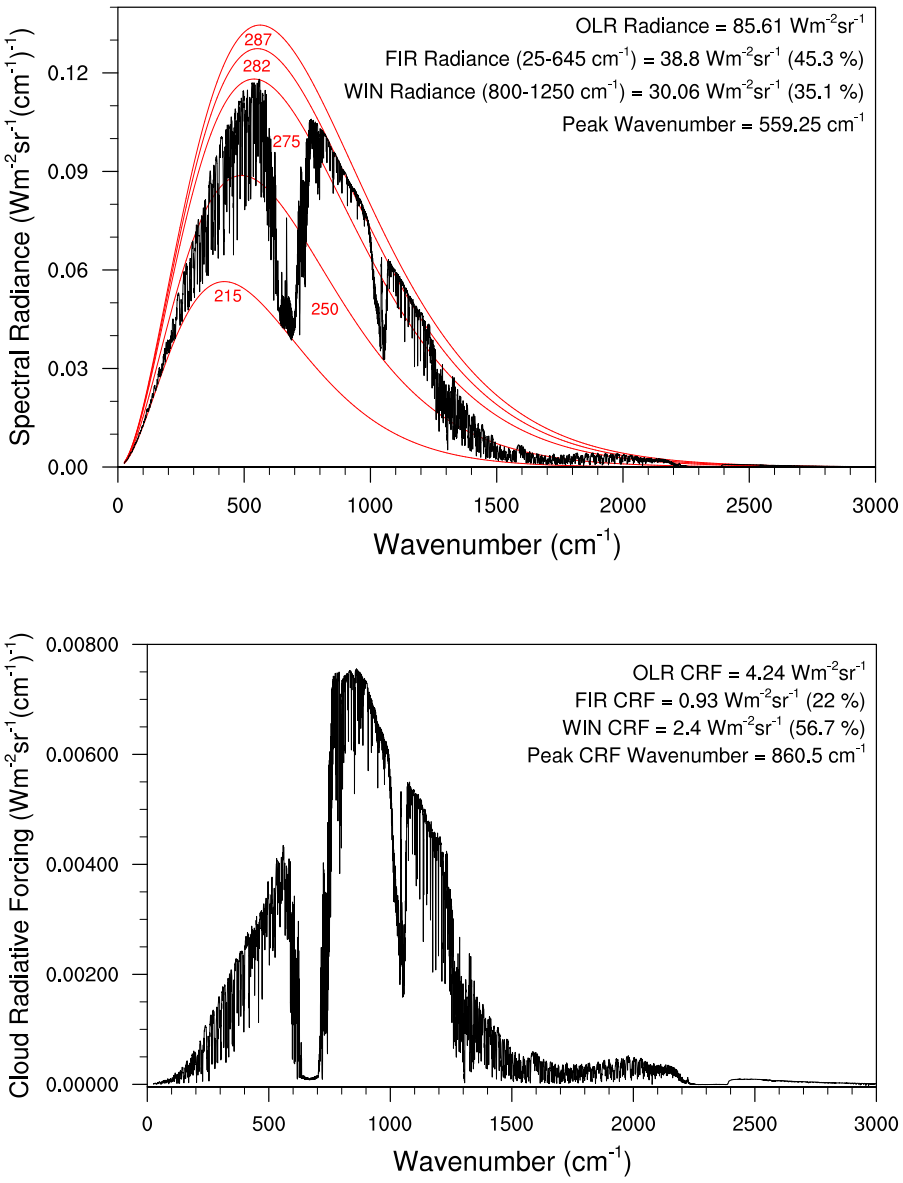

Figure 4.3: Top: All-sky OLR spectrum for the HadGEM2-A climate model for the all-sky. Data is time sampled to the MetOp-A satellite orbit. Figures in brackets are the percentage contributions of the FIR and the WIN regions to the total OLR. Red lines show the equivalent blackbody spectra at the given temperatures measured in Kelvin. (This figure is the model equivalent of Figure 1.2) Bottom: Cloud radiative forcing spectrum for HadGEM2-A climate model data simulated by RTTOV-10. Figures in brackets are the percentage contribution to the total OLR CRF by the FIR and the WIN respectively. Both plots are the 2009 annual global mean.

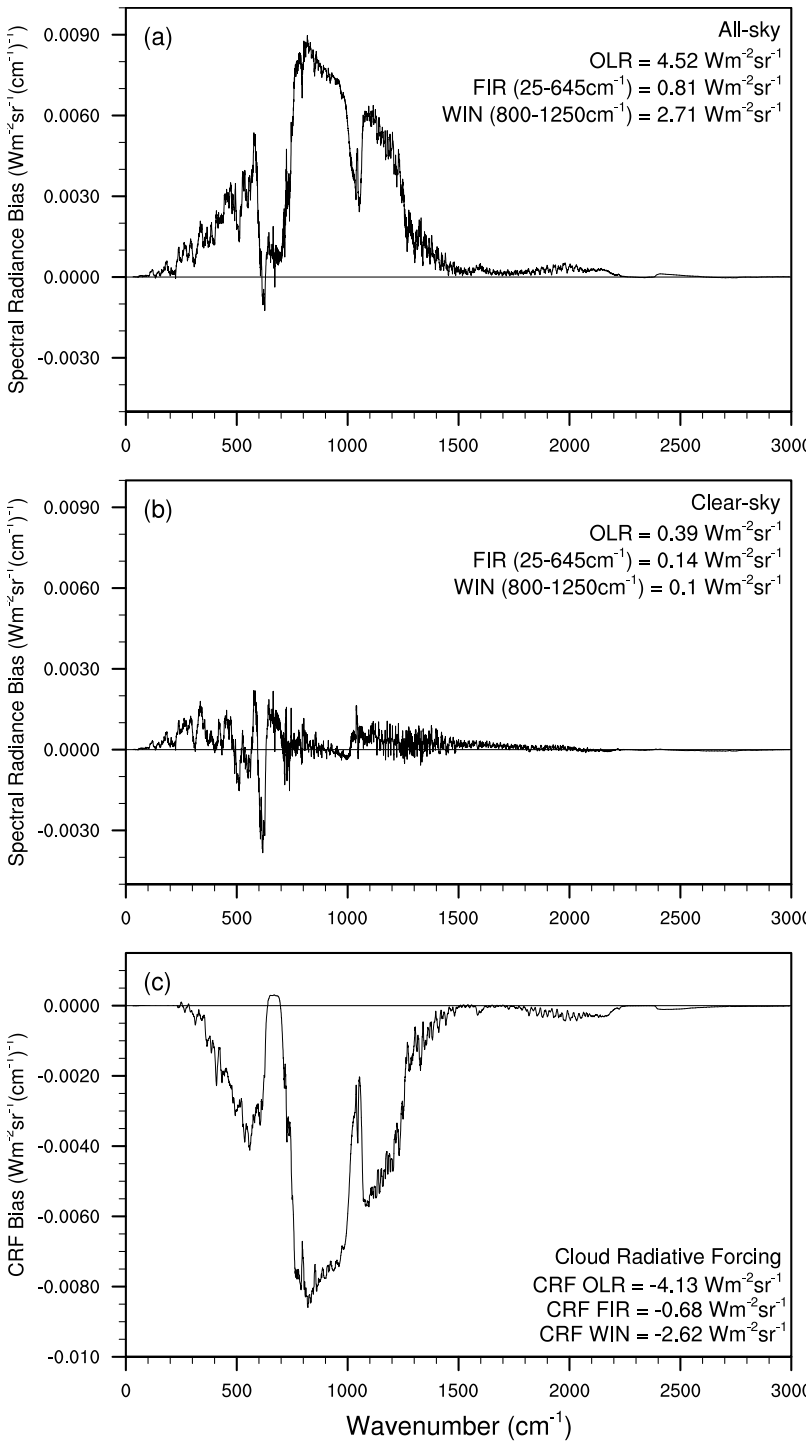

Figure 4.4: 2009 annual global mean radiance biases for a) all-sky radiances, b) clear-sky radiances, and c) cloud radiative forcing. A 30 member running average has been applied to the curves. Note a) and b) have a different ordinate scale to c)

Table 4.1: 2009 annual global mean biases (model - observations) of the OLR spectrum integrated over each band used in the Edward-Slingo radiation code used in HadGEM2-A. Units are $Wm^{-2}sr^{-1}$.

Band (cm^{-1})	Sensitivity	All-sky	Clear-sky
0-400	H_2O rotational	0.21	0.15
400-550	H_2O rotational 'window'	0.39	0.03
550-800	H_2O CO_2 window	0.77	0.04
800-880	window	0.66	0.01
880-990	window	0.80	-0.01
990-1120	O_3	0.64	0.05
1120-1200	window	0.41	0.03
1200-1500	H_2O vibrational ν_2 CH_4 N_20	0.45	0.06
1500-3000	H_2O ν_2 ν_3 CO_2	0.18	0.04
0-3000		**4.52**	**0.39**

The ES radiation code associated with HadGEM2 computes fluxes in 9 consecutive wavebands in the longwave, the division of which is related to different absorbing mediums in each band which were initially chosen to study the global warming due to CO_2 and other greenhouse gases. To investigate errors associated with these predefined divisions that are sensitive to different atmospheric components the total bias in each of these wavebands is shown in Table 4.1. There are positive biases in all of the all-sky bands, the largest of which are found in the 4 bands between 550 and 1120 cm^{-1}. The first of these ranges from 550 to 800 cm^{-1} and is rather broad, covering the latter part of the far infrared up to about 650 cm^{-1}, the CO_2 ν_2 band, and a substantial contribution from the surface from about 750 cm^{-1}. Hence the large bias of 0.77 $Wm^{-2}sr^{-1}$ is mostly the result of a strong positive bias in the window region, whereas as seen in Figure 4.4a the CO_2 band between 650 and 750 cm^{-1} contributes very little bias. In the clear-sky, biases in all 9 bands are much smaller. The highest contributing bias is found in the 0 to 400 cm^{-1} strongly absorbing FIR region which suggests that water vapour is possibly underestimated slightly in the very upper troposphere.

There are small seasonal cycles visible in the global mean radiance biases (Figure 4.5). For the all-sky the range is 0.76 $Wm^{-2}sr^{-1}$, with a peak of nearly 5 $Wm^{-2}sr^{-1}$ in June and just over 4 $Wm^{-2}sr^{-1}$ in February, which is small compared to the absolute biases. The range of the cycle is slightly greater in the clear-sky with a range of 0.97

$Wm^{-2}sr^{-1}$, however, as the absolute biases reach a maximum of 0.81 $Wm^{-2}sr^{-1}$ this is more significant. As discussed in Chapter 2, Section 2.3.2 with reference to Figure 2.7, this fluctuation is likely to be due to the model land surface temperatures not being prescribed and hence more uncertain than applied SSTs. Land experiences more of a seasonal cycle than ocean so it appears that clear-sky errors are proportional to seasonal variables such as higher temperatures in Northern Hemispheric summer.

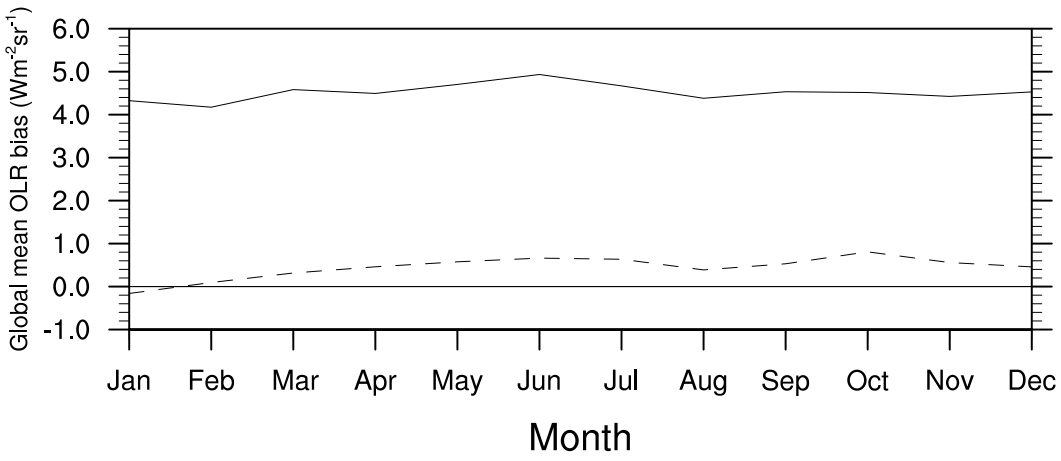

Figure 4.5: Global mean radiance biases by month for all-sky radiances (solid line) and clear-sky radiances (dashed line) for 2009.

4.3.1.2 Maps of biases

Figure 4.6 shows the spatial distribution of biases for integrated bands over the total OLR spectrum, the constructed FIR region, and the mid infrared WIN region. The pattern of biases in the all-sky OLR are strongest over areas of deep convective activity and remain positive over the majority of the globe, with negative biases only appearing in regions where low subsidence clouds prevail. Individual errors can be as much as twice the global mean in these regions. The clear-sky equivalent bias is much lower due to a cancellation of spatial positive and negative biases. The more prominent land biases mentioned in the last paragraph are evident and particularly defined in the window band (4.6f), where there is a general trend of too little radiation

emitted over land scenes which is balanced by a widespread overestimation of emitted radiation over the ocean. Comparing 4.6e with 4.6a shows that most of the positive pattern of all-sky OLR biases are coming from the window region with additional equatorial biases originating in the FIR region (4.6c), indicating that the very tops of clouds contribute to this error. The FIR also seems to be a source of negative bias in the subsidence regions. The clear-sky equivalents show low FIR biases that cancel zonally to near zero, whereas the WIN region shows an obvious pattern of biases over land regions which is indicative of discrepancies in land temperatures, likely due to land surface temperatures not being prescribed.

4.3.2 Brightness Temperatures

As discussed in Section 1.1.6 the equivalent radiance unit of brightness temperature is a useful way to visualise TOA radiation. This is particularly informative when examining wavenumbers with low radiant intensities but high brightness temperatures, such as those beyond 1500 cm^{-1}. This measure of radiance also allows comparisons to be made with results obtained from the HIRS evaluation in Chapter 2. The spectrum of longwave brightness temperatures and their biases are presented in this section.

4.3.2.1 Spectral comparison

Figure 4.7 presents the complete simulated infrared spectrum of brightness temperatures. There is a difference of approximately 6K between the all and the clear-sky in the window bands between 800 and 1250 cm^{-1}, and 2400 - 3000 cm^{-1} which, owing to the lack of absorbing mediums at these wavenumbers, corresponds to the average temperature difference between the surface and cloud tops. Note that this neglects the water vapour continuum which decreases outgoing radiation in the clear-sky. Also high level ice clouds with low emissivity values will not show up significantly in the all-sky as they are semi-transparent.

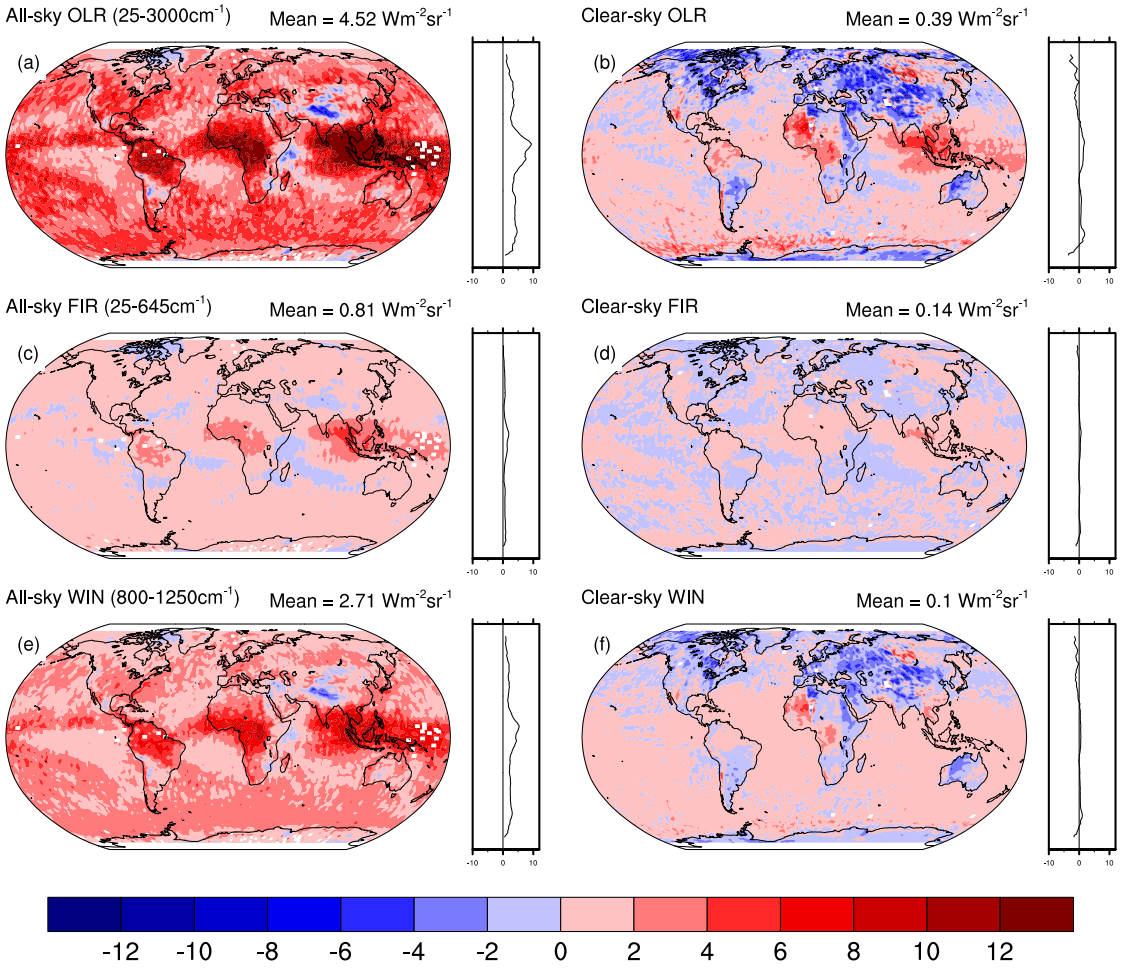

Figure 4.6: 2009 annual mean radiance biases, spectrally integrated for a) all-sky OLR, b) clear-sky OLR, c) all-sky FIR, d) clear-sky FIR, e) all-sky WIN, and f) clear-sky WIN. Zonal means are shown to the right and area weighted global means are given at the top right of each plot. Units are $Wm^{-2}sr^{-1}$.

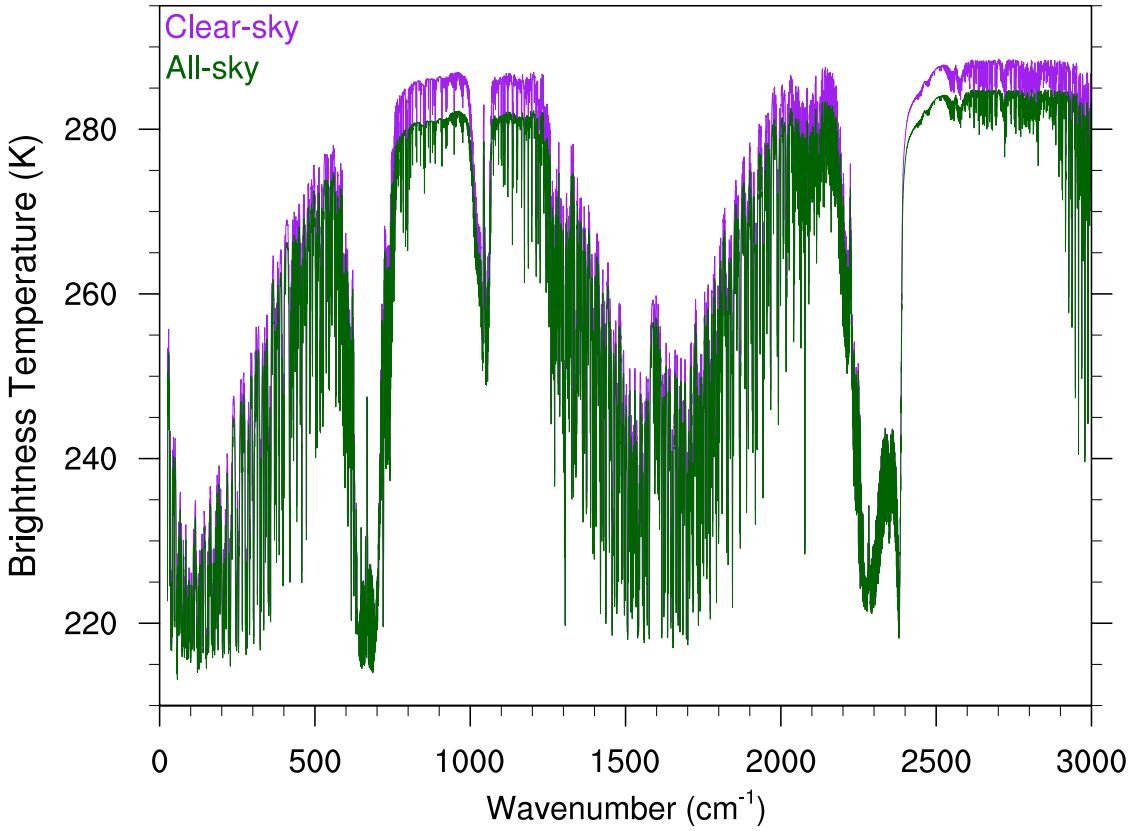

Figure 4.7: 2009 annual mean brightness temperature spectrum for the HadGEM2-A climate model data simulated by RTTOV-10 for the all-sky (green line) and the clear-sky (purple line). Units are K.

The biases between these spectra and equivalent observations (Figure 4.8) closely match the biases calculated in Chapter 2 (see Figures 2.6 and 2.7) at wavenumbers corresponding to the positions of the HIRS channels (marked in red). This verifies that measurements from the HIRS and IASI instruments are consistent with one another. The FIR biases are of comparable size to the biases around the water vapour vibrational ν_2 band (centred at 1533 cm^{-1}), and as the majority of the predictor radiances used to construct the FIR are found in this region it is consistent that they are positively correlated with each other. As the FIR level of emission is above the water vapour distribution where temperatures are mostly below freezing the difference between all and clear-sky biases isolates the misrepresentation of ice clouds, which is up to 3K. This is approximately half the 6K bias difference seen in

the window region which includes mid and low level clouds as well.

The only prominent negative biases in the brightness temperatures appear at around 2300 cm^{-1} and 2700 cm^{-1}, which are affected by CO_2 and methane (CH_4) respectively. The size of these biases are somewhat misleading and arise mostly because radiances at these wavenumbers are so low that small differences are emphasised by the application of the inverse Planck equation (Equation 1.13) to calculate brightness temperatures from radiances. Additionally trace gases such as CH_4 and N_2O with sensitivity in this region are not variable in RTTOV-10. This suggests limited conclusions can be drawn from examining the NIR part of the spectrum simulated in this manner. Apart from these regions, and as with the spectral radiance comparison, there are no appreciable negative biases in the all-sky part of the spectrum, in contrast with the original hypothesis, giving a high overall bias. Verifying this seeming inconsistency with the broadband analysis is the subject of the next section.

4.3.3 Flux Comparison

For all-sky data the total mean global OLR bias is 4.52 $Wm^{-2}sr^{-1}$, whereas the broadband flux bias presented in section 2.3.3 using fluxes taken directly from the climate models radiation scheme, evaluated against HIRS OLR on MetOp-A is 2.86 Wm^{-2} (Figure 2.8a), and 2.27 Wm^{-2} when evaluated against CERES EBAF fluxes (Figure 2.8c). The former is more appropriate to use because the diurnal sampling of the CERES data is different to that of IASI as both of the CERES instruments that make up the EBAF product fly on satellites with different equatorial crossing times to MetOp-A.

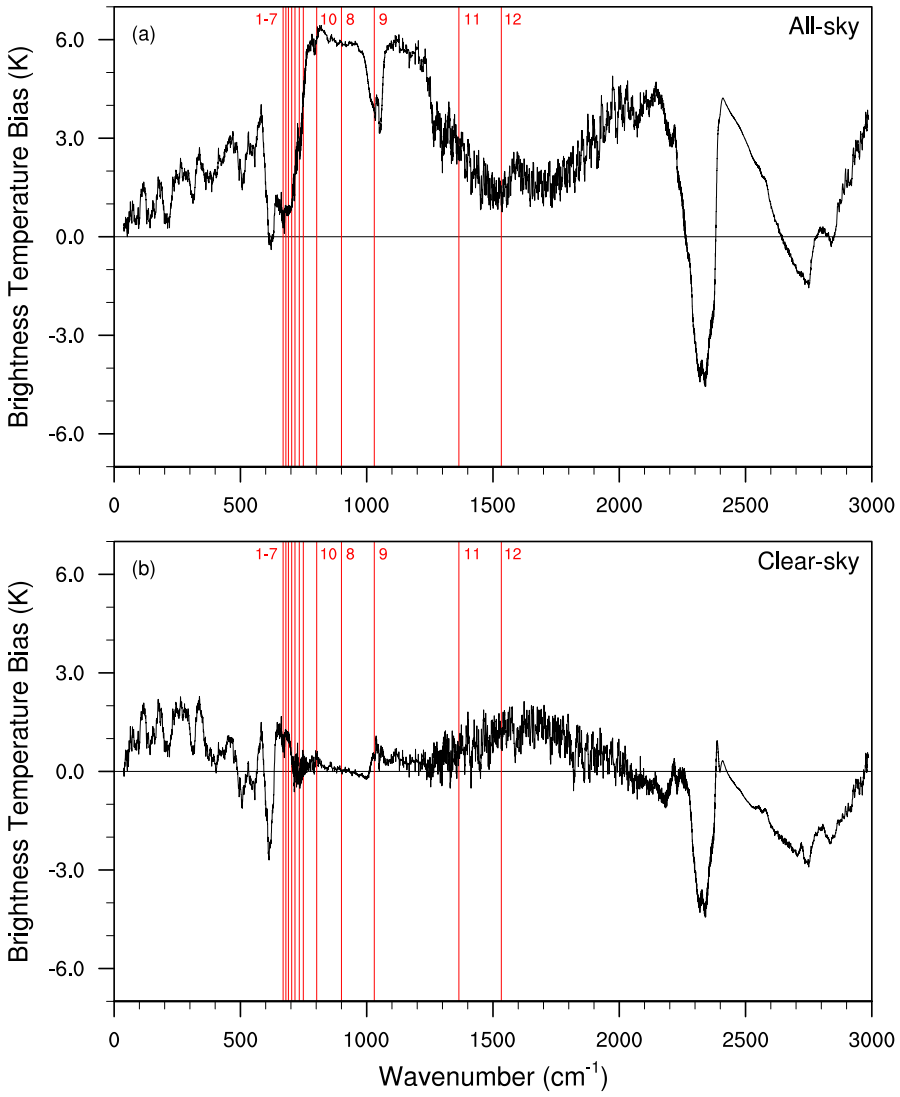

Figure 4.8: 2009 annual global mean brightness temperature biases (model - observations) for a) all-sky and b) clear-sky. A 50 member running average has been applied. Numbered red lines indicate the positions of the HIRS longwave channels.

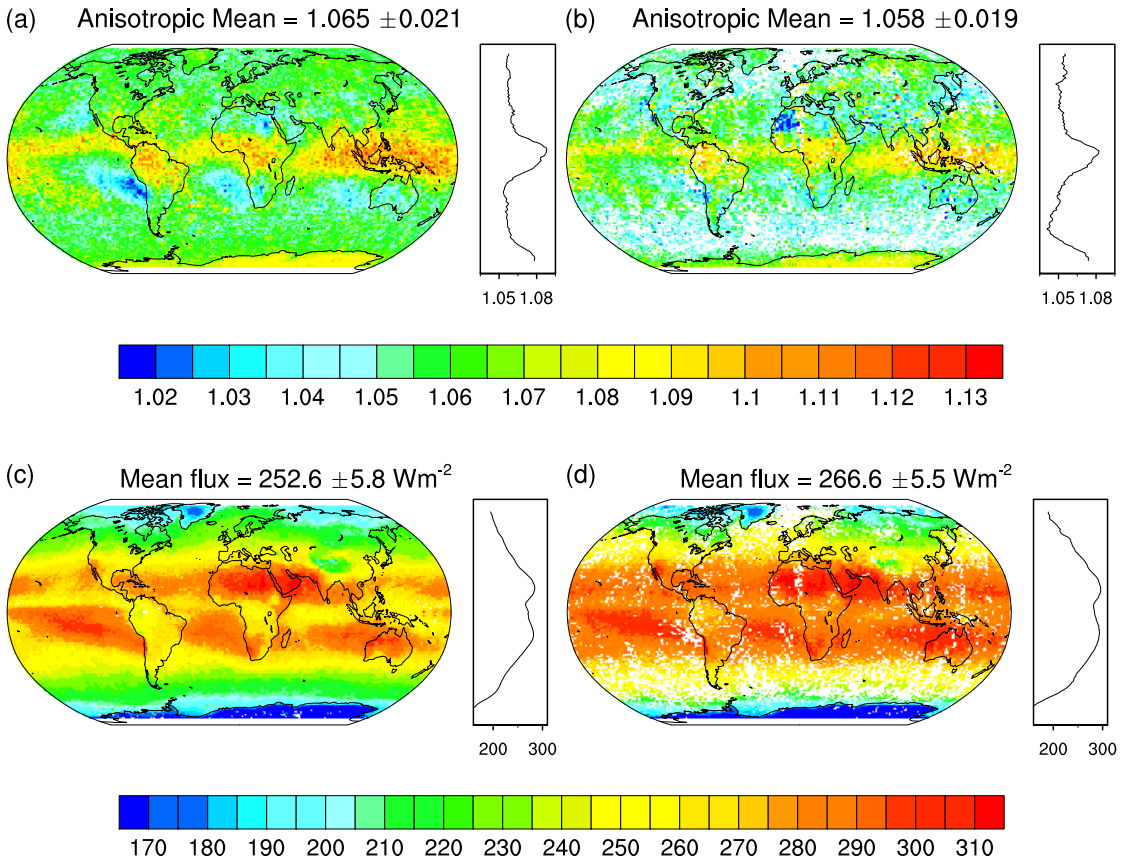

Figure 4.9: a) All-sky and b) clear-sky mean gridded anisotropic factors calculated from collocated IASI OLR integrated radiances and HIRS OLR fluxes. Units are dimensionless. c) All-sky and d) clear-sky model simulated IASI OLR fluxes calculated using these gridded anisotropic factors. Units are Wm^{-2}. All maps comprise the mean of 2009, with zonal averages shown to the right.

As a first approximation of the flux bias from the IASI OLR product, an assumption of isotropy (Equation 1.7) applied to the bias values calculated in Figure 4.4 gives a model flux that is 14.20 Wm^{-2} greater than observations. However, the equivalent clear-sky flux is estimated at 1.23 Wm^{-2} which is approximately consistent with the broadband clear-sky flux bias of 0.79 Wm^{-2} evaluated using CERES (Figure 2.9d), allowing for the aforementioned discrepancies from diurnal sampling differences. As spatial anisotropy is heavily dependent on scene type and is particularly affected by the presence of clouds, the assumption of isotropy is not appropriate. Gridded and averaged anisotropic factors for the whole of 2009, empirically derived using the

collocation methodology described in section 4.2.5 are shown in Figure 4.9. Most scenes display an average value of 1.06 however larger values of up to 1.13 are present in regions of deep convective cloud, and values as low as 0.95 are found in the subtropical subsidence regions. Clear-sky anisotropic factors are slightly lower overall. The RMS error due to the uncertainties in both the IASI OLR and HIRS flux quantities is 0.02. Applying these gridded mean values to simulated IASI OLR data by inverting equation 4.1 yields an estimate of model IASI fluxes with their associated averaged RMS errors (Figure 4.9c and d).

Biases between the new flux product and HIRS OLR observations still remain large in the all-sky at 12.57 Wm^{-2} (Figure 4.10a) which is not dissimilar from the value given by the isotropic assumption, indicating the effect of anisotropy is only around 1.63 Wm^{-2} in the all-sky. The difference between these fluxes and the flux calculated by the ES radiation code is presented in Figure 4.10c and d. These results are independent of the bias introduced by climate model errors because both radiative transfer codes are operating on the same underlying data, hence provide a way of isolating their performance. The difference between them is significantly large in the all-sky at 9.83 Wm^{-2}. The errors in the model flux estimate for each scene, or in the model case, gridpoint, j, are estimated from the uncertainty in the construction of the IASI INLR product, $\Delta I_{mod,j}$ (1 $\mathrm{Wm}^{-2}\mathrm{sr}^{-1}$, Chapter 3, Section 3.3.2), and the global distribution of uncertainties in the empirically estimated anisotropic factors, ΔR_j. These are themselves subject to the uncertainty in the IASI INLR estimate, ΔI_j, which is still 1 $\mathrm{Wm}^{-2}\mathrm{sr}^{-1}$ and that of the HIRS OLR product, $F_{HIRS,j}$ (3.5 Wm^{-2}, section 4.2.5). The model estimated flux error, ΔF_j, is given by:

$$\Delta F_j = F_j \times \sqrt{\left(\frac{\Delta I_{mod,j}}{I_{mod,j}}\right)^2 + \left(\frac{\Delta R_j}{R_j}\right)^2} \tag{4.2}$$

where $\Delta I_{mod,j}$ is 1 and ΔR_j is given by:

$$\Delta R_j = R_j \times \sqrt{\left(\frac{\Delta I_j}{I_j}\right)^2 + \left(\frac{\Delta F_{HIRS,j}}{F_{HIRS,j}}\right)^2} \tag{4.3}$$

where $\Delta F_{HIRS,j}$ is 3.5 and ΔI_j is 1. This combines to give a global averaged flux uncertainty of 5.8 Wm^{-2} which results in a possible lower bound bias of 6.77 Wm^{-2},

which is still more than double the ES model-satellite bias. The uncertainty associated with the 9 band GCM configuration of the ES code evaluated against the line-by-line code AER is estimated at 0.55 Wm^{-2} for the clear-sky (Goldblatt et al., 2009), but unfortunately no equivalent exists for the all-sky. A pattern of positive biases associated with deep convective cloud is just visible in Figure 4.10c, but does not dominate the zonal bias as it does with observational evaluations (Figure 4.10a and 2.8a), indicating that the bias between radiative transfer codes is a global and systematic all-sky issue, not just one related to deep convective cloud. The vast difference between the all and the clear-sky indicate it is, however, a cloud related problem.

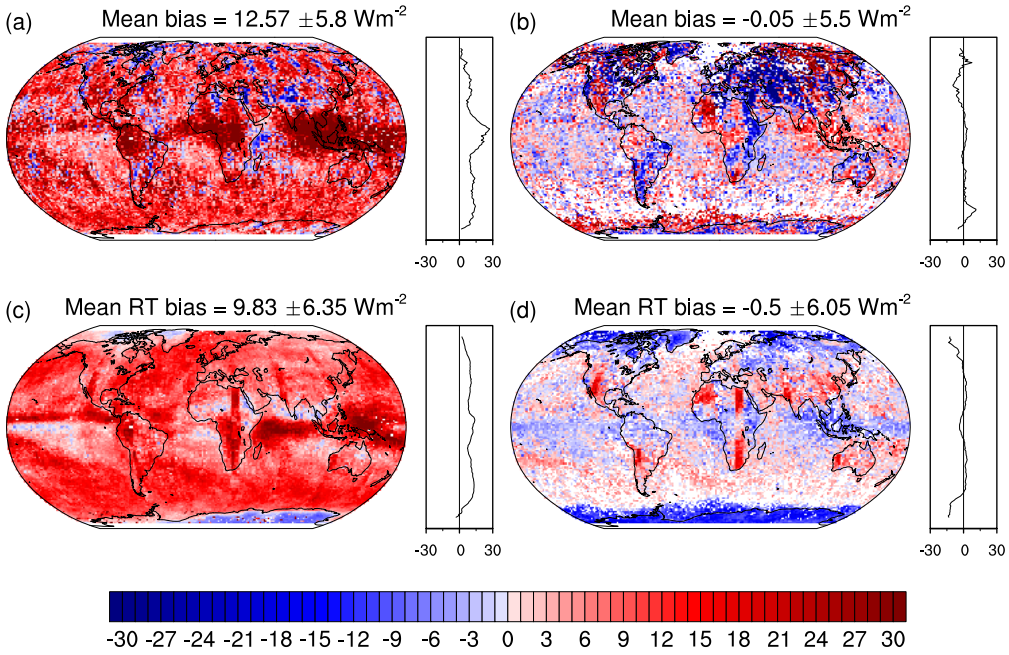

Figure 4.10: a) All-sky and b) clear-sky biases between model simulated IASI OLR and HIRS OLR fluxes. c) All-sky and) clear-sky biases between model simulated IASI OLR fluxes and those produced by the Edward-Slingo radiation code within HadGEM2. Units are Wm^{-2}. All maps are the mean of 2009, with zonal means shown to the right.

The lower flux biases produced by the ES code shown in Figure 2.8 have been reproduced previously by alternate studies (e.g. Wang and Su (2013)) so we can be

confident in these results. By comparing the spatial plots of IASI OLR flux bias (Figure 4.10a) with the ES flux bias (Figure 2.8a) it can be seen that in general the former produces too much outgoing radiation at all latitudes, and the negative biases that are present in the latter are not as prominent in the IASI OLR analysis. In light of this, and by a process of elimination of other possible errors, namely; the clear-sky analysis appears consistent, the IASI OLR observational product has been verified with independent observations in Chapter 4, Section 3.3.2, and the overestimated brightness temperatures produced by the HIRS and IASI evaluations are equal at corresponding wavenumbers, it seems likely that the all-sky inconsistency lies in the different treatments of the cloud-radiance interaction by both codes.

As detailed in Chapter 1 (Sections 1.3.6.1 and 1.4.4), both models parametrise cloud variables such as shape and effective hydrometeor diameter, where the latter does not represent a real physical quantity. For ice in particular, this parametrisation has the difficult task of providing a catch-all description of the wide varieties of ice crystal shapes (habits) and sizes that are present in nature. It is known that errors are introduced at this point particularly with semi-transparent clouds. These are often large because algorithms are unable to describe adequately the wide range of possible habits that could arise, which until recently had not even been described accurately by atmospheric science journals and textbooks (Bailey and Hallett, 2009). The range of radiation values associated with the different crystals in this distribution are large. For this reason such complex cloud systems are usually identified and discarded in assimilation systems to avoid inaccuracies (Lavanant et al., 2011). However, a comparison with observations that have not been equivalently filtered will clearly highlight this discrepancy.

As discussed in Chapter 2, Section 2.4 the radiation balance in HadGEM2 is controlled primarily by tuning cloud-related parameters to known broadband targets (Martin et al., 2011), and it is likely due to this tuning process that the code gives tolerable results with respect to observations. It is unlikely that the multiple scattering scheme in RTTOV has been tuned to such an extent, in part because a broadband instrument is not part of its simulation suite. In a sense this means that RTTOV provides a more independent test of the parametrisations that are part of its fast radiative transfer model. In a previous sensitivity study of RTTOV-10, Faijan et al.

(2012) identified the vertical distribution of clouds as having a large effect on brightness temperatures for a relatively small perturbation, consistent with the results of the sensitivity tests presented in Section 2.3.4.2, but also found that the choice of ice cloud effective diameter (D_e) exhibited far greater sensitivity than those shown in Section 2.3.4.3, with differences of up to 20 K between schemes (see Figure 5. of Faijan et al. (2012)) which prompts further analysis of this factor in the present study.

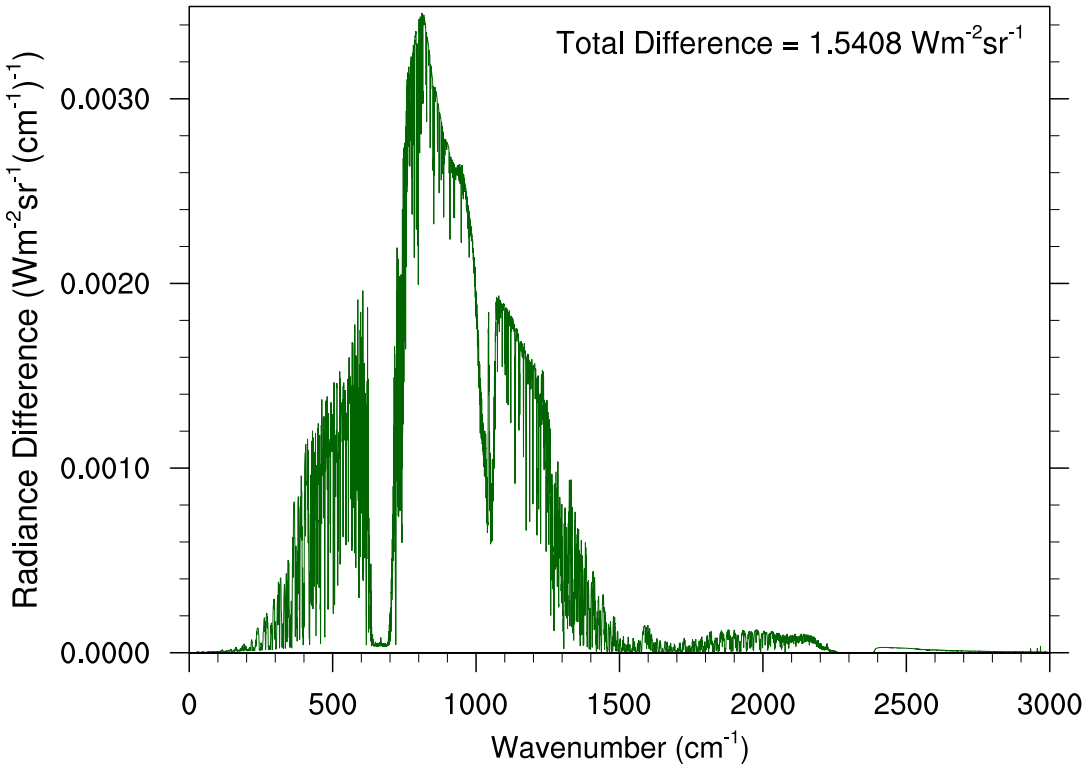

Figure 4.11: Differences between globally averaged simulated spectra that differ only in their choice of ice cloud parametrisation within RTTOV. The order is Wyser D_e and aggregate ice crystal shape (the default) minus Boudala D_e and hexagonal ice crystal shape. Units are $Wm^{-2}sr^{-1}(cm^{-1})^{-1}$. Data is the average of January and July 2009.

The Wyser parametrisation of D_e (Wyser and Yang, 1998) combined with an aggregate ice crystal shape was selected as the default combination to perform all

simulations throughout this project based on the outcome of existing studies (Vidot et al., 2011; Baran and Francis, 2004). This arrangement is shown to predict one of the largest brightness temperatures of all the 8 possible combinations in the 12 HIRS channels (Figure 2.12). In order to test the effect of a different ice parametrisation choice at all wavenumbers, the Boudala et al. (2002) parametrisation of D_e with hexagonal shaped ice crystals is selected to rerun IASI OLR simulations from January and July 2009. This combination produced the lowest brightness temperatures in Figure 2.12, by up to 2.5 K, so should give an indication of the full spectral range of sensitivity to ice cloud parametrisation. Figure 4.11 shows the difference between the 2 simulations which is highly spectrally dependent and reaches up to 0.0034 $Wm^{-2}sr^{-1}$ (2.5 K in the equivalent brightness temperature comparison) around the peak of the window region at 800 cm^{-1}. Errors of up to 0.0018 $Wm^{-2}sr^{-1}$ (1.5 K) are present in the FIR, isolating the effect of ice clouds in the upper troposphere. This range is still a factor of 10 less than those reported by Faijan et al. (2012) which likely arises because these are globally averaged profiles that include clear and non-ice cloud scenes, whereas the previous study is based on an instantaneous profile of identified ice cloud. Another feature visible in Figure 4.11 is the bug recently identified in the 800 - 1000 cm^{-1} region which is associated with the aggregate particle shape, and shows an erroneous curved shape[1]. In terms of the new flux bias that is given with this parametrisation combination the global mean bias is estimated at around 8 Wm^{-2} rather than 12.5 Wm^{-2}. This is still a difference of around 5 Wm^{-2} between the 2 radiation codes, hence if the treatment of ice-radiative effects is the primary source of this difference the range of parametrisations available in RTTOV-10 do not adequately encompass observational values.

4.4 Conclusions and Discussion

The construction of a spectrally resolved OLR observational product from 0-3000 cm^{-1} that can be equivalently simulated in the climate model world has allowed the combination of the HadGEM2-A GCM and the RTTOV-10 radiative transfer code to be evaluated at a heretofore unprecedented level, in both the all-sky and the clear-sky. Annual mean all-sky radiances appear greatly overestimated at all wavenumbers

[1]See the link to the forum post at the bottom of the webpage http://nwpsaf.eu/deliverables/rtm/rtm_rttov11.html

and compensating negative biases outside of the HIRS coverage previously hypothesised in Chapter 2 are absent, with the far infrared contributing to the overall bias rather than cancelling it. Equivalent clear-sky biases are much lower overall, in part due to spectral and spatial cancellation of errors. A flux-to-flux comparison was enabled by estimating the spatial distribution of anisotropic factors, using collocated HIRS OLR fluxes and IASI OLR radiances, which yielded global mean model fluxes in excess of 12 Wm^{-2} higher than observations in the all-sky. The difference between this and the fluxes calculated using the climate models broadband radiation code are around 10 Wm^{-2} which is outside the range of uncertainty in the method used to estimate flux. An equivalent analysis adjusting the ice cloud parametrisation to reflect the radiances that have the biggest differences to the original configuration selected showed a bias reduction of 4.5 Wm^{-2}, which is still not enough to completely explain its size, suggesting the existence of residual cloud problems.

Both the ES and the RTTOV-10 code operate on the same underlying cloud data but use different optical property parametrisations, with the ES simulation being significantly closer to observations. Even when an alternative ice cloud parametrisation is used in RTTOV that results in reduced biases they are still significantly higher across the spectrum, suggesting the parametrisation of clouds in RTTOV does not approach observations adequately enough to obtain meaningful results for cloud studies on a spectral level, i.e. identifying the signal of ice clouds in the far infrared. This is a conclusion that could only have been drawn due to the construction of a broadband product from hyperspectral data because it eliminates the possibility of compensating negative errors. However, this is not to say that RTTOV's way of representing ice clouds is wrong and ES's is right, particularly as it is possible that the latter's tuning process produces compensating spectral errors particularly because the target observations are broadband rather than line-by-line. The ES code is tuned by adjusting OLR to macroscopic cloud parameters such as fraction that are themselves tuned parameters in a sense, using statistical relationships to approximate the outcome of a particular set of gridbox conditions. If the first tunable relationship is wrong, tuning of the second could create the right results based on an incorrect relationship, which may cause unforseen problems in certain situations. It is important that the macro and microscopic properties are as accurate as possible in the first instance, before tuning commences.

These parametrisations are based on microphysical properties such as D_e that given their highly variable nature, do not necessarily reflect an actual situation, and current developments are reflecting the need for even more sophisticated schemes, with more physical choices of input variables (Edwards et al., 2007). For example RTTOV-10 provides the option for the user to specify their own effective diameter, and in the most recent version of the code (RTTOV-11.2), a new ice cloud database that has been introduced which only depends on cloud top temperature and ice water content (Baran et al., 2009, 2014), and eliminates the need to estimate D_e entirely. The database is based on an ensemble of different ice cloud habits, not just hexagonal or aggregates, which is expected to be more realistic than either of these shapes. It is planned to retire the ice parametrisations based on D_e in a future version of RTTOV, as they are based on particle size distributions which are likely to be biased towards smaller ice crystals (Korolev et al., 2011). This newer parametrisation gives consistent optical properties across all wavelengths but still displays a bias comparable with the other schemes in comparison with observations. For example the bias is still higher than observations at all wavenumbers than the Boudala et al. (2002) parametrisation of D_e combined with hexagonal ice crystals (Saunders et al., 2013), indicating there is still much work to be done in this area. This is also hindered by the limits of computational power, as even fast radiative transfer codes still struggle to simulate instruments with higher spectral resolution in terms of efficiency and time.

There are limited conclusions that can be drawn from the current project regarding the sources of climate model-satellite biases, because the OLR errors associated with the radiative transfer code are difficult to separate from those originating from the climate model. In order to improve the representation of clouds within radiative transfer codes, both satellite simulators and climate model based, accurate retrieved vertical profiles of the many varied microphysical properties of clouds, particularly ice clouds, combined with multispectral radiation measurements is the best way forward. This is an area of active research that is progressing at speed, particularly with the wealth of in-cloud properties that have been retrieved by virtue of the A-Train satellite constellation (Stubenrauch et al., 2013; Stephens et al., 2008). More detailed spectral observations could improve things further; a recent proposal for a

submillimetre sensor which would have a greater ability to retrieve ice water content further down in the vertical cloud column is one example (Buehler et al., 2007). This would allow a database of variables to be constructed that provides enough detail to derive better constrained relationships between current model diagnostics, or allows new ones to be created.

Chapter 5

Conclusion

This chapter bring together the key points and overall lessons learnt from the thesis, along with potential directions for future study. Radiances, and their corresponding brightness temperatures, from narrowband (HIRS), hyperspectral (IASI), and broadband (CERES and HIRS OLR) longwave satellite measurements have been compared with the equivalent quantities simulated using the appropriate forward model (RTTOV or ES) on HadGEM2-A climate variables. A major tool in this evaluation was the development of an extended hyperspectral product that is a fusion of real satellite measurements with those predicted via regression techniques, using physical correlations between different parts of the spectrum. Overall the study used an 'all-sky versus clear-sky' approach to isolate and assess the representation of clouds in the climate and radiative transfer model.

5.1 Summary

The forward model comparison was facilitated by satellite-like sampling of climate model data. Diurnal differences were minimised by restricting local times to the subset covered by the MetOp-A sun-synchronous orbit. Instantaneous climate model data obtained at 15 hourly intervals was selected instead of monthly averages to sample more of the diurnal cycle at a lower temporal resolution, in order to reduce data volumes. The clear-sky product was constructed with an upper limit of 40% cloud fraction, which proved robust for all channels apart from those with high sensitivity

to water vapour, due to its intrinsic correlation with clouds. To ensure consistency with gridded climate model grid data model-like sampling was applied to the IASI OLR product by gridding and averaging the satellite data before constructing the extended spectrum.

HIRS channels were used to investigate the sensitivity of radiances to cloud parameters through a variety of simple tests that perturbed macrophysical properties such as fraction, height and hydrometeor concentration, and made alternate choices when filtering clouds for input to the fast radiative transfer code, RTTOV. The main findings from this exploratory study were the discovery of large all-sky biases in the window region that were not observed in the corresponding clear-sky results. Broadband biases obtained using HIRS OLR and CERES satellite data, and HadGEM2's own radiation scheme (Edward-Slingo) as the forward model were significantly lower, which pointed towards compensating biases outside of the HIRS coverage. Radiances were identified as being particularly sensitive to cloud height, and the choice of parametrisation in RTTOV for the interaction between ice clouds and radiation also displayed a significant range.

The coverage of the HIRS instrument was shown to be highly useful for evaluating the main features of the longwave spectrum, with channels at wavenumbers that isolate the effects of carbon dioxide, clouds and water vapour. However, the lack of channels in the FIR region required alternative observational sources. The issue of compensating biases raised by the HIRS evaluation prompted the construction of the IASI OLR product, with the primary aim of evaluating the FIR and the secondary benefit of obtaining the entire outgoing longwave coverage at extremely high resolution for flexible exploration of the whole spectrum.

The IASI OLR is one of only a few similar products currently in existence that provide quasi-observational satellite measurements of the FIR; a theoretical construction required due to technological gap in this spectral region. It has unprecedented coverage extending to 25 cm^{-1} (400 μm) with a sampling resolution of 0.5 cm^{-1} in the FIR and NIR regions. Two separate verifications of the product were carried out by comparing the spectrally integrated product with broadband CERES radi-

ances, instantaneously at simultaneous nadir overpasses, and on an averaged basis by comparing composites of global data. Mean differences were about 1 $Wm^{-2}sr^{-1}$ (just over 1% relative difference) for all-sky measurements, which is within the 1.5% absolute calibration uncertainty for LW CERES radiances. Part of this difference will almost certainly arise from errors relating to both instruments sensing slightly different scenes at simultaneous nadir overpasses. Examination of the mean properties of the new product show that the FIR contributes between 43 - 64% to the total OLR intensity with instantaneous profiles, with global averages of 47% in the all-sky and 44% in the clear-sky. As the entirety of this percentage is estimated by theoretical correlations, the consistency with totally independent measurements is a strong argument for the products ability to accurately simulate the whole OLR spectrum.

The primary aim of producing the IASI OLR product was to allow the simulation of the same radiances from climate model output with RTTOV and identify compensating biases in the longwave spectrum. An additional goal was to assess the contribution of the far infrared portion of the spectrum because it is an unobserved but radiatively significant region. It also contains the spectral signature of ice clouds, whose inhomogeneity renders them challenging to parametrise in global climate models. The results of the IASI OLR evaluation were surprising in that all-sky compensating biases were negligible and outgoing radiation was over estimated across the spectrum, apart from at wavenumbers whose weighting functions peak in the stratosphere. As with the HIRS analysis clear-sky biases were again low across the spectrum, which is a tough test and therefore suggests HadGEM2 represents non-cloudy state variables well. The source of the all-sky bias is almost entirely dominated by clouds, which is evident from the spectral cloud radiative forcing biases being of near identical size and shape to the all-sky biases. However, by employing a method to estimate IASI OLR fluxes it was revealed that an average of 80% of this bias can be attributed to the radiative transfer code RTTOV, if it is assumed that the climate model configuration of the Edwards-Slingo infrared radiative transfer code is accurate. This assumption is discussed further in the limitations section.

The results of the HIRS analysis suggest that although the choice of RTTOV's ice

cloud parametrization could contribute brightness temperatures of up to 2.5 K (42%) of the bias in window channels based on results obtained when the combination with the lowest bias is selected, the vertical distribution of clouds exhibit a greater sensitivity. Over the whole spectrum simulated with IASI the alternate parametrisation make a 50% difference (4.93 Wm^{-2} instead of 9.83 Wm^{-2}) to the flux bias between the RTTOV and ES codes. The clear-sky difference remains the same, hence there is still 4.9 Wm^{-2} of difference between the codes which is due to the cloud representation. These results suggest that the range of radiances simulated by RTTOV-10 using the ice parametrisations available do not encompass the true values, and there are further problems with either its ice or liquid cloud parameterisations that need to be addressed.

5.2 Challenges and Limitations

A current challenge involved when creating a relationship between ice particle concentration and effective diameter, which is then used to calculate the emitted radiation, is that crystal shape is currently not accounted for at anywhere near the level of detail required, given the large sensitivity of radiance to ice habit. The interaction between spherical liquid cloud droplets and radiation is much more easily described, hence, it is speculated that although all cloud-radiance interactions are challenging to parametrise, it is likely that the root of the substantial cloud error identified lies in RTTOV's ice cloud parametrization. This discovery places a fundamental limitation on the use of all-sky simulated spectral radiances to assess the accuracy of climate model variables in the context of the current study, as the individual contributions of GCM cloud errors and RTTOV cloud errors are not well defined. The different units that climate models and radiative transfer models use respectively (flux versus radiance) presents additional challenges for their inter-comparison.

In addition to this major limitation deduced from the combined results of the study, several others were illuminated over the course of the project. It was shown in Chapter 2 that the construction of a clear-sky climate model product was challenging when considering channels sensitive to water vapour, as they exhibit sensitivity to the small fractions of cloud that fall under the specified threshold. This threshold

is a fundamentally arbitrary choice that fortunately proves robust in most channels, but the correlation between clouds and water vapour is unavoidable in those channels with the appropriate sensitivity. This places a limitation on the use of clear-sky climate model data for studies of water vapour and it is suggested this variable be used with caution.

Additionally, prominent compensating spatial biases were observed upon examination of stratospheric peaking channels in the CO_2 region which relate to the limited vertical resolution of the climate model, a common problem amongst GCMs. The project used the standard configuration, otherwise known as the 'low-top' model with 38 levels as opposed to the 60 level 'high-top' version. There is a limit to how accurately the stratospheric dynamics can be represented with the coarseness of the vertical resolution, hence limited information can be gleaned from examination of climate model radiation bands that peak in the stratosphere with similar configurations. Diagnosing this issue, however, is an important step in subsequently improving it.

The accuracy of the IASI OLR product presented in Chapter 3 was revealed to be within reasonable bounds of uncertainty, even with the added challenge presented by IASI and CERES being on different satellite platforms. The lack of a broadband product flying alongside IASI makes estimating fluxes more challenging. Previous studies have utilised CERES for obtaining information about scene anisotropy, by virtue of its existing algorithm, that has been applied to other instruments onboard at coincident footprints (Huang et al., 2008). The method used to estimate spatial anisotropy in Chapter 4 was very empirical and the large uncertainty in the resulting fluxes is dominated by the errors introduced when using this approach. Alternatively, a different method for estimating fluxes from IASI radiances is an option that could be the topic of future work. A further technological issue involved when using the IASI OLR product is its size, being comprised of 10181 channels. This places restrictions on processing and use of this dataset at current computational limits, which is a consideration that should not be underestimated.

The greater bias obtained when using RTTOV rather than the Edward-Slingo code

to model all-sky broadband fluxes (which is not seen in the clear-sky) suggests that RTTOV's cloud parametrisation is significantly more inaccurate than the latter. However, this assumes that the ES code is accurate, which may not necessarily be true. Although a clear-sky evaluation of the GCM configuration against a LBL code has been performed (Goldblatt et al., 2009), no equivalent exists for the all-sky, which is needed to verify this hypothesis. Even with such an analysis, however, it should not be assumed that LBL codes are error-free themselves, as they contain their own parametrisations of cloud-radiative effects which are unlikely to be without uncertainties.

The ES code has the advantage of being previously tuned to known broadband values, but this process can produce inaccurate underlying variables, even with tolerable radiance results. To illustrate this concept, Figure 5.1 shows a simplified version of one of the many chains of parametrisations that link one variable to another. Each arrow represents one or more dependencies that are approximated by statistical relationships that greatly simplify the actual process. It is these many layers of parametrisations that can have a cumulative knock-on effect, potentially allowing errors to propagate through the chain. Herein lies a fundamental limitation of the insights that radiation studies can give into cloud parametrisations alone. It is the quantity extracted at the very end of the chain and can only provide a 'top-down' evaluation. A 'bottom-up' approach is needed to effectively improve parametrisations, by constraining the variables lower down the process to avoid tuning parameters to unreasonable values in order to produce the right top level quantity.

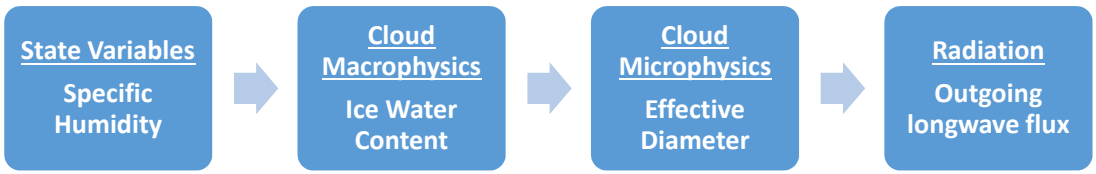

Figure 5.1: A chain of climate model variables whose values depend on the one preceding it. The arrows represent one or more parametrisations which are used to approximate the relationship between one variable and the next.

5.3 Future Work

A greater distinction could be attributed to biases in either of the radiation codes through further work, though in light of the deficiencies revealed in the RTTOV version 10 ice cloud parametrisations it is recommended that these configurations be avoided as the basis of future work. The most recent version of RTTOV (version 11.2) with its new parametrisation for ice-radiation effects could be tested and back-compared with the configurations available in version 10.2, by developing a methodology to separate the biases in ice and liquid clouds. It could also be possible to extract the effective diameter estimated by the Edwards-Slingo code for direct input into RTTOV to assess whether this improves results. However a detailed knowledge of the different ways both codes deal with this quantity would be required to ensure consistency, which is beyond the scope of the current project.

To remove the possibility of potential biases associated with the ES code from the RTTOV evaluation it could be useful to follow an approach similar to that adopted by Faijan et al. (2012), and attempt to use observed values of cloud and other variables as inputs together with their associated measured radiances. This could potentially be achieved with reanalysis data, although cloud quantities are still estimated therein using a model, or alternatively retrieved quantities from the cloud instruments onboard the A-Train constellation of satellites could provide more observationally constrained data. A potentially more difficult approach is to apply the climate configuration of the Edwards-Slingo broadband code to observations in a similar manner, however in the first instance a test involving a comparison with LBL output would indicate the level of overall performance in its different spectral regions and illuminate any compensating biases.

The spectral flexibility afforded by the new IASI OLR product offers the ability to create user defined wavebands across the spectrum by integrating across the appropriate part of the finely resolved spectrum. Based on the results of Chapter 4 it could be advantageous to use an alternative forward model to the RTTOV satellite simulator to test climate model output, such as the ES code itself. The 9 bands that make up the broadband simulated fluxes can be extracted separately and equivalently constructed from IASI, so long as an accurate enough method for estimating

band-by-band fluxes was developed for IASI OLR observations. The selected placement of future instruments on coincident IASI satellite platforms will influence this process. This would still allow the broad features of the FIR to be evaluated as it is covered by 3 consecutive bands in the ES code.

Finally the model-to-radiance approaches explored in this thesis could serve as a prototype study for assessing other climate models that participate in the CMIP project in a similar manner, so long as the corresponding required variables could be obtained, or constructed. This might involve further synergising of output so cloud macro and microphysical properties were consistent across all models, and would require examination of how different models partition different cloud types. Additionally, if the radiative transfer codes that relate to these different climate models were made flexible enough to be applied to a common set of state variables, this could highlight common biases amongst codes which would be instructive, as particularly in the all-sky this is something that is lacking.

Bibliography

Abel, P. and Gruber, A. (1979). An improved model for the calculation of longwave flux at 11 μm. *NOAA Tech. Rep. NESS*, (106):24.

Ackerman, S. A. and Stephens, G. L. (1987). The absorption of solar radiation by cloud droplets: An application of anomalous diffraction theory. *Journal of the Atmospheric Sciences*, 44(12):1574–1588.

Allan, R., Ringer, M., and Slingo, A. (2003). Evaluation of moisture in the Hadley Centre climate model using simulations of HIRS water-vapour channel radiances. *Quarterly Journal of the Royal Meteorological Society*, 129(595):3371–3389.

Allan, R. and Slingo, A. (2002). Can current climate model forcings explain the spatial and temporal signatures of decadal OLR variations? *Geophysical Research Letters*, 29(7):1141.

Allan, R. P. (2009). Examination of relationships between clear-sky longwave radiation and aspects of the atmospheric hydrological cycle in climate models, reanalyses, and observations. *Journal of Climate*, 22(11):3127–3145.

Allison, L. J. and Warnecke, G. (1965). *The interpretation of TIROS radiation data for practical use in synoptic weather analysis*, volume 2851. National Aeronautics and Space Administration.

Alvarado, M., Payne, V., Mlawer, E., Uymin, G., Shephard, M., Cady-Pereira, K., Delamere, J., and Moncet, J. (2013). Performance of the Line-by-Line Radiative Transfer Model (LBLRTM) for temperature, water vapor, and trace gas retrievals: recent updates evaluated with IASI case studies. *Atmos. Chem. Phys*, 13:6687–6711.

Amorati, R. and Rizzi, R. (2002). Radiances simulated in the presence of clouds by use of a fast radiative transfer model and a multiple-scattering scheme. *Applied Optics*, 41(9):1604–1614.

Anderson, J., Dykema, J., Goody, R., Hu, H., and Kirk-Davidoff, D. (2004). Absolute, spectrally-resolved, thermal radiance: a benchmark for climate monitor-

ing from space. *Journal of Quantitative Spectroscopy and Radiative Transfer*, 85(3):367–383.

Bailey, M. P. and Hallett, J. (2009). A comprehensive habit diagram for atmospheric ice crystals: Confirmation from the laboratory, AIRS II, and other field studies. *Journal of the Atmospheric Sciences*, 66(9):2888–2899.

Baran, A. and Francis, P. (2004). On the radiative properties of cirrus cloud at solar and thermal wavelengths: A test of model consistency using high-resolution airborne radiance measurements. *Quarterly Journal of the Royal Meteorological Society*, 130(598):763–778.

Baran, A. J., Connolly, P., and Lee, C. (2009). Testing an ensemble model of cirrus ice crystals using midlatitude *in situ* estimates of ice water content, volume extinction coefficient and the total solar optical depth. *Journal of Quantitative Spectroscopy and Radiative Transfer*, 110(14):1579–1598.

Baran, A. J., Cotton, R., Furtado, K., Havemann, S., Labonnote, L.-C., Marenco, F., Smith, A., and Thelen, J.-C. (2014). A self-consistent scattering model for cirrus. II: The high and low frequencies. *Quarterly Journal of the Royal Meteorological Society*, 140(680):1039–1057.

Barker, H. W., Li, Z., and Blanchet, J.-P. (1994). Radiative characteristics of the Canadian Climate Centre second-generation general circulation model. *Journal of Climate*, 7(7):1070–1091.

Barkstrom, B. R. (1984). The earth radiation budget experiment (ERBE). *Bulletin of the American Meteorological Society*, 65(11):1170–1185.

Bates, J., Wu, X., and Jackson, D. (1996). Interannual variability of upper-troposphere water vapor band brightness temperature. *Journal of Climate*, 9(2):427–438.

Bianchini, G., Carli, B., Cortesi, U., Del Bianco, S., Gai, M., and Palchetti, L. (2008). Test of far-infrared atmospheric spectroscopy using wide-band balloon-borne measurements of the upwelling radiance. *Journal of Quantitative Spectroscopy and Radiative Transfer*, 109(6):1030–1042.

Bjerknes, V. (1904). *Das Problem der Wettervorhersage: betrachtet vom Standpunkte der Mechanik und der Physik*.

Blumstein, D., Chalon, G., Carlier, T., Buil, C., Hebert, P., Maciaszek, T., Ponce, G., Phulpin, T., Tournier, B., Simeoni, D., et al. (2004). IASI instrument: Technical overview and measured performances. In *Optical Science and Technology, the SPIE 49th Annual Meeting*, pages 196–207. International Society for Optics and Photonics.

Board, S. S. et al. (2007). *Earth science and applications from space: National imperatives for the next decade and beyond*. National Academies Press.

Bodas-Salcedo, A., Webb, M., Bony, S., Chepfer, H., Dufresne, J., Klein, S., Zhang, Y., Marchand, R., Haynes, J., Pincus, R., et al. (2011). COSP: Satellite simulation software for model assessment. *Bulletin of the American Meteorological Society*, 92:1023–1043.

Bony, S. and Emanuel, K. (2001). A parameterization of the cloudiness associated with cumulus convection; evaluation using TOGA COARE data. *Journal of the Atmospheric Sciences*, 58(21):3158–3183.

Boudala, F. S., Isaac, G. A., Fu, Q., and Cober, S. G. (2002). Parameterization of effective ice particle size for high-latitude clouds. *International Journal of Climatology*, 22(10):1267–1284.

Bower, K. N., Moss, S., Johnson, D., Choularton, T., Latham, J., Brown, P., Blyth, A., and Cardwell, J. (1996). A parametrization of the ice water content observed in frontal and convective clouds. *Quarterly Journal of the Royal Meteorological Society*, 122(536):1815–1844.

Brohan, P., Kennedy, J. J., Harris, I., Tett, S. F., and Jones, P. D. (2006). Uncertainty estimates in regional and global observed temperature changes: A new data set from 1850. *Journal of Geophysical Research: Atmospheres (1984–2012)*, 111(D12).

Budyko, M. I. (1969). The effect of solar radiation variations on the climate of the earth. *Tellus*, 21(5):611–619.

Buehler, S., Jimenez, C., Evans, K., Eriksson, P., Rydberg, B., Heymsfield, A., Stubenrauch, C., Lohmann, U., Emde, C., John, V., et al. (2007). A concept for a satellite mission to measure cloud ice water path, ice particle size, and cloud altitude. *Quarterly Journal of the Royal Meteorological Society*, 133(S2):109–128.

Cao, C., Ciren, P., Goldberg, M., and Weng, F. (2005a). Intersatellite calibration of HIRS from 1980 to 2003 using the simultaneous nadir overpass (SNO) method for improved consistency and quality of climate data. In *Int. TOVS Study Conf.*

Cao, C., Goldberg, M., and Wang, L. (2009). Spectral bias estimation of historical HIRS using IASI observations for improved fundamental climate data records. *Journal of Atmospheric and Oceanic Technology*, 26(7):1378–1387.

Cao, C., Weinreb, M., and Xu, H. (2004). Predicting simultaneous nadir overpasses among polar-orbiting meteorological satellites for the intersatellite calibration of radiometers. *Journal of Atmospheric and Oceanic Technology*, 21(4):537–542.

Cao, C., Xu, H., Sullivan, J., McMillin, L., Ciren, P., and Hou, Y. (2005b). Intersatellite radiance biases for the High-Resolution Infrared Radiation sounders (HIRS) on board NOAA-15,-16, and-17 from simultaneous nadir observations. *Journal of Atmospheric and Oceanic Technology*, 22(4):381–395.

Capelle, V., Chédin, A., Péquignot, E., Schlüssel, P., Newman, S. M., and Scott, N. A. (2012). Infrared continental surface emissivity spectra and skin temperature retrieved from iasi observations over the tropics. *Journal of Applied Meteorology and Climatology*, 51(6):1164–1179.

Cess, R. D. (1976). Climate change: An appraisal of atmospheric feedback mechanisms employing zonal climatology. *Journal of Atmospheric Sciences*, 33:1831–1843.

Cess, R. D. and Potter, G. L. (1987). Exploratory studies of cloud radiative forcing with a general circulation model. *Tellus A*, 39(5):460–473.

Chahine, M. T., Pagano, T. S., Aumann, H. H., Atlas, R., Barnet, C., Blaisdell, J., Chen, L., Divakarla, M., Fetzer, E. J., Goldberg, M., et al. (2006). AIRS: Improving weather forecasting and providing new data on greenhouse gases. *Bulletin of the American Meteorological Society*, 87(7).

Chang, T. and Cao, C. (2014). Modeling infrared radiometer self-emission with application to MetOp/HIRS. *IEEE*.

Charlton-Perez, A., Baldwin, M., Birner, T., Black, R., Butler, A., Calvo, N., Davis, N., Gerber, E., Gillett, N., Hardiman, S., et al. (2013). On the lack of stratospheric dynamical variability in low-top versions of the CMIP5 models. *Journal of Geophysical Research: Atmospheres*, 118:2494–2505.

Charney, J. G., Fjörtoft, R., and Neumann, J. v. (1950). Numerical integration of the barotropic vorticity equation. *Tellus*, 2(4):237–254.

Chen, R. and Cao, C. (2012). Physical analysis and recalibration of MetOp HIRS using IASI for cloud studies. *Journal of Geophysical Research*, 117(D3):D03103.

Chen, X., Huang, X., Loeb, N. G., and Wei, H. (2013). Comparisons of Clear-Sky Outgoing Far-IR Flux Infered from Satellite Observations and Computed from the Three Most Recent Reanalysis Products. *Journal of Climate*, 26(2):478–494.

Cheruy, F., Kandel, R., and Duvel, J. (1991). Outgoing longwave radiation and its diurnal variation from combined ERBE and Meteosat observations: 1. estimating OLR from meteosat data. *Journal of Geophysical Research: Atmospheres (1984–2012)*, 96(D12):22611–22622.

Chervin, R. M. (1988). On the relationship between computer technology and climate modelling. In *Physically-Based Modelling and Simulation of Climate and Climatic Change*, pages 1053–1068. Springer.

Chevallier, F., Bauer, P., Kelly, G., Jakob, C., and McNally, T. (2001). Model clouds over oceans as seen from space: Comparison with HIRS/2 and MSU radiances. *Journal of Climate*, 14(21):4216–4229.

Chevallier, F. and Kelly, G. (2002). Model clouds as seen from space: Comparison with geostationary imagery in the 11-μm window channel. *Monthly Weather Review*, 130(3):712–722.

Chou, M.-D., Lee, K.-T., Tsay, S.-C., and Fu, Q. (1999). Parameterization for cloud longwave scattering for use in atmospheric models. *Journal of Climate*, 12(1):159–169.

Chung, E., Soden, B., and Clement, A. (2012). Diagnosing climate feedbacks in coupled ocean–atmosphere models. *Surveys in Geophysics*, 33:733–744.

Chung, E., Soden, B., Sohn, B., and Schmetz, J. (2011). Model-simulated humidity bias in the upper troposphere and its relation to the large-scale circulation. *Journal of Geophysical Research*, 116(D10):D10110.

Clerbaux, C., Boynard, A., Clarisse, L., George, M., Hadji-Lazaro, J., Herbin, H., Hurtmans, D., Pommier, M., Razavi, A., Turquety, S., et al. (2009). Monitoring of atmospheric composition using the thermal infrared IASI/MetOp sounder. *Atmospheric Chemistry and Physics*, 9(16):6041–6054.

Clerbaux, N., Dewitte, S., Gonzalez, L., Bertrand, C., Nicula, B., and Ipe, A. (2003). Outgoing longwave flux estimation: Improvement of angular modelling using spectral information. *Remote Sensing of Environment*, 85(3):389–395.

Clough, S., Shephard, M., Mlawer, E., Delamere, J., Iacono, M., Cady-Pereira, K., Boukabara, S., and Brown, P. (2005). Atmospheric radiative transfer modeling: A summary of the AER codes. *Journal of Quantitative Spectroscopy and Radiative Transfer*, 91(2):233–244.

Clough, S. A., Iacono, M. J., and Moncet, J.-L. (1992). Line-by-line calculations of atmospheric fluxes and cooling rates: Application to water vapor. *Journal of Geophysical Research: Atmospheres (1984–2012)*, 97(D14):15761–15785.

Collins, M., Booth, B. B., Bhaskaran, B., Harris, G. R., Murphy, J. M., Sexton, D. M., and Webb, M. J. (2011). Climate model errors, feedbacks and forcings: a comparison of perturbed physics and multi-model ensembles. *Climate Dynamics*, 36(9-10):1737–1766.

Collins, W., Bellouin, N., Doutriaux-Boucher, M., Gedney, N., Hinton, T., Jones, C., Liddicoat, S., Martin, G., O Connor, F., Rae, J., et al. (2008). Evaluation of the HadGEM2 model. *Hadley Centre Technical Note 74. Met Office: Exeter, UK*, 74.

Combs, A. C., Weickmann, H. K., Mader, C., and Tebo, A. (1965). Application of infrared radiometers to meteorology. *Journal of Applied Meteorology*, 4(2):253–262.

Cordero, E., Forster, P., et al. (2006). Stratospheric variability and trends in models used for the IPCC AR4. *Atmospheric Chemistry and Physics*, 6(12):5369–5380.

Costa, S. and Shine, K. (2006). An estimate of the global impact of multiple scattering by clouds on outgoing long-wave radiation. *Quarterly Journal of the Royal Meteorological Society*, 132(616):885–895.

Crevoisier, C., Clerbaux, C., Guidard, V., Phulpin, T., Armante, R., Barret, B., Camy-Peyret, C., Chaboureau, J.-P., Coheur, P.-F., Crépeau, L., et al. (2013). Towards IASI-New Generation (IASI-NG): impact of improved spectral resolution and radiometric noise on the retrieval of thermodynamic, chemistry and climate variables. *Atmospheric Measurement Techniques Discussions*, 6(6):11215–11277.

Cusack, S., Edwards, J., and Kershaw, R. (1999). Estimating the subgrid variance of saturation, and its parametrization for use in a GCM cloud scheme. *Quarterly Journal of the Royal Meteorological Society*, 125(560):3057–3076.

Davies, R., Randall, D. A., Corsetti, T. G., et al. (1987). A fast radiation parameterization for atmospheric circulation models. *Journal of Geophysical Research: Atmospheres (1984–2012)*, 92(D1):1009–1016.

Dee, D., Uppala, S., Simmons, A., Berrisford, P., Poli, P., Kobayashi, S., Andrae, U., Balmaseda, M., Balsamo, G., Bauer, P., et al. (2011). The ERA-Interim reanalysis: Configuration and performance of the data assimilation system. *Quarterly Journal of the Royal Meteorological Society*, 137(656):553–597.

Delamere, J., Clough, S., Payne, V., Mlawer, E., Turner, D., and Gamache, R. (2010). A far-infrared radiative closure study in the Arctic: Application to water vapor. *Journal of Geophysical Research: Atmospheres (1984–2012)*, 115(D17).

Derbyshire, S., Maidens, A., Milton, S., Stratton, R., and Willett, M. (2011). Adaptive detrainment in a convective parametrization. *Quarterly Journal of the Royal Meteorological Society*, 137(660):1856–1871.

Deschenes, O. and Moretti, E. (2009). Extreme weather events, mortality, and migration. *The Review of Economics and Statistics*, 91(4):659–681.

Dessler, A. and Yang, P. (2003). The distribution of tropical thin cirrus clouds inferred from Terra MODIS data. *Journal of Climate*, 16(8):1241–1247.

Dufresne, J.-L., Gautier, C., Ricchiazzi, P., and Fouquart, Y. (2002). Longwave scattering effects of mineral aerosols. *Journal of the atmospheric sciences*, 59(12):1959–1966.

Edwards, D. (1992). GENLN2: A general line-by-line atmospheric transmittance and radiance model. version 3.0: Description and users guide. *Unknown*, 1.

Edwards, J., Havemann, S., Thelen, J.-C., and Baran, A. (2007). A new parametrization for the radiative properties of ice crystals: Comparison with existing schemes and impact in a GCM. *Atmospheric Research*, 83(1):19–35.

Edwards, J. and Slingo, A. (1996). Studies with a flexible new radiation code. I: Choosing a configuration for a large-scale model. *Quarterly Journal of the Royal Meteorological Society*, 122(531):689–719.

Ellingson, R. G., Ellis, J., and Fels, S. (1991). The intercomparison of radiation codes used in climate models: Longwave results. *Journal of Geophysical Research: Atmospheres (1984–2012)*, 96(D5):8929–8953.

Ellingson, R. G., Lee, H.-T., Yanuk, D. J., and Gruber, A. (1989a). A technique for estimating outgoing longwave radiation from HIRS radiance observations. *Journal of Atmospheric and Oceanic Technology*, 6:706–711.

Ellingson, R. G., Yanuk, D. J., and Gruber, A. (1989b). Effects of the choice of meteorological data on a radiation model simulation of the NOAA technique for estimating outgoing longwave radiation from satellite radiance observations. *Journal of Climate*, 2(8):761–765.

Ellis, J. S. and Vander Haar, T. H. (1976). *Zonal average earth radiation budget measurements from satellites for climate studies*. Department of Atmospheric Science, Colorado State University Fort Collins, Colorado.

Esposito, F., Grieco, G., Leone, L., Restieri, R., Serio, C., Bianchini, G., Palchetti, L., Pellegrini, M., Cuomo, V., Masiello, G., et al. (2007). REFIR/BB initial observations in the water vapour rotational band: Results from a field campaign. *Journal of Quantitative Spectroscopy and Radiative Transfer*, 103(3):524–535.

Eyre, J. (1991). *A fast radiative transfer model for satellite sounding systems*. European Centre for Medium-Range Weather Forecasts Technical Memo 176.

Eyre, J. R. and Woolf, H. M. (1988). Transmittance of atmospheric gases in the microwave region: a fast model. *Applied Optics*, 27(15):3244–3249.

Faijan, F., Lavanant, L., and Rabier, F. (2012). Towards the use of cloud microphysical properties to simulate IASI spectra in an operational context. *Journal of Geophysical Research: Atmospheres (1984–2012)*, 117(D22).

Feldman, D. R., Collins, W. D., Pincus, R., Huang, X., and Chen, X. (2014). Far-infrared surface emissivity and climate. *Proceedings of the National Academy of Sciences*, 111(46):16297–16302.

Fels, S. B. and Kaplan, L. D. (1975). A test of the role of longwave radiative transfer in a general circulation model. *Journal of the Atmospheric Sciences*, 32(4):779–789.

Fu, Q. (1996). An accurate parameterization of the solar radiative properties of cirrus clouds for climate models. *Journal of Climate*, 9(9):2058–2082.

Fu, Q., Yang, P., and Sun, W. (1998). An accurate parameterization of the infrared radiative properties of cirrus clouds for climate models. *Journal of Climate*, 11(9):2223–2237.

Gleckler, P. J., Taylor, K. E., and Doutriaux, C. (2008). Performance metrics for climate models. *Journal of Geophysical Research: Atmospheres (1984–2012)*, 113(D6).

Golaz, J.-C., Golaz, J.-C., and Levy, H. (2013). Cloud tuning in a coupled climate model: Impact on 20th century warming. *Geophysical Research Letters*, 40(10):2246–2251.

Goldberg, M., Ohring, G., Butler, J., Cao, C., Datla, R., Doelling, D., Gärtner, V., Hewison, T., Iacovazzi, B., Kim, D., et al. (2011). The Global Space-Based Inter-Calibration System. *Bulletin of the American Meteorological Society*, 92(4).

Goldblatt, C., Lenton, T., and Watson, A. (2009). An evaluation of the long-wave radiative transfer code used in the met office unified model. *Quarterly Journal of the Royal Meteorological Society*, 135(640):619–633.

Goldstine, H. H. and Goldstine, A. (1946). The electronic numerical integrator and computer (ENIAC). *Mathematical Tables and Other Aids to Computation*, pages 97–110.

Goody, R., Anderson, J., and North, G. (1998). Testing climate models: An approach. *Bulletin of the American Meteorological Society*, 79(11):2541–2549.

Green, P. D., Newman, S. M., Beeby, R. J., Murray, J. E., Pickering, J. C., and Harries, J. E. (2012). Recent advances in measurement of the water vapour continuum in the far-infrared spectral region. *Philosophical Transactions of the Royal Society A: Mathematical, Physical and Engineering Sciences*, 370(1968):2637–2655.

Gregory, D. and Rowntree, P. (1990). A mass flux convection scheme with representation of cloud ensemble characteristics and stability-dependent closure. *Mon Weath Rev*, 118(7):1483–1506.

Gregory, D., Wilson, D., and Bushell, A. (2002). Insights into cloud parametrization provided by a prognostic approach. *Quarterly Journal of the Royal Meteorological Society*, 128(583):1485–1504.

Gregory, J. (1999). Representation of the radiative effects of convective anvils. *Hadley Centre Technical Note 7. Met Office: Exeter, UK*.

Gregory, J. and Webb, M. (2008). Tropospheric adjustment induces a cloud component in CO2 forcing. *Journal of Climate*, 21(1):58–71.

Gruber, A. (1977). Determination of the earth-atmosphere radiation budget from NOAA satellite data. *Unknown*, 1.

Gruber, A., Ellingson, R., Ardanuy, P., Weiss, M., Yang, S., and Oh, S. N. (1994). A comparison of ERBE and AVHRR longwave flux estimates. *Bulletin of the American Meteorological Society*, 75(11):2115–2130.

Gruber, A. and Winston, J. (1978). Earth-atmosphere radiative heating based on NOAA scanning radiometer measurements. *Bulletin of the American Meteorological Society*, 59:1570–1573.

Guan, B., Waliser, D. E., Li, J.-L. F., and Silva, A. (2013). Evaluating the impact of orbital sampling on satellite–climate model comparisons. *Journal of Geophysical Research: Atmospheres*, 118(2):355–369.

Gube, M. (1982). Radiation budget parameters at the top of the earth's atmosphere from METEOSAT data. *Journal of Applied Meteorology*, 21(12):1907–1921.

Hanel, R. A., C. B. J. J. D. E. . S. R. E. (2003). Exploration of the solar system by infrared remote sensing. *Cambridge Univ. Press*.

Hanel, R., Conrath, B., Kunde, V., Prabhakara, C., Revah, I., Salomonson, V., and Wolford, G. (1972). The Nimbus 4 infrared spectroscopy experiment: 1. Calibrated thermal emission spectra. *Journal of Geophysical Research*, 77(15):2629–2641.

Hardiman, S., Butchart, N., Hinton, T., Osprey, S., and Gray, L. (2012). The effect of a well resolved stratosphere on surface climate: Differences between CMIP5 simulations with high and low top versions of the Met Office climate model. *Journal of Climate*, 25(2012):7083–7099.

Harries, J., Carli, B., Rizzi, R., Serio, C., Mlynczak, M., Palchetti, L., Maestri, T., Brindley, H., and Masiello, G. (2008). The far-infrared earth. *Reviews of Geophysics*, 46(4):RG4004.

Harries, J. E., Brindley, H. E., Sagoo, P. J., and Bantges, R. J. (2001). Increases in greenhouse forcing inferred from the outgoing longwave radiation spectra of the Earth in 1970 and 1997. *Nature*, 410(6826):355–357.

Hartmann, D., Ramanathan, V., Berroir, A., and Hunt, G. (1986). Earth radiation budget data and climate research. *Reviews of Geophysics*, 24(2):439–468.

Haurwitz, F. and Kuhn, W. R. (1974). The distribution of tropospheric planetary radiation in the southern hemisphere. *Journal of Applied Meteorology*, 13(4):417–429.

Haywood, J. M., Allan, R. P., Culverwell, I., Slingo, T., Milton, S., Edwards, J., and Clerbaux, N. (2005). Can desert dust explain the outgoing longwave radiation anomaly over the sahara during july 2003? *Journal of Geophysical Research: Atmospheres (1984–2012)*, 110(D5).

Hess, M., Koepke, P., and Schult, I. (1998). Optical properties of aerosols and clouds: The software package OPAC. *Bulletin of the American Meteorological Society*, 79(5):831–844.

Hewison, T. J. and Muller, J. (2013). Ice contamination of Meteosat/SEVIRI implied by intercalibration against MetOp/IASI. *Geoscience and Remote Sensing, IEEE Transactions on*, 51(3):1182–1186.

Hewitt, H., Copsey, D., Culverwell, I., Harris, C., Hill, R., Keen, A., McLaren, A., and Hunke, E. (2011). Design and implementation of the infrastructure of HadGEM3: the next-generation Met Office climate modelling system. *Geosci. Model Dev*, 4:223–253.

Hill, P., Manners, J., and Petch, J. (2011). Reducing noise associated with the monte carlo independent column approximation for weather forecasting models. *Quarterly Journal of the Royal Meteorological Society*, 137(654):219–228.

Huang, X., Cole, J. N., He, F., Potter, G. L., Oreopoulos, L., Lee, D., Suarez, M., and Loeb, N. G. (2013). Longwave Band-By-Band Cloud Radiative Effect and Its Application in GCM Evaluation. *Journal of Climate*, 26(2):450–467.

Huang, X., Loeb, N., and Yang, W. (2010). Spectrally resolved fluxes derived from collocated AIRS and CERES measurements and their application in model evaluation: 2. cloudy sky and band-by-band cloud radiative forcing over the tropical oceans. *Journal of Geophysical Research*, 115(D21):D21101.

Huang, X., Ramaswamy, V., and Schwarzkopf, M. D. (2006). Quantification of the source of errors in AM2 simulated tropical clear-sky outgoing longwave radiation. *Journal of Geophysical Research: Atmospheres (1984–2012)*, 111(D14).

Huang, X., Yang, W., Loeb, N. G., and Ramaswamy, V. (2008). Spectrally resolved fluxes derived from collocated AIRS and CERES measurements and their application in model evaluation: Clear sky over the tropical oceans. *Journal of Geophysical Research: Atmospheres (1984–2012)*, 113(D9).

Huang, Y., Ramaswamy, V., Huang, X., Fu, Q., and Bardeen, C. (2007a). A strict test in climate modeling with spectrally resolved radiances: GCM simulation versus AIRS observations. *Geophysical Research Letters*, 34(24):L24707.

Huang, Y., Ramaswamy, V., and Soden, B. (2007b). An investigation of the sensitivity of the clear-sky outgoing longwave radiation to atmospheric temperature and water vapor. *Journal of geophysical research*, 112(D5):D05104.

Huber, M. and Knutti, R. (2014). Natural variability, radiative forcing and climate response in the recent hiatus reconciled. *Nature Geoscience*.

Hudson, S. R. and Brandt, R. E. (2005). A look at the surface-based temperature inversion on the Antarctic Plateau. *Journal of Climate*, 18(11):1673–1696.

Hulme, M., Barrow, E. M., Arnell, N. W., Harrison, P. A., Johns, T. C., and Downing, T. E. (1999). Relative impacts of human-induced climate change and natural climate variability. *Nature*, 397(6721):688–691.

Iacono, M., Delamere, J., Mlawer, E., and Clough, S. (2003). Evaluation of upper tropospheric water vapor in the NCAR community climate model (CCM3) using modeled and observed HIRS radiances. *Journal of geophysical research*, 108(D2):4037.

Inness, P. M. and Slingo, J. M. (2003). Simulation of the madden-julian oscillation in a coupled general circulation model. part i: Comparison with observations and an atmosphere-only gcm. *Journal of Climate*, 16(3):345–364.

Jackson, D., Wylie, D., and Bates, J. (2003). The HIRS Pathfinder radiance data set (1979-2001). In *Preprints, 12th Conf. on Satellite Meteorology and Oceanography, Long Beach, CA, Amer. Meteor. Soc. P*, volume 1.

Jacquinet-Husson, N., Scott, N., Chédin, A., Garceran, K., Armante, R., Chursin, A., Barbe, A., Birk, M., Brown, L., Camy-Peyret, C., et al. (2005). The 2003 edition of the GEISA/IASI spectroscopic database. *Journal of Quantitative Spectroscopy and Radiative Transfer*, 95(4):429–467.

Jiang, J., Su, H., Zhai, C., Perun, V., Del Genio, A., Nazarenko, L., Donner, L., Horowitz, L., Seman, C., Cole, J., et al. (2012). Evaluation of cloud and water vapor simulations in CMIP5 climate models using NASA A-Train satellite observations. *Journal of Geophysical Research*, 117(D14):D14105.

John, V., Holl, G., Allan, R., Buehler, S., Parker, D., and Soden, B. (2011). Clear-sky biases in satellite infrared estimates of upper tropospheric humidity and its trends. *Journal of Geophysical Research*, 116(D14):D14108.

John, V. and Soden, B. (2007). Temperature and humidity biases in global climate models and their impact on climate feedbacks. *Geophys. Res. Lett*, 34:L18704.

Joseph, J. H., Wiscombe, W., and Weinman, J. (1976). The delta-eddington approximation for radiative flux transfer. *Journal of the Atmospheric Sciences*, 33(12):2452–2459.

Kassianov, E., Barnard, J., Berg, L., Long, C., and Flynn, C. (2011). Shortwave spectral radiative forcing of cumulus clouds from surface observations. *Geophysical Research Letters*, 38(7):L07801.

Kato, S. and Loeb, N. G. (2005). Top-of-atmosphere shortwave broadband observed radiance and estimated irradiance over polar regions from clouds and the earth's radiant energy system (CERES) instruments on Terra. *Journal of Geophysical Research: Atmospheres (1984–2012)*, 110(D7).

Kay, J., Gettelman, A., Eaton, B., Boyle, J., J., Marchand, R., R., and Ackermann, T. (2012). Exposing global cloud biases in the community atmosphere model (CAM) using satellite observations and their corresponding instrument simulators. *J. Climate*, 25:5190–5207.

Kiehl, J., Hack, J., and Briegleb, B. (1994). The simulated earth radiation budget of the National Center for Atmospheric Research community climate model CCM2 and comparisons with the Earth Radiation Budget Experiment (ERBE). *Journal of Geophysical Research: Atmospheres (1984–2012)*, 99(D10):20815–20827.

Kiehl, J. and Ramanathan, V. (1990). Comparison of cloud forcing derived from the Earth Radiation Budget Experiment with that simulated by the NCAR Community Climate Model. *Journal of Geophysical Research: Atmospheres (1984–2012)*, 95(D8):11679–11698.

Klaes, D., Ackermann, J., Schraidt, R., Patterson, T., Schlüssel, P., Phillips, P., Arriaga, A., and Grandell, J. (2005). The ATOVS and AVHRR product processing facility of eps. *Advances in Space Research*, 36(5):996 – 1002. Atmospheric Remote Sensing: Earth's Surface, Troposphere, Stratosphere and Mesosphere.

Klein, S., Zhang, Y., Zelinka, M., Pincus, R., Boyle, J., and Gleckler, P. (2013). Are climate model simulations of clouds improving? an evaluation using the ISCCP simulator. *Journal of Geophysical Research: Atmospheres*.

Korolev, A., Emery, E., Strapp, J., Cober, S., Isaac, G., Wasey, M., and Marcotte, D. (2011). Small ice particles in tropospheric clouds: Fact or artifact? airborne icing

instrumentation evaluation experiment. *Bulletin of the American Meteorological Society*, 92(8):967–973.

Kratz, D. P. (2002). High-resolution modeling of the far infrared. In *International Symposium on Optical Science and Technology*, pages 171–180. International Society for Optics and Photonics.

Kristjánsson, J., Edwards, J., and Mitchell, D. (2000). Impact of a new scheme for optical properties of ice crystals on climates of two GCMs. *Journal of Geophysical Research: Atmospheres (1984–2012)*, 105(D8):10063–10079.

Larson, V. E., Wood, R., Field, P. R., Golaz, J.-C., Vonder Haar, T. H., and Cotton, W. R. (2001). Systematic biases in the microphysics and thermodynamics of numerical models that ignore subgrid-scale variability. *Journal of the Atmospheric Sciences*, 58(9):1117–1128.

Lauer, A. and Hamilton, K. (2013). Simulating clouds with global climate models: a comparison of CMIP5 results with CMIP3 and satellite data. *Journal of Climate*, 26(11):3823–3845.

Lavanant, L., Fourrié, N., Gambacorta, A., Grieco, G., Heilliette, S., Hilton, F., Kim, M.-J., McNally, A., Nishihata, H., Pavelin, E., et al. (2011). Comparison of cloud products within IASI footprints for the assimilation of cloudy radiances. *Quarterly Journal of the Royal Meteorological Society*, 137(661):1988–2003.

Lee, H., Gruber, A., Ellingson, R., and Laszlo, I. (2007). Development of the HIRS outgoing longwave radiation climate dataset. *Journal of Atmospheric and Oceanic Technology*, 24(12):2029–2047.

Lee, H.-T. and Ellingson, R. G. (2013). HIRS OLR climate data record–Production and validation updates. In *AIP Conference Proceedings*, volume 1531, page 420.

Lee, H.-T., Heidinger, A., Gruber, A., and Ellingson, R. G. (2004). The HIRS outgoing longwave radiation product from hybrid polar and geosynchronous satellite observations. *Advances in Space Research*, 33(7):1120–1124.

Leroy, S., Anderson, J., Dykema, J., and Goody, R. (2008). Testing climate models using thermal infrared spectra. *Journal of Climate*, 21(9):1863–1875.

Li, J., Wolf, W., Menzel, W., Zhang, W., Huang, H., and Achtor, T. (2000). Global soundings of the atmosphere from ATOVS measurements: The algorithm and validation. *Journal of Applied Meteorology*, 39(8):1248–1268.

Li, J.-L. F., Waliser, D. E., Stephens, G., Lee, S., L'Ecuyer, T., Kato, S., Loeb, N., and Ma, H.-Y. (2013). Characterizing and Understanding Radiation Budget Biases in CMIP3/CMIP5 GCMs, Contemporary GCM and Reanalysis. *Journal of Geophysical Research: Atmospheres*, 118:8166–8184.

Lindfors, A. V., Mackenzie, I. A., Tett, S. F., and Shi, L. (2011). Climatological diurnal cycles in clear-sky brightness temperatures from the high-resolution infrared radiation sounder (HIRS). *Journal of Atmospheric and Oceanic Technology*, 28(10):1199–1205.

Liou, K.-N. (1986). Influence of cirrus clouds on weather and climate processes: A global perspective. *Monthly Weather Review*, 114(6):1167–1199.

Loeb, N., Wielicki, B., Doelling, D., Smith, G., Keyes, D., Kato, S., Manalo-Smith, N., and Wong, T. (2009). Toward optimal closure of the Earth's top-of-atmosphere radiation budget. *Journal of Climate*, 22(3):748–766.

Loeb, N. G., Manalo-Smith, N., Kato, S., Miller, W. F., Gupta, S. K., Minnis, P., and Wielicki, B. A. (2003). Angular distribution models for top of atmosphere radiative flux estimation from the clouds and the earths radiant energy system instrument on the tropical rainfall measuring mission satellite. part I methodology. *Journal of applied meteorology*, 42(2).

Loeb, N. G., Parol, F., Buriez, J.-C., and Vanbauce, C. (2000). Top-of-atmosphere albedo estimation from angular distribution models using scene identification from satellite cloud property retrievals. *Journal of Climate*, 13(7):1269–1285.

Loeb, N. G., Priestley, K. J., Kratz, D. P., Geier, E. B., Green, R. N., Wielicki, B. A., Hinton, P. O., and Nolan, S. K. (2001). Determination of unfiltered radiances from the Clouds and the Earth's Radiant Energy System instrument. *Journal of Applied Meteorology*, 40(4):822–835.

MacKenzie, I., Tett, S., and Lindfors, A. (2012). Climate model-simulated diurnal cycles in HIRS clear-sky brightness temperatures. *Journal of Climate*, 25(2012):5845–5863.

Maestri, T. and Rizzi, R. (2003). A study of infrared diabatic forcing of ice clouds in the tropical atmosphere. *Journal of geophysical research*, 108(D4):4139.

Manabe, S. and Wetherald, R. T. (1967). Thermal equilibrium of the atmosphere with a given distribution of relative humidity. *Journal of the Atmospheric Sciences*, 24:241–259.

Mannozzi, L., Di Giuseppe, F., and Rizzi, R. (1999). Cirrus cloud optical properties in far infrared. *Physics and Chemistry of the Earth, Part B: Hydrology, Oceans and Atmosphere*, 24(3):269–273.

Martin, G., Bellouin, N., Collins, W., Culverwell, I., Halloran, P., Hardiman, S., Hinton, T., Jones, C., McDonald, R., McLaren, A., et al. (2011). The HadGEM2 family of Met Office Unified Model climate configurations. *Geoscientific Model Development*, 4(3):723–757.

Masiello, G., Serio, C., Esposito, F., and Palchetti, L. (2012). Validation of line and continuum spectroscopic parameters with measurements of atmospheric emitted spectral radiance from far to mid infrared wave number range. *Journal of Quantitative Spectroscopy and Radiative Transfer*, 113(11):1286–1299.

Matricardi, M. (2005). *The inclusion of aerosols and clouds in RTIASI, the ECMWF fast radiative transfer model for the infrared atmospheric sounding interferometer*. European Centre for Medium-Range Weather Forecasts.

Matricardi, M. (2007). An inter-comparison of line-by-line radiative transfer models. *ECMWF Research Dept. Tech. Memo. 525*.

Mauritsen, T., Stevens, B., Roeckner, E., Crueger, T., Esch, M., Giorgetta, M., Haak, H., Jungclaus, J., Klocke, D., Matei, D., et al. (2012). Tuning the climate of a global model. *Journal of Advances in Modeling Earth Systems*, 4(null):M00A01.

McFarquhar, G. M., Iacobellis, S., and Somerville, R. C. (2003). SCM simulations of tropical ice clouds using observationally based parameterizations of microphysics. *Journal of Climate*, 16(11):1643–1664.

McMillin, L. M., Fleming, H. E., and Hill, M. L. (1979). Atmospheric transmittance of an absorbing gas. 3: A computationally fast and accurate transmittance model for absorbing gases with variable mixing ratios. *Applied Optics*, 18(10):1600–1606.

Meador, W. and Weaver, W. (1980). Two-stream approximations to radiative transfer in planetary atmospheres: A unified description of existing methods and a new improvement. *Journal of the Atmospheric Sciences*, 37(3):630–643.

Meehl, G., Covey, C., Delworth, T., Latif, M., McAvaney, B., Mitchell, J., Stouffer, R., and Taylor, K. (2007). The WCRP CMIP3 multi-model dataset: A new era in climate change research. *Bulletin of the American Meteorological Society*, 88:1383–1394.

Minnis, P., Young, D. F., and Harrison, E. F. (1991). Examination of the relationship between outgoing infrared window and total longwave fluxes using satellite data. *Journal of Climate*, 4(11):1114–1133.

Minnis, P., Young, D. F., Sun-Mack, S., Heck, P. W., Doelling, D. R., and Trepte, Q. Z. (2004). CERES cloud property retrievals from imagers on TRMM, Terra, and Aqua. In *Remote Sensing*, pages 37–48. International Society for Optics and Photonics.

Miskolczi, F. M. and Mlynczak, M. G. (2004). The greenhouse effect and the spectral decomposition of the clear-sky terrestrial radiation. *Quarterly Journal of the Hungarian Meteorological Service*, 108(4):209–251.

Mitchell, D., Lawson, R., and Baker, B. (2011). Understanding effective diameter and its application to terrestrial radiation in ice clouds. *Atmospheric Chemistry and Physics*, 11(7):3417–3429.

Mitchell, D. L. (2002). Effective diameter in radiation transfer: General definition, applications, and limitations. *Journal of the Atmospheric Sciences*, 59(15):2330–2346.

Mitchell, D. L., Liu, Y., and Macke, A. (1996). Modeling cirrus clouds. part II: Treatment of radiative properties. *Journal of the Atmospheric Sciences*, 53(20):2967–2988.

Mlawer, E. J., Payne, V. H., Moncet, J.-L., Delamere, J. S., Alvarado, M. J., and Tobin, D. C. (2012). Development and recent evaluation of the MT_CKD model of continuum absorption. *Philosophical Transactions of the Royal Society A: Mathematical, Physical and Engineering Sciences*, 370(1968):2520–2556.

Mlawer, E. J., Taubman, S. J., Brown, P. D., Iacono, M. J., and Clough, S. A. (1997). Radiative transfer for inhomogeneous atmospheres: RRTM, a validated correlated-k model for the longwave. *Journal of Geophysical Research: Atmospheres (1984–2012)*, 102(D14):16663–16682.

Mlynczak, M., Johnson, D., Bingham, G., Jucks, K., Traub, W., Gordley, L., and Harries, J. (2004). The far-infrared spectroscopy of the troposphere (FIRST) project. In *Proc. SPIE*, volume 5659, pages 81–87.

Mlynczak, M., Johnson, D., Latvakoski, H., Jucks, K., Watson, M., Kratz, D., Bingham, G., Traub, W., Wellard, S., Hyde, C., et al. (2006). First light from the Far-Infrared Spectroscopy of the Troposphere (FIRST) instrument. *Geophysical Research Letters*, 33(7):L07704.

Morcrette, C., O'Connor, E., and Petch, J. (2012). Evaluation of two cloud parametrization schemes using ARM and Cloud-Net observations. *Quarterly Journal of the Royal Meteorological Society*, 138:964–979.

Morcrette, J. (1989). Comparison of satellite-derived and model-generated diurnal cycles of cloudiness and brightness temperatures. *Advances in Space Research*, 9:175–179.

Morcrette, J. (1991). Evaluation of model-generated cloudiness: Satellite-observed and model-generated diurnal variability of brightness temperature. *Monthly Weather Review*, 119(5):1205–1224.

Morcrette, J.-J. and Fouquart, Y. (1985). On systematic errors in parametrized calculations of longwave radiation transfer. *Quarterly Journal of the Royal Meteorological Society*, 111(469):691–708.

Nam, C., Bony, S., Dufresne, J.-L., and Chepfer, H. (2012). The 'too few, too bright'tropical low-cloud problem in CMIP5 models. *Geophysical Research Letters*, 39(21).

NOAA (2006). KLM user's guide. Section 3.2.2 HIRS/4.

Ohring, G., Gruber, A., and Ellingson, R. (1984). Satellite determinations of the relationship between total longwave radiation flux and infrared window radiance. *Journal of Climate and Applied Meteorology*, 23(3):416–425.

Ou, S. and Liou, K. (1995). Ice microphysics and climatic temperature feedback. *Atmospheric Research*, 35(2-4):127–138.

Palchetti, L., Bianchini, G., Carli, B., Cortesi, U., and Bianco, S. D. (2008). Measurement of the water vapour vertical profile and of the Earth's outgoing far infrared flux. *Atmospheric Chemistry and Physics*, 8(11):2885–2894.

Patz, J. A., Campbell-Lendrum, D., Holloway, T., and Foley, J. A. (2005). Impact of regional climate change on human health. *Nature*, 438(7066):310–317.

Phillips, N., Susskind, J., and McMillin, L. (1988). Results of a joint NOAA/NASA sounder simulation study. *Journal of Atmospheric and Oceanic Technology*, 5(1):44–56.

Phillips, N. A. (1956). The general circulation of the atmosphere: A numerical experiment. *Quarterly Journal of the Royal Meteorological Society*, 82(352):123–164.

Pincus, R., Platnick, S., Ackerman, S. A., Hemler, R. S., and Patrick Hofmann, R. J. (2012). Reconciling simulated and observed views of clouds: MODIS, ISCCP, and the limits of instrument simulators. *Journal of Climate*, 25(13):4699–4720.

Potter, G. L. and Cess, R. D. (2004). Testing the impact of clouds on the radiation budgets of 19 atmospheric general circulation models. *Journal of Geophysical Research: Atmospheres (1984–2012)*, 109(D2).

Priestley, K., Wielicki, B., Green, R., Haeffelin, M., Lee, R., and Loeb, N. (2002). Early radiometric validation results of the CERES Flight Model 1 and 2 instruments onboard NASA'S Terra Spacecraft. *Advances in Space Research*, 30(11):2371–2376.

Probst, P., Rizzi, R., Tosi, E., Lucarini, V., and Maestri, T. (2012). Total cloud cover from satellite observations and climate models. *Atmospheric Research*, 107:161–170.

Räisänen, P. (1998). Effective longwave cloud fraction and maximum-random overlap of clouds: A problem and a solution. *Monthly weather review*, 126(12):3336–3340.

Ramanathan, V. (1987). The role of earth radiation budget studies in climate and general circulation research. *Journal of Geophysical Research*, 92(D4):4075–4095.

Randall, D., Khairoutdinov, M., Arakawa, A., and Grabowski, W. (2003). Breaking the cloud parameterization deadlock. *Bulletin of the American Meteorological Society*, 84(11):1547–1564.

Randall, D., Wood, R., Bony, S., Colman, R., Fichefet, T., Fyfe, J., Kattsov, V., Pitman, A., Shukla, J., Srinivasan, J., Stouffer, R., Sumi, A., and Taylor, K. (2007). Climate Models and their Evaluation. in: Climate Change 2007: The Physical Science Basis. contribution of Working Group I to the Fourth Assessment Report of the Intergovernmental Panel on Climate Change. [Solomon, S., D. Qin, M. Manning, Z. Chen, M. Marquis, K.B. Averyt, M.Tignor and H.L. Miller (eds.)]. *Cambridge University Press, Cambridge, United Kingdom and New York, NY, USA.*, chapter 8.

Raschke, E., Vonder Haar, T. H., Bandeen, W. R., and Pasternak, M. (1973). The annual radiation balance of the earth-atmosphere system during 1969-70 from Nimbus 3 measurements. *Journal of Atmospheric Sciences*, 30:341–364.

Rathke, C., Fischer, J., Neshyba, S., and Shupe, M. (2002). Improving IR cloud phase determination with 20 microns spectral observations. *Geophysical Research Letters*, 29(8):50–1.

Rayner, N., Parker, D., Horton, E., Folland, C., Alexander, L., Rowell, D., Kent, E., and Kaplan, A. (2003). Global analyses of sea surface temperature, sea ice, and night marine air temperature since the late nineteenth century. *J. Geophys. Res*, 108(D14):4407.

Richardson, L. F. (2007). *Weather prediction by numerical process*. Cambridge University Press.

Righetti, P., Meixner, H., Sancho, F., Damiano, A., and Lazaro, D. (2007). Flight dynamics performances of the MetOp-A satellite during the first months of operations. *Oral presentation from the International Symposium on Space Flight Dynamics*.

Ringer, M. and Allan, R. (2004). Evaluating climate model simulations of tropical cloud. *Tellus A*, 56(4):308–327.

Ritter, B. and Geleyn, J.-F. (1992). A comprehensive radiation scheme for numerical weather prediction models with potential applications in climate simulations. *Monthly Weather Review*, 120(2):303–325.

Rizzi, R. (1994). Raw HIRS/2 radiances and model simulations in the presence of clouds. *ECMWF Tech. Report*, No. 73:29.

Rizzi, R. and Mannozzi, L. (2000). Preliminary results on the planetary emission between 100 and 600 cm^{-1}. *REFIR Radiation Explorer in the Far Infrared Final Rep ENV4 CT6*, 344:77–88.

Rizzi, R., Serio, C., and Amorati, R. (2002). Sensitivity of broadband and spectral measurements of outgoing radiance to changes in water vapor content. In *International Symposium on Optical Science and Technology*, pages 181–190. International Society for Optics and Photonics.

Rossow, W. B. and Schiffer, R. A. (1991). ISCCP cloud data products. *Bulletin of the American Meteorological Society*, 72(1):2–20.

Rothman, L. S., Jacquemart, D., Barbe, A., Chris Benner, D., Birk, M., Brown, L., Carleer, M., Chackerian Jr, C., Chance, K., Coudert, L. e. a., et al. (2005). The *HITRAN* 2004 molecular spectroscopic database. *Journal of Quantitative Spectroscopy and Radiative Transfer*, 96(2):139–204.

Rotstayn, L. D. (2000). On the "tuning" of autoconversion parameterizations in climate models. *Journal of Geophysical Research: Atmospheres (1984–2012)*, 105(D12):15495–15507.

Sassen, K., Wang, Z., and Liu, D. (2008). Global distribution of cirrus clouds from CloudSat/Cloud-Aerosol lidar and infrared pathfinder satellite observations (CALIPSO) measurements. *Journal of Geophysical Research*, 113(D8):D00A12.

Saunders, R. et al. (2010). RTTOV-9 science and validation report. *NWP SAF Report: EUMETSAT*.

Saunders, R. et al. (2011). RTTOV-10 science and validation report. *NWP SAF Report: EUMETSAT*.

Saunders, R., Hocking, J., Rundle, D., Rayner, P., Matricardi, M., Geer, A., Lupu, C., Brunel, P., and Vidot, J. (2013). RTTOV-11 science and validation report. *NWP SAF Report*, 32.

Schmetz, J. and Liu, Q. (1988). Outgoing longwave radiation and its diurnal variation at regional scales derived from Meteosat. *Journal of Geophysical Research: Atmospheres (1984–2012)*, 93(D9):11192–11204.

Shephard, M., Clough, S., Payne, V., Smith, W., Kireev, S., and Cady-Pereira, K. (2009). Performance of the line-by-line radiative transfer model (LBLRTM) for temperature and species retrievals: IASI case studies from JAIVEx. *Atmospheric Chemistry and Physics*, 9(19):7397–7417.

Shi, L. and Bates, J. J. (2011). Three decades of intersatellite-calibrated high-resolution infrared radiation sounder upper tropospheric water vapor. *Journal of Geophysical Research (Atmospheres)*, 116:4108.

Shine, K. P., Ptashnik, I. V., and Rädel, G. (2012). The water vapour continuum: brief history and recent developments. *Surveys in Geophysics*, 33(3-4):535–555.

Simeoni, D., Astruc, P., Miras, D., Alis, C., Andreis, O., Scheidel, D., Degrelle, C., Nicol, P., Bailly, B., Guiard, P., et al. (2004). Design and development of IASI instrument. In *Optical Science and Technology, the SPIE 49th Annual Meeting*, pages 208–219. International Society for Optics and Photonics.

Simmons, A., Uppala, S., Dee, D., and Kobayashi, S. (2007). ERA-Interim: New ECMWF reanalysis products from 1989 onwards. *ECMWF newsletter*, 110(110):25–35.

Sinha, A. and Harries, J. E. (1995). Water vapour and greenhouse trapping: The role of far infrared absorption. *Geophysical Research Letters*, 22(16):2147–2150.

Slingo, A. and Schrecker, H. (1982). On the shortwave radiative properties of stratiform water clouds. *Quarterly Journal of the Royal Meteorological Society*, 108(456):407–426.

Slingo, A. and Webb, M. (1997). The spectral signature of global warming. *Quarterly Journal of the Royal Meteorological Society*, 123(538):293–307.

Slingo, J., Bates, K., Nikiforakis, N., Piggott, M., Roberts, M., Shaffrey, L., Stevens, I., Vidale, P. L., and Weller, H. (2009). Developing the next-generation climate system models: challenges and achievements. *Philosophical Transactions of the Royal Society A: Mathematical, Physical and Engineering Sciences*, 367(1890):815–831.

Slingo, J. M. (1982). A study of the Earth's radiation budget using a general circulation model. *Quarterly Journal of the Royal Meteorological Society*, 108(456):379–405.

Smith, G., Mlynczak, P., Rutan, D., and Wong, T. (2008). Comparison of the diurnal cycle of outgoing longwave radiation from a climate model with results from ERBE. *Journal of Applied Meteorology and Climatology*, 47(12):3188–3201.

Smith, R. (1990). A scheme for predicting layer clouds and their water content in a general circulation model. *Quarterly Journal of the Royal Meteorological Society*, 116(492):435–460.

Soden, B. and Held, I. (2006). An assessment of climate feedbacks in coupled ocean-atmosphere models. *Journal of Climate*, 19(14):3354–3360.

Soden, B., Jackson, D., Ramaswamy, V., Schwarzkopf, M., and Huang, X. (2005). The radiative signature of upper tropospheric moistening. *Science*, 310(5749):841–844.

Sohn, B., Nakajima, T., Satoh, M., and Jang, H. (2010). Impact of different definitions of clear-sky flux on the determination of longwave cloud radiative forcing: NICAM simulation results. *Atmospheric Chemistry & Physics*, 10:11641–11646.

Stephens, G. (2005). Cloud feedbacks in the climate system: A critical review. *Journal of Climate*, 18(2):237–273.

Stephens, G., Campbell, G., and Haar, T. (1981). Earth radiation budgets. *Journal of Geophysical Research: Oceans (1978–2012)*, 86(C10):9739–9760.

Stephens, G. and Kummerow, C. (2007). The remote sensing of clouds and precipitation from space: A review. *Journal of the Atmospheric Sciences*, 64(11):3742–3765.

Stephens, G. L. (1979). *Optical properties of eight water cloud types*. Number 36. CSIRO.

Stephens, G. L. (1984). The parameterization of radiation for numerical weather prediction and climate models. *Monthly Weather Review*, 112(4):826–867.

Stephens, G. L., Li, J., Wild, M., Clayson, C. A., Loeb, N., Kato, S., L'Ecuyer, T., Stackhouse Jr, P. W., Lebsock, M., and Andrews, T. (2012). An update on Earth's energy balance in light of the latest global observations. *Nature Geoscience*, 5:691–696.

Stephens, G. L., Vane, D. G., Boain, R. J., Mace, G. G., Sassen, K., Wang, Z., Illingworth, A. J., O'Connor, E. J., Rossow, W. B., Durden, S. L., et al. (2002). The CloudSat mission and the A-Train: A new dimension of space-based observations of clouds and precipitation. *Bulletin of the American Meteorological Society*, 83(12):1771–1790.

Stephens, G. L., Vane, D. G., Tanelli, S., Im, E., Durden, S., Rokey, M., Reinke, D., Partain, P., Mace, G. G., Austin, R., et al. (2008). Cloudsat mission: Performance and early science after the first year of operation. *Journal of Geophysical Research: Atmospheres (1984–2012)*, 113(D8).

Stocker, T. F., Qin, D., Plattner, G.-K., Tignor, M., Allen, S. K., Boschung, J., Nauels, A., Xia, Y., Bex, V., and Midgley, P. M. (2013). *Climate change 2013: The physical science basis*. Cambridge University Press, Cambridge, United Kingdom and New York, NY, USA.

Stratton, R. and Stirling, A. (2012). Improving the diurnal cycle of convection in GCMs. *Quarterly Journal of the Royal Meteorological Society*, 138:1121–1134.

Stubenrauch, C., Rossow, W., Kinne, S., Ackerman, S., Cesana, G., Chepfer, H., Di Girolamo, L., Getzewich, B., Guignard, A., Heidinger, A., et al. (2013). Assessment of global cloud datasets from satellites: Project and database initiated

by the GEWEX radiation panel. *Bulletin of the American Meteorological Society*, 94(7):1031–1049.

Sun, F., Goldberg, M. D., Liu, X., and Bates, J. J. (2010). Estimation of outgoing longwave radiation from atmospheric infrared sounder radiance measurements. *Journal of Geophysical Research: Atmospheres (1984–2012)*, 115(D9).

Sundqvist, H., Berge, E., and Kristjánsson, J. E. (1989). Condensation and cloud parameterization studies with a mesoscale numerical weather prediction model. *Monthly Weather Review*, 117(8):1641–1657.

Suzuki, K., Golaz, J.-C., and Stephens, G. L. (2013). Evaluating cloud tuning in a climate model with satellite observations. *Geophysical Research Letters*, 40(16):4464–4468.

Taylor, K., Stouffer, R., and Meehl, G. (2012). An overview of CMIP5 and the experiment design. *Bulletin of the American Meteorological Society*, 93(4):485.

Thomas, S. and Priestley, K. (2014). CERES FM1 - FM6 Instrument Update. *Spring 2014 CERES Science Team Meeting. April 22-24. Hampton, VA*.

Turner, D. D., Tobin, D., Clough, S. A., Brown, P. D., Ellingson, R. G., Mlawer, E. J., Knuteson, R. O., Revercomb, H. E., Shippert, T. R., Smith, W. L., et al. (2004). The QME AERI LBLRTM: A closure experiment for downwelling high spectral resolution infrared radiance. *Journal of the Atmospheric Sciences*, 61(22).

Turner, E. C. and Tett, S. F. (2013). Using longwave HIRS radiances to test climate models. *Climate Dynamics*, pages 1–25.

Vidot, J., Guyot, Jourdan, G., Sourdeval, O., Brunel, O., P. Labonnote, L., and Brogniez, G. (2011). Evaluation of RTTOV ice cloud parameterization by comparison with infrared measurements from IIR/CALIPSO during the CIRCLE-2 experiment. *Poster from 2011 EUMETSAT Meteorological Satellite Conference*, page P.59.

Waliser, D. E., Li, J.-L. F., Woods, C. P., Austin, R. T., Bacmeister, J., Chern, J., Del Genio, A., Jiang, J. H., Kuang, Z., Meng, H., et al. (2009). Cloud ice: A climate model challenge with signs and expectations of progress. *Journal of Geophysical Research*, 114(D8):D00A21.

Wang, C., Yang, P., Dessler, A., Baum, B. A., and Hu, Y. (2014). Estimation of the cirrus cloud scattering phase function from satellite observations. *Journal of Quantitative Spectroscopy and Radiative Transfer*, 138:36–49.

Wang, H. and Su, W. (2013). Evaluating and understanding top of the atmosphere cloud radiative effects in Intergovernmental Panel on Climate Change (IPCC)

Fifth Assessment Report (AR5) Coupled Model Intercomparison Project Phase 5 (cmip5) models using satellite observations. *Journal of Geophysical Research: Atmospheres*, 118:683–699.

Washington, W. M. and Parkinson, C. L. (2005). *An introduction to three-dimensional climate modeling*. University science books.

Webb, M., Senior, C., Bony, S., and Morcrette, J.-J. (2001). Combining ERBE and ISCCP data to assess clouds in the hadley centre, ECMWF and LMD atmospheric climate models. *Climate Dynamics*, 17(12):905–922.

Weitzman, M. L. (2009). On modeling and interpreting the economics of catastrophic climate change. *The Review of Economics and Statistics*, 91(1):1–19.

Wielicki, B., Barkstrom, B., Harrison, E., Lee III, R., Louis Smith, G., and Cooper, J. (1996). Clouds and the Earth's Radiant Energy System (CERES): An earth observing system experiment. *Bulletin of the American Meteorological Society*, 77(5):853–868.

Wilson, D. and Ballard, S. (1999). A microphysically based precipitation scheme for the UK meteorological office unified model. *Quarterly Journal of the Royal Meteorological Society*, 125(557):1607–1636.

Wilson, D., Bushell, A., Kerr-Munslow, A., Price, J., and Morcrette, C. (2008). PC2: A prognostic cloud fraction and condensation scheme. i: Scheme description. *Quarterly Journal of the Royal Meteorological Society*, 134(637):2093–2107.

Wylie, D. (2008). Diurnal cycles of clouds and how they affect polar-orbiting satellite data. *Journal of Climate*, 21(16):3989–3996.

Wylie, D., Jackson, D., Menzel, W., and Bates, J. (2005). Trends in global cloud cover in two decades of HIRS observations. *Journal of Climate*, 18(15):3021–3031.

Wylie, D., Menzel, W., Woolf, H., and Strabala, K. (1994). Four years of global cirrus cloud statistics using HIRS. *Journal of Climate*, 7(12):1972–1986.

Wyser, K. and Yang, P. (1998). Average ice crystal size and bulk short-wave single-scattering properties of cirrus clouds. *Atmospheric Research*, 49(4):315–335.

Yang, G. and Slingo, J. (2001). The diurnal cycle in the tropics. *Monthly Weather Review*, 129(4):784–801.

Yang, P., Mlynczak, M. G., Wei, H., Kratz, D. P., Baum, B. A., Hu, Y. X., Wiscombe, W. J., Heidinger, A., and Mishchenko, M. I. (2003). Spectral signature of ice clouds in the far-infrared region: Single-scattering calculations and radiative sensitivity study. *Journal of Geophysical Research: Atmospheres (1984–2012)*, 108(D18).

Yang, Z. and Arritt, R. W. (2002). Tests of a perturbed physics ensemble approach for regional climate modeling. *Journal of Climate*, 15(20):2881–2896.

Zdunkowski, W., Welch, R., and Korb, G. (1980). An investigation of the structure of typical two-stream-methods for the calculation of solar fluxes and heating rates in clouds. *Beitraege zur Physik der Atmosphaere*, 53(2):147–166.

Zhou, T. and Yu, R. (2006). Twentieth-century surface air temperature over china and the globe simulated by coupled climate models. *Journal of Climate*, 19(22):5843–5858.